








A systematic analysis of the X-ray emission in optically selected tidal disruption events: observational evidence for the unification of the optically and X-ray selected populations

MURYEL GUOLO ¹, SUVI GEZARI ^{2,1}, YUHAN YAO ^{3,4,5}, SJOERT VAN VELZEN ⁶, ERICA HAMMERSTEIN ^{7,8,9},
S. BRADLEY CENKO ^{8,10} AND YARONE M. TOKAYER ¹¹

¹*Bloomberg Center for Physics and Astronomy, Johns Hopkins University, 3400 N. Charles St., Baltimore, MD 21218, USA*

²*Space Telescope Science Institute, 3700 San Martin Drive, Baltimore, MD 21218, USA*

³*Cahill Center for Astrophysics, California Institute of Technology, MC 249-17, 1200 E California Boulevard, Pasadena, CA 91125, USA*

⁴*Miller Institute for Basic Research in Science, 468 Donner Lab, Berkeley, CA 94720, USA*

⁵*Department of Astronomy, University of California, Berkeley, CA 94720, USA*

⁶*Leiden Observatory, Leiden University, PO Box 9513, 2300 RA Leiden, The Netherlands*

⁷*Department of Astronomy, University of Maryland, College Park, MD 20742, USA*

⁸*Astrophysics Science Division, NASA Goddard Space Flight Center, Mail Code 661, Greenbelt, MD 20771, USA*

⁹*Center for Research and Exploration in Space Science and Technology, NASA/GSFC, Greenbelt, MD 20771, USA*

¹⁰*Joint Space-Science Institute, University of Maryland, College Park, MD 20742, USA*

¹¹*Department of Physics, Yale University, P.O. Box 208121, New Haven, CT 06520, USA*

ABSTRACT

We present a systematic analysis of the X-ray emission of a sample of 17 optically selected, X-ray-detected tidal disruption events (TDEs) discovered between 2014 and 2021, using *XMM-Newton* and *Swift*/XRT observations. The X-ray light curves show a diverse range of temporal behaviors, with most sources not following the expected power-law decline. The X-ray spectra are mostly extremely soft and consistent with thermal emission from the innermost region of an accretion disk, which cools as the accretion rate decreases. Three sources show the formation of a hard X-ray corona, which occurs at least 200 days after the UV/optical peak. The shape of the spectral energy distribution, as traced by the ratio ($L_{\text{BB}}/L_{\text{X}}$) between the UV/optical and X-ray luminosities, shows a wide range of values $L_{\text{BB}}/L_{\text{X}} \in (0.5, 3000)$ at early-times, and converges to disk-like values $L_{\text{BB}}/L_{\text{X}} \in (0.5, 10)$ at late-times. The evolution of the derived physical parameters favors a decrease in the optical depth of a reprocessing layer instead of delayed disk formation to explain the late-time X-ray brightening found in several sources. We estimate the fraction of optically discovered TDEs with $L_{\text{X}} \geq 10^{42} \text{ erg s}^{-1}$ to be at least 40%, and find that the X-ray loudness is independent of black hole mass. We combine our sample with TDEs discovered by X-ray surveys to construct an X-ray luminosity function, which is best fitted by a broken power-law with a strong brake at $\sim 10^{44} \text{ erg s}^{-1}$. We show that there is no dichotomy between optically and X-ray selected TDE populations, and instead, there is a continuous distribution of early time $L_{\text{BB}}/L_{\text{X}}$, at least as wide as $L_{\text{BB}}/L_{\text{X}} \in (0.1, 3000)$, with optical/X-ray surveys selecting preferentially, but not exclusively, from the higher/lower end of the distribution. Our findings are consistent with the presence of an orientation-dependent and time-evolving reprocessing layer, and support viewing-angle unification models.

Keywords: Tidal disruption (1696) – X-ray transient sources (1852) – Supermassive black holes (1663) – Time domain astronomy (2109) – High energy astrophysics (739) – Accretion (14)

1. INTRODUCTION

The occasional tidal disruption of a star that approaches close enough to a massive black hole (MBH) was predicted by theorists as a signpost for MBHs lurking in the center of galaxies (Hills 1975; Rees 1988; Ulmer 1999). These luminous events, called tidal dis-

ruption events (TDE), are observed throughout the entire electromagnetic spectrum, and are now a well-established class of transients (see recent review by Gezari 2021). TDEs are a unique opportunity to probe the existence of quiescent black holes in the low mass end of the MBH’s mass function ($< 10^8 M_{\odot}$). At higher

black hole masses, a TDE is not observable; stars are swallowed whole since the tidal disruption radius lies inside the event horizon (Hills 1975; van Velzen 2018; Yao et al. 2023).

The first observational evidence for TDEs came from the detection of X-ray flares from the centers of quiescent galaxies during the *ROSAT* all-sky survey (RASS) in 1990–1991 (e.g., Bade et al. 1996; Grupe et al. 1999; Komossa & Greiner 1999; Greiner et al. 2000). The flares exhibited soft spectra with temperatures $T \sim 10^6$ K (for a review on X-ray selected TDEs, see Saxton et al. 2020). Since 2020, the Spektrum-Roentgen-Gamma (*SRG*) mission (Sunyaev et al. 2021), with its sensitive eROSITA telescope (Predehl et al. 2021), and six-month cadenced all-sky surveys, has become the most prolific discoverer of TDEs in X-rays, presenting thirteen new sources discovered during the first two All-sky scans (Sazonov et al. 2021).

The discovery of TDEs has increased dramatically in the last few years due to the operation of wide-field optical surveys, such as iPTF (Blagorodnova et al. 2017, 2019; Hung et al. 2017), Pan-STARRS (Gezari et al. 2012; Chornock et al. 2014; Holoien et al. 2019), ASASSN (Holoien et al. 2014, 2016a,b; Wevers et al. 2019a), and ZTF (van Velzen et al. 2019, 2021; Hammerstein et al. 2023a; Yao et al. 2023); with ZTF now dominating the number of discoveries with a rate of ~ 10 per year (Hammerstein et al. 2023a; Yao et al. 2023). Although, the number of optically selected TDEs dominates over the ones discovered by means of high-energy observations, the nature of what is powering their bright optical flares is uncertain. Unlike the soft X-ray component detected in some optically selected TDEs – which is similar to the X-ray selected TDEs and is consistent with thermal emission from the inner radii of an accretion disk – the UV/optical component seems, in most cases, not consistent with the direct emission from the Rayleigh-Jeans tail of the expected disk to form from the circularization of the stellar debris streams around a $10^5 - 10^8 M_\odot$ black hole. This implies the existence of an unknown, larger emitting structure that competing interpretations invoke to be either produced as a result of reprocessing of the extreme UV and X-ray emission (Miller et al. 2015; Dai et al. 2018; Parkinson et al. 2022; Thomsen et al. 2022), or from shocks between intersecting debris streams themselves (Piran et al. 2015; Jiang et al. 2016; Bonnerot et al. 2017).

Besides the origin of optical emission, a second important aspect of optically-selected TDEs is that most of them are X-ray faint. In the unifying reprocessing scenario, the distinct classes of TDEs are given by the viewing angle with respect to the accretion disk and its

associated reprocessing layer; the X-ray bright, ‘optically faint’ TDEs are the ones observed more face-on, the optically bright, X-ray faint are edge-on, while the ones that show both emission components are seen at intermediate angles (Guillochon et al. 2014; Dai et al. 2018; Parkinson et al. 2022). In this scenario, X-rays from sources at intermediate angles can only break out after the reprocessing gas has expanded enough to become transparent to X-rays (Metzger & Stone 2016; Lu & Kumar 2018; Thomsen et al. 2022). However, in the stream-stream collision scenario, the intrinsically X-ray faint TDEs have been proposed to be a result of delayed accretion, due to the timescale required for the circularization of the debris into an appreciable accretion disk (Gezari et al. 2017; Liu et al. 2019).

In addition to the study of nascent accretion disks, TDEs can be used to study the formation and evolution of other physical structures related to MBH accretion. Relativistic (e.g., Cenko et al. 2012; Pasham et al. 2015; Zauderer et al. 2011; Brown et al. 2017; Pasham et al. 2023) and non-relativistic (e.g., Alexander et al. 2016; Bright et al. 2018; Stein et al. 2021) jets, as well as outflows with velocities varying from 200–600 km s $^{-1}$ (Miller et al. 2015; Cenko et al. 2016; Blagorodnova et al. 2018; Kosec et al. 2023) up to $0.2c$ (e.g., Lin et al. 2015; Kara et al. 2018) have being detected in several sources.

This paper presents an analysis of the X-ray light curves, X-ray spectral evolution, and broadband UV/optical/X-ray spectral energy distribution (SED) evolution of 16 X-ray detected, optically discovered TDEs between 2014 and December 2021, and one more simultaneous discovered by *SRG*/eROSITA (AT2020ksf) but with extensive UV/optical follow-up. We present new *XMM-Newton* data for half of our sources and systematically reanalyze all publicly available ZTF, *Neil Gehrels Swift Observatory* and *XMM-Newton* data presented in previous studies on individual sources. In §2 we present our sample and our data. The data analyses are described in §3. In §4 we show our results and their interpretations, which are discussed in terms of the current literature in §5; our conclusion are presented in §6.

We adopt a standard Λ CDM cosmology with matter density $\Omega_M = 0.3$, dark energy density $\Omega_\Lambda = 0.7$, and the Hubble constant $H_0 = 70$ km s $^{-1}$ Mpc $^{-1}$. Optical and UV magnitudes are reported in the AB system. Uncertainties of X-ray model parameters are reported at the 68% confidence level, and upper limits are reported at 3σ .

2. SAMPLE, OBSERVATIONS AND DATA REDUCTION

2.1. Sample Selection

Aiming to explore the diversity of X-ray evolution in optically selected TDEs, we draw our sample from sources discovered by optical time-domain surveys. We compile sources from ZTF sample papers (van Velzen et al. 2021; Hammerstein et al. 2023b; Yao et al. 2023) as well as studies on individual sources from other surveys (Wyrzykowski et al. 2017; Holoien et al. 2016a,b; Wevers et al. 2019a). We did not consider nuclear transients with pre-existing active galactic nuclei (AGN) from TDE candidates, these excludes those with host galaxies with AGN-like broad emission lines or *neo WISE* (Mainzer et al. 2014) Mid Infrared (MIR) variability before the transient, as well as $W1 - W2$ MIR color exceeds AGN selection criteria (e.g., Stern et al. 2012). We limited the sample based on the epoch of discovery; given that the first optically discovered TDE to be systematically followed-up by X-ray telescopes was ASASSN-14li, we delimited the sample with sources discovered after 2014. Our discovery epoch criteria also exclude those sources discovered after December 2021, allowing us to have more than one year of data for the entire sample. Finally we require every source to have at least one 3σ *Swift*/XRT detection¹, yielding our final sample of 17 optically selected X-ray detected TDEs. The complete sample and the basic information on the sources are shown upper portion of Table 1. Besides the observations on the 17 sources that make our main sample, we also present deep upper-limits based on *XMM-Newton* observations of another 9 optically-selected TDEs that never show detectable X-ray emission; these sources are shown the bottom portion of Table 1.

2.2. XMM-Newton

The primary data set underlying this work is based on *XMM-Newton* observations, these were obtained primarily from a series of Announcement of Opportunity (AO) programs (AO-18 84259, AO-20 88259, P.I.: Gezari, and AO-21 90276 P.I. Yao) aimed on the deep X-ray follow-up of ZTF-discovered TDEs. These observations were taken in Full Frame mode with the thin filter using the European Photon Imaging Camera (EPIC; Strüder et al. 2001) and are presented here for the first time. We also included publicly available observations from several other AO and Director Discretionary Time

(DDT) proposals. The details on the *XMM-Newton* observations are shown in Table 2.

The observation data files (ODFs) were reduced using the *XMM-Newton* Standard Analysis Software (SAS; Gabriel et al. 2004). The raw data files were then processed using the `epproc` task. Since the pn instrument generally has better sensitivity than MOS1 and MOS2, we only analyze the pn data. Following the *XMM-Newton* data analysis guide, to check for background activity and generate “good time intervals” (GTIs), we manually inspected the background light curves in the 10–12 keV band. Using the `evselect` task, we only retained patterns that correspond to single and double events (`PATTERN<=4`). The source spectra were extracted using a source region of $r_{\text{src}} = 35''$ around the peak of the emission. The background spectra were extracted from a $r_{\text{bkg}} = 108''$ region located in the same CCD. The ARFs and RMF files were created using the `arfgen` and `rmfgen` tasks, respectively. Some of the observations for ASASSN-14li and AT2020ocn presented pile-up effects. Therefore, we followed the SAS guide² by excising the core of the point spread function (PSF), up to a radius where the pile-up fraction becomes negligible following the `epatplot` command results.

2.3. Neil Gehrels Swift Observatory

All the sources were observed by the X-ray Telescope (XRT; Burrows et al. 2005) and the Ultra-Violet/Optical Telescope (UVOT; Roming et al. 2005) on board *Neil Gehrels Swift Observatory* (Gehrels et al. 2004). The number of observations varies from a few for the more distant sources to a hundred for the most well-sampled sources. All *Swift* data were processed with `heasoft` v6.29c.

2.3.1. XRT

The 0.3–10 keV X-ray counts light curves were produced using the UK Swift Data center online XRT data products tool, which uses the HEASOFT v6.22 software (Arnaud 1996). We used a fixed aperture at the ZTF coordinate of the transient, generating one count rate point per visit (i.e., per ObsID) for most of the sources; for faint sources (AT2018zr, AT2018hyz and AT2019qiz), in which the count rate of individual visits were close to the XRT detection limit ($\sim 10^{-3}$ count s^{-1}) we stack few observations using the ‘dynamical binning’ as described in Evans et al. (2007), in order to obtain a smooth X-ray light curve.

¹ For the standard 2 ks observations this translate to a 0.3-10 keV flux greater than $few \times 10^{-13}$ erg cm^{-2} s^{-1}

² <https://www.cosmos.esa.int/web/xmm-newton/sas-thread-epatplot>

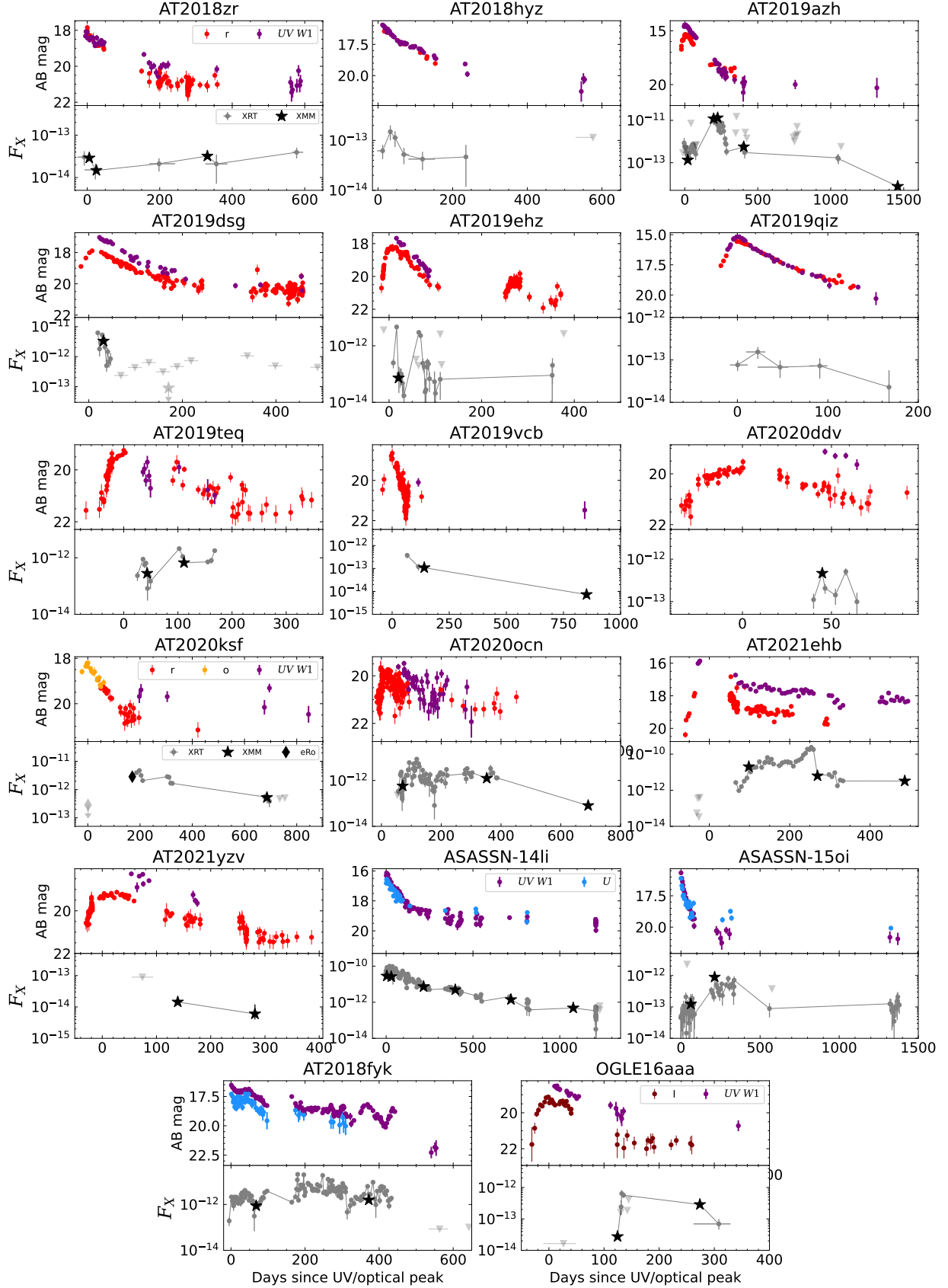


Figure 1. UV/Optical (top panels) and X-ray (bottom panels) light curves from our sample of 17 optically selected X-ray detected TDEs. On top panels we show ZTF r -band (red points), *Swift*/UVOT UV W1 band (purple points), ATLAS o -band (orange points) and OGLE I -band (maroon points), all in magnitudes in the AB system. On bottom panels we show the neutral absorption corrected 0.3-10 keV X-ray flux (F_X), *Swift*/XRT in grey points, *XMM-Newton* in stars and *SRG*/eROSITA in diamonds.

Table 1. Sample Information.

IAU	Discovery	Optical/UV peak	Redshift	$N_{H,G}$	$\log (M_*/M_\odot)^b$	σ_*	$\log(M_{BH}/M_\odot)^c$	TDE
Name	Name	(MJD)		$(10^{20} \text{ cm}^{-2})^a$		(km s^{-1})		Classification
AT2018zr	ZTF18aabtxvd	58214	0.071	4.17	$10.01^{+0.08}_{-0.14}$	$49 \pm 5^{(d)}$	5.83 ± 0.51	ATel #11444
AT2018hyz	ASASSN-18zj	58422	0.045	2.59	$9.96^{+0.09}_{-0.16}$	$57 \pm 1^{(e)}$	6.12 ± 0.46	ATel #12198
AT2019azh	ASASSN-19dj	58558	0.022	4.15	$9.74^{+0.08}_{-0.05}$	$77 \pm 2^{(f)}$	6.68 ± 0.46	ATel #12568
AT2019dsg	ZTF19aapreis	58600	0.051	6.46	$10.55^{+0.09}_{-0.12}$	$94 \pm 1^{(g)}$	7.04 ± 0.45	ATel #12752
AT2019ehz	Gaia19bpt	58611	0.074	1.42	$9.65^{+0.09}_{-0.12}$	$47 \pm 11^{(d)}$	5.75 ± 0.59	ATel #12789
AT2019qiz	ZTF19abzrhgq	58764	0.015	6.35	$10.01^{+0.09}_{-0.12}$	$70 \pm 2^{(h)}$	6.49 ± 0.46	ATel #13131
AT2019teq	ZTF19accmaxo	58794	0.087	4.54	$9.95^{+0.07}_{-0.11}$...	6.32 ± 0.49	TNSCR #7482
AT2019vcb	ZTF19acspeuw	58838	0.088	1.45	$9.49^{+0.06}_{-0.06}$...	5.59 ± 0.52	TNSCR #7078
AT2020ddv	ZTF20aamqmfk	58915	0.16	1.35	$10.30^{+0.13}_{-0.16}$	$57 \pm 10^{(d)}$	6.09 ± 0.55	ATel #13655
AT2020ksf	Gaia20cjk	58976	0.092	3.61	$10.12^{+0.13}_{-0.09}$	$52 \pm 2^{(i)}$	5.92 ± 0.48	Gilfanov et al. (2020)
AT2020ocn	ZTF18aakelin	58972	0.07	1.28	$10.28^{+0.13}_{-0.70}$	$81 \pm 8^{(d)}$	6.77 ± 0.49	ATel #13859
AT2021ehb	ZTF21aanxhvj	59330	0.018	9.88	$10.18^{+0.01}_{-0.02}$	$93 \pm 5^{(j)}$	7.04 ± 0.46	TNSCR #10001
AT2021yzv	ZTF21abxngcz	59475	0.286	8.60	$10.65^{+0.04}_{-0.06}$...	7.45 ± 0.47	TNSCR #11890
...	ASASSN-14li	56993	0.02	1.95	$9.68^{+0.04}_{-0.09}$	$81 \pm 2^{(k)}$	6.77 ± 0.46	ATEL #6777
...	ASASSN-15oi	57259	0.048	4.86	$10.02^{+0.04}_{-0.03}$...	6.42 ± 0.48	ATEL #7936
AT2018fyk	ASASSN-18ul	58389	0.059	1.16	$10.56^{+0.21}_{-0.12}$	$158 \pm 1^{(l)}$	8.04 ± 0.44	TNSCR #2723
...	OGLE16aaa	57403	0.165	2.72	$10.47^{+0.09}_{-0.11}$...	7.14 ± 0.48	Wyrzykowski et al. (2017)
AT2018bsi	ZTF18aahqkbtr	58389	0.051	4.91	$10.62^{+0.05}_{-0.07}$	$118 \pm 8^{(d)}$	7.48 ± 0.46	ATel #12035
AT2018hco	ATLAS18way	58479	0.088	4.12	$10.01^{+0.12}_{-0.16}$...	6.40 ± 0.49	ATel #12263
AT2018iih	ATLAS18yys	58558	0.212	3.19	$10.81^{+0.11}_{-0.14}$...	7.70 ± 0.48	van Velzen et al. (2021)
AT2018lna	ZTF19aabbnzo	58561	0.091	6.42	$9.56^{+0.08}_{-0.14}$	$36 \pm 4^{(d)}$	5.20 ± 0.53	ATel #12509
AT2019mha	ZTF19abhejal	58705	0.148	1.71	$10.01^{+0.14}_{-0.18}$...	6.41 ± 0.49	van Velzen et al. (2021)
AT2019meg	ZTF19abhhjcc	58743	0.152	5.08	$9.64^{+0.07}_{-0.08}$...	5.81 ± 0.52	AN-2019-88
AT2020pj	ZTF20aabqihu	58866	0.068	2.24	$10.01^{+0.07}_{-0.08}$...	6.43 ± 0.49	TNSCR #7481
AT2020vwl	ZTF20achpcvt	59167	0.032	2.23	$9.89^{+0.08}_{-0.08}$...	6.21 ± 0.49	TNSCR #8572
AT2020wey	ZTF20acitpfz	59156	0.027	6.19	$9.67^{+0.09}_{-0.12}$	$39 \pm 3^{(d)}$	5.38 ± 0.51	TNSCR #7769

NOTE—Top: X-ray detected TDE (main sample). Bottom: X-ray non-detected TDEs with new deeper upper-limits. Abbreviations ATel corresponding to the Astronomer’s Telegram (<https://astronomerstelegram.org>), AN corresponding to AstroNotes (<https://www.wis-tns.org/astronotes>), and TNSCR corresponding to TNS classification reports. a) Galactic absorption column density from HI4PI Collaboration et al. (2016); b) Host galaxy stellar mass from SED fitting (see 3.1); c) Black hole masses. When a σ_* measurement is available it is estimated using the Gültekin et al. (2019) $\sigma_* - M_{BH}$ relation, when σ_* is not available, this is estimated from the $M_* - M_{BH}$ relation presented in Yao et al. (2023). d) Hammerstein et al. (2023b); (e) Short et al. (2020); f) Liu et al. (2019); g) Cannizzaro et al. (2021); h) Nicholl et al. (2020); i) Wevers et al., in prep; j) Yao et al. (2022); k) Wevers et al. (2019b); l) Wevers et al. (2019a)

The short XRT exposures do not allow for spectral fitting of individual visits, so we stacked consecutive observations using an automated online tool³ (Evans et al. 2009). We aimed to have at least 100 counts per stacked spectrum, allowing the bins to be at maximum 100 days long, we also ensure there was no large evolution in the hardness ratio within each bin. Spectral fitting will be detailed in §3.3. For AT2018zr, AT2019vcb, AT2020ddv and ASASSN-15oi there were not enough counts to generate a fitable spectrum, even combining all the XRT observations, therefore we restrict our XRT analysis on their light curves and only perform spectral analysis in their *XMM-Newton* data.

2.3.2. UVOT

We used the `uvotsource` package to analyze the Swift UVOT photometry, using an aperture of 5'' for all sources except AT2019azh, AT2019qiz, and AT2019dsg, which required a larger aperture to capture the host galaxy light. We subtracted the host galaxy flux estimated from the population synthesis modeling of archival pre-event photometry described in §3.1. We apply Galactic extinction correction on all bands using $E(B - V)$ values at the position of each source from Schlafly & Finkbeiner (2011).

2.4. Zwicky Transient Facility

We performed point spread function (PSF) photometry on all publicly available ZTF data using the ZTF forced-photometry service (Masci et al. 2019, 2023) in g - and r -band. Similar to UVOT, ZTF photometry was corrected for Galactic extinction.

2.5. Additional Data

OGLE16aaa was discovered by the fourth phase of the Optical Gravitational Lensing Experiment (OGLE-IV, Udalski et al. 2015) survey, we added the I band (7970 Å) data, which is the best sampled optical light curve of the source; the data was retrieved from the survey website⁴.

The optical peak of AT2020ksf was missed by ZTF, however the Asteroid Terrestrial-impact Last Alert System (ATLAS, Tonry et al. 2018) started observing the field containing the source ~60 days before ZTF, hence allowing us to measure the date of its optical peak; we added available ATLAS data to our light curve of AT2020ksf. The source was first detected in the X-rays

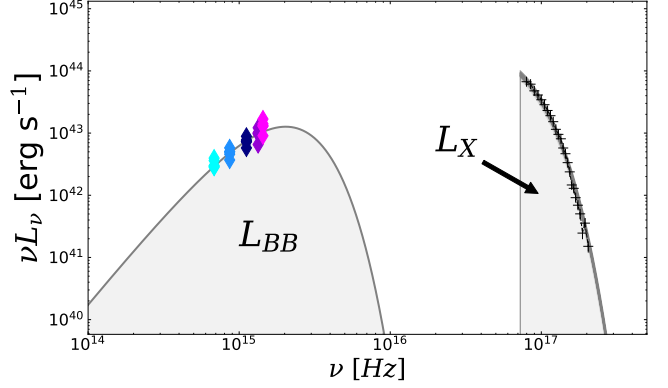


Figure 2. Illustration of how the UV/optical blackbody luminosity (L_{BB}) and the 0.3-10 keV X-ray luminosity (L_X) are measured and what those values represent regarding the full SED of the transient. Colored points indicate observed UV/optical photometry, underline it the best-fitting blackbody function is shown in dark gray, and the area below the curve is the measured L_{BB} . The black crosses show the observed X-ray spectra and best-fitted X-ray model, and the measured L_X is also shown in gray. Both UV/optical and X-ray components are corrected for Galactic extinction/absorption.

by the *SRG*/eROSITA, although the spectral data is not yet publicly available, we added the reported detection flux of $1.7 \times 10^{-12} \text{ erg cm}^{-2} \text{ s}^{-1}$ ($2.85 \times 10^{-12} \text{ erg cm}^{-2} \text{ s}^{-1}$ unabsorbed) observed in 20th November 2020 (MJD 59162), as well as the previous X-ray upper limit ($\leq 2.85 \times 10^{-13} \text{ erg cm}^{-2} \text{ s}^{-1}$) from a visit taken on 8th May 2020 (MJD 58977) which is fortuitously timed at the optical peak of the source, both reported by Gilfanov et al. (2020).

3. DATA ANALYSES

3.1. Host Galaxy SED modelling

Before analyzing the transient's UV/optical light curve, the host contamination needs to be subtracted. We followed van Velzen et al. (2021) prescription to fit the host galaxy pre-flare photometry. We compile the host galaxy spectral energy distribution (SED) using archival observations in the UV through IR bands. We use the `Prospector` software (Johnson et al. 2021) to run a Markov Chain Monte Carlo (MCMC) sampler (Foreman-Mackey et al. 2013) to obtain the posterior distributions of the Flexible Stellar Population Synthesis models (Conroy et al. 2009). We adopted a simple power law star formation history, with the same ranges and priors as in van Velzen et al. (2021), for the 5 free parameters: stellar mass, Calzetti et al. (2000) dust model optical depth, stellar population age, metallicity, and the e-folding time of the star formation history. The resulting host stellar mass (M_*) are presented in Table

³ https://www.swift.ac.uk/user_objects

⁴ <http://ogle.astrouw.edu.pl/ogle4/transients/2017a/transients.html>

Table 2. Summary of *XMM-Newton* Observations

Source	Obs ID	Obs Date	phase (Δt) ^a	$\log F_X^c$	$\log L_X^c$	L_{BB} / L_X	First
		MJD	(days)	(erg cm ² s ⁻¹)	(erg s ⁻¹)		presented in
AT2018zr	0822040301	58220	5	$-13.538^{+0.040}_{-0.045}$	$41.610^{+0.040}_{-0.045}$	$95.46^{+9.26}_{-9.30}$	van Velzen et al. (2019)
	0822040501	58241	25	$-13.831^{+0.052}_{-0.059}$	$41.317^{+0.052}_{-0.059}$	$127.48^{+16.28}_{-16.24}$	
	0822040401	58569	331	$-13.493^{+0.033}_{-0.036}$	$41.656^{+0.033}_{-0.036}$	$12.38^{+0.99}_{-1.00}$	this work
AT2019azh	0822041101	58579	20	$-12.872^{+0.016}_{-0.017}$	$41.178^{+0.016}_{-0.017}$	$889.10^{+34.07}_{-34.09}$	this work
	0842591001	58760	197	$-10.924^{+0.002}_{-0.002}$	$43.125^{+0.002}_{-0.002}$	$0.58^{+0.01}_{-0.01}$	
	0823810401	58788	4	$-10.881^{+0.001}_{-0.001}$	$43.168^{+0.001}_{-0.001}$	$0.41^{+0.01}_{-0.01}$	
	0842592601	58971	404	$-12.248^{+0.013}_{-0.014}$	$41.801^{+0.013}_{-0.014}$	$2.14^{+0.07}_{-0.07}$	
	0902761101	60049	1458	$-14.114^{+0.116}_{-0.158}$	$39.936^{+0.116}_{-0.158}$...	
AT2019dsg	0842590901	58633	31	$-11.483^{+0.004}_{-0.004}$	$43.316^{+0.004}_{-0.004}$	$3.16^{+0.03}_{-0.03}$	Stein et al. (2021)
	0842591901	58779	170	< -13.046	< 41.753	> 15.99	
AT2019ehz	0842590801	58633	20	$-13.138^{+0.022}_{-0.023}$	$41.998^{+0.022}_{-0.023}$	$50.89^{+2.63}_{-2.63}$	this work
AT2019teq	0842591701	58841	43	$-12.549^{+0.011}_{-0.012}$	$42.736^{+0.011}_{-0.012}$	$2.25^{+0.06}_{-0.06}$	this work
	0842592401	58915	111	$-12.173^{+0.005}_{-0.006}$	$43.111^{+0.005}_{-0.006}$	$0.49^{+0.01}_{-0.01}$	
AT2019vcb	0871190301	58991	140	$-12.967^{+0.020}_{-0.021}$	$42.339^{+0.020}_{-0.021}$	$1.71^{+0.08}_{-0.08}$	Quintin et al. (2023)
	0882591401	59764	851	$-14.136^{+0.106}_{-0.150}$	$41.169^{+0.106}_{-0.150}$	$7.12^{+1.97}_{-2.08}$	
AT2020ddv	0842592501	58967	44	$-12.332^{+0.008}_{-0.008}$	$43.523^{+0.008}_{-0.008}$	$5.05^{+0.09}_{-0.09}$	this work
AT2020ksf	0882591201	59725	749	$-12.280^{+0.009}_{-0.010}$	$43.057^{+0.009}_{-0.010}$	$2.92^{+0.06}_{-0.06}$	this work
AT2020ocn	0863650101	59048	76	$-12.238^{+0.005}_{-0.006}$	$42.848^{+0.005}_{-0.006}$	$1.42^{+0.02}_{-0.02}$	Pasham et al., in prep
	0872392901	59349	377	$-11.902^{+0.004}_{-0.004}$	$43.183^{+0.004}_{-0.004}$	$0.06^{+0.01}_{-0.01}$	
	0902760701	59712	685	$-13.094^{+0.020}_{-0.021}$	$41.991^{+0.020}_{-0.021}$	$2.73^{+0.13}_{-0.13}$	this work
AT2021ehb	0882590101	59430	98	$-10.696^{+0.003}_{-0.004}$	$43.177^{+0.003}_{-0.004}$	$0.49^{+0.01}_{-0.01}$	Yao et al. (2022)
	0882590901	59604	269	$-11.203^{+0.003}_{-0.003}$	$42.670^{+0.003}_{-0.003}$	$0.52^{+0.01}_{-0.01}$	
	0902760101	59825	486	$-11.489^{+0.006}_{-0.006}$	$42.384^{+0.006}_{-0.006}$	$0.67^{+0.01}_{-0.01}$	this work
AT2021yzv	0882591001	59654	139	$-13.844^{+0.054}_{-0.062}$	$42.580^{+0.054}_{-0.062}$	$99.26^{+13.22}_{-13.19}$	this work
	0882591501	59837	281	$-14.222^{+0.301}_{-0.176}$	$42.204^{+0.301}_{-0.176}$	$68.48^{+68.48}_{-22.83}$	
ASASSN-14li	0694651201	56997	3	$-10.549^{+0.002}_{-0.002}$	$43.442^{+0.002}_{-0.002}$	$2.33^{+0.01}_{-0.01}$	Miller et al. (2015)
	0694651401	57023	29	$-10.588^{+0.002}_{-0.002}$	$43.403^{+0.002}_{-0.002}$	$1.31^{+0.01}_{-0.01}$	Kara et al. (2018)
	0694651501	57213	215	$-11.135^{+0.004}_{-0.004}$	$42.856^{+0.004}_{-0.004}$	$0.78^{+0.01}_{-0.01}$	
	0770980501	57399	397	$-11.312^{+0.005}_{-0.005}$	$42.679^{+0.005}_{-0.005}$	$0.49^{+0.01}_{-0.01}$	this work
	0770980701	57726	718	$-11.855^{+0.007}_{-0.008}$	$42.136^{+0.007}_{-0.008}$	$2.04^{+0.04}_{-0.04}$	
	0770980901	58092	1076	$-12.318^{+0.008}_{-0.009}$	$41.673^{+0.008}_{-0.009}$	$5.13^{+0.10}_{-0.10}$	
	0722160501	57324	62	$-12.907^{+0.027}_{-0.029}$	$41.837^{+0.027}_{-0.029}$	$77.94^{+5.07}_{-5.06}$	
ASASSN-15oi	0722160701	57482	212	$-12.051^{+0.011}_{-0.011}$	$42.693^{+0.011}_{-0.011}$	$1.22^{+0.03}_{-0.03}$	Gezari et al. (2017)
AT2018fyk	0831790201	58461	67	$-12.056^{+0.005}_{-0.005}$	$42.874^{+0.005}_{-0.005}$	$29.62^{+0.31}_{-0.31}$	Wevers et al. (2021)
	0853980201	58783	372	$-11.803^{+0.003}_{-0.003}$	$43.127^{+0.003}_{-0.003}$	$2.97^{+0.02}_{-0.02}$	
OGLE16aaa	0790181801	57548	124	$-13.563^{+0.056}_{-0.064}$	$42.322^{+0.056}_{-0.064}$	$15.06^{+2.06}_{-2.06}$	Kajava et al. (2020)
	0793183201	57722	273	$-12.543^{+0.012}_{-0.012}$	$43.342^{+0.012}_{-0.012}$	$0.49^{+0.01}_{-0.01}$	
AT2018bsi	0822040801	58389	164	< -13.453	< 41.319	> 42	this work
AT2018hco	0822040901	58479	71	< -13.974	< 41.312	> 291	this work
AT2018iih	0822040701	58558	95	< -14.250	< 41.867	> 254	this work
AT2018lna	0822041001	58561	48	< -14.057	< 41.260	> 309	this work
AT2019mha	0842592201	58705	33	< -14.288	< 41.483	> 43	this work
AT2019meg	0842592101	58743	40	< -13.919	< 41.878	> 82	this work
AT2020wey	0902760401	59851	676	-13.0857	41.1449	...	this work
AT2020pj	0902760801	59809	882	-13.5102	41.5488	...	this work
AT2020vwl	0902760301	59776	590	-13.568	40.8932	...	this work

NOTE—a) Relative to the rest-frame UV/optical peak; b) 0.3-10.0 keV band, upper limits are 3σ .

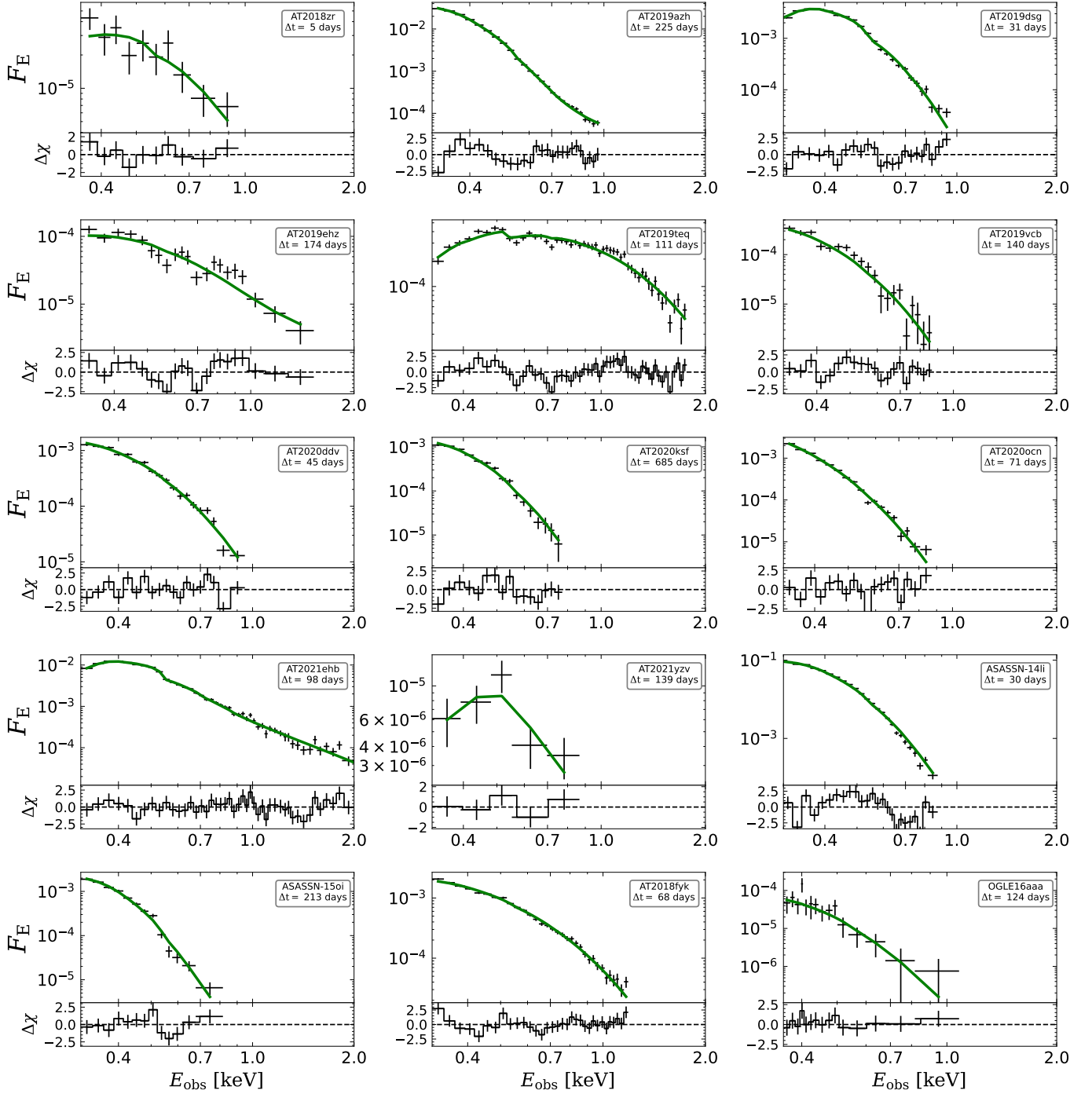


Figure 3. Representative unfolded spectra, best-fit model and residuals for all the source with available *XMM-Newton* data in our sample. Top panels shows the unfolded spectra in black and the best-fitting model in green (either `tdediscspec` or `simPL@tdediscspec`) in units of $\text{keV cm}^{-2} \text{s}^{-1} \text{keV}^{-1}$. Bottom panels show the residuals in $\Delta\chi$.

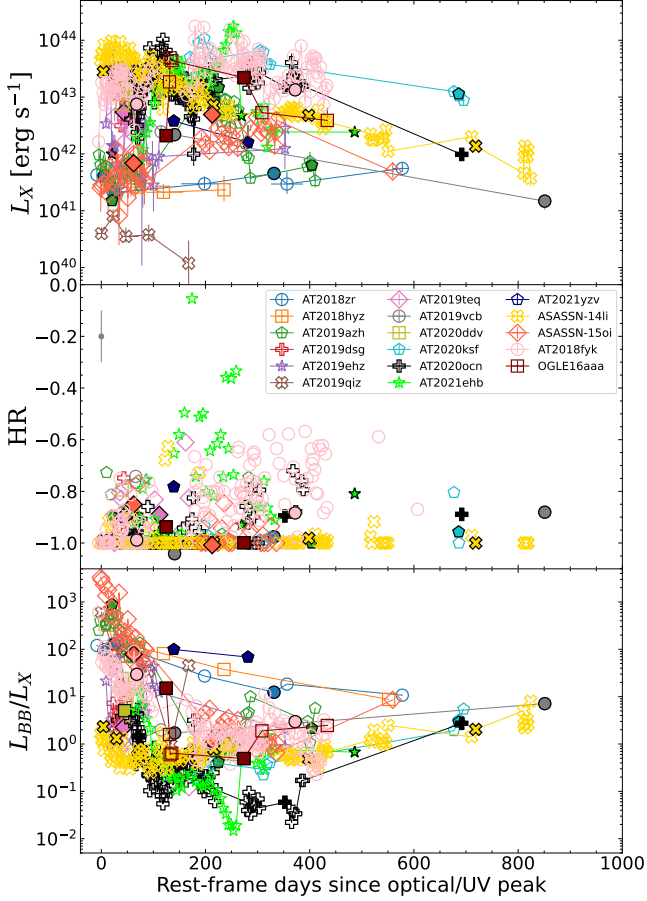


Figure 4. Observed X-ray properties as function of time. From Top to Bottom: 0.3-10 keV absorption correct luminosity (L_X), hardness ratio (HR), and UV/optical blackbody luminosity to X-ray luminosity ratio (L_{BB}/L_X). Hollow points show *Swift*/XRT observations and solid markers show the *XMM-Newton* observations.

1, the fitting for all host galaxies of our sample are presented either in van Velzen et al. (2021), Hammerstein et al. (2023a) or Yao et al. (2023), the reader is referred to these papers for the full list of best-fitting parameters. We subtract the host contribution to the transient’s UVOT filter’s photometry. The UVW1 band (2600 Å, observed frame) host-subtracted light curves are shown in the top panels of Figure 1 for individual sources.

3.2. UV/optical

Following the standard approach for optical TDEs (e.g., van Velzen et al. 2021; Hammerstein et al. 2023a) we estimate the integrated UV/optical luminosity (L_{BB}) by fitting the transient UV/optical SED with an evolving, Gaussian rise and power law decay, blackbody (BB) function. The model can be written as:

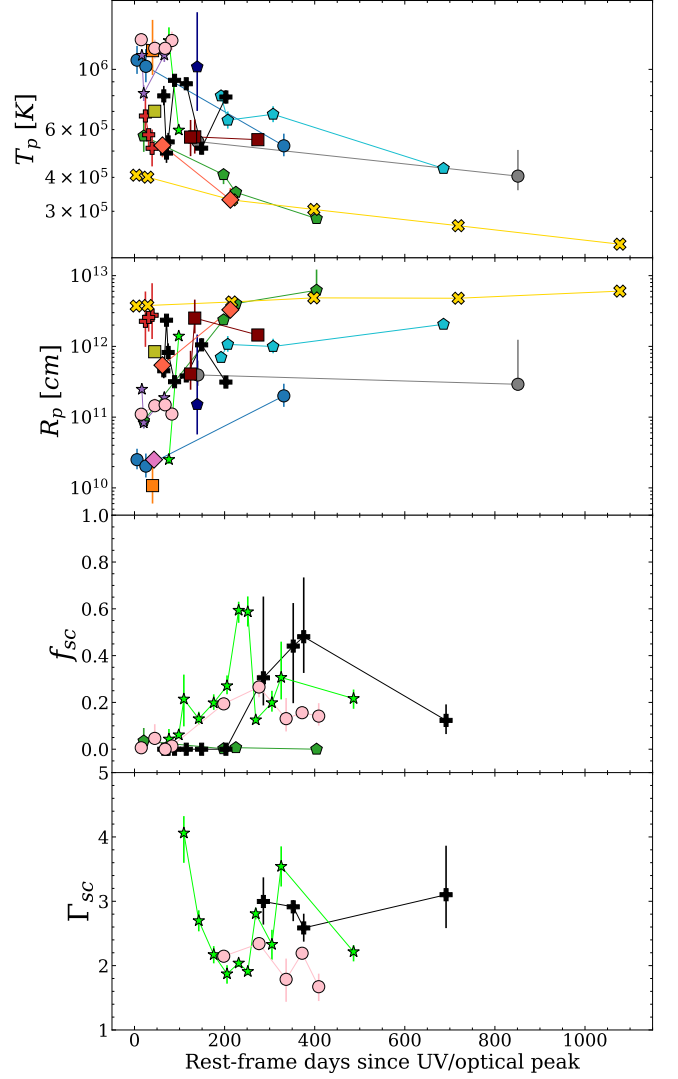


Figure 5. Best-fitting parameters from X-ray spectral modeling as function of time from the UV/optical peak. From top to bottom: Peak temperature (T_p) and Radius (R_p) from *tdediscspec*; fraction of comptonized photons (f_{sc}) and power-law photon index (Γ_{sc}) of *simPL*.

$$L_{BB}(t) = L_{BB,peak} \frac{\pi B_\nu(T(t))}{\sigma_{SB} T^4(t)} \times \begin{cases} e^{-(t-t_{peak})^2/2\sigma^2}, & t \leq t_{peak} \\ [(t-t_{peak})/t_0]^p, & t > t_{peak} \end{cases} \quad (1)$$

We consider a non-parametric temperature evolution; we fit the temperature at grid points spaced ± 30 days apart beginning at peak and use a log-normal Gaussian prior at each grid point. We use a Gaussian likelihood function to estimate the parameters of the models above; we use the *emcee* sampler (Foreman-Mackey et al. 2013). Details on the fitting process and resulting UV/optical integrated light curves can be seen in either van Velzen et al. (2021) or Hammerstein et al. (2023a)

for all the sources. The time dependent model assumed in Eq. 1, was assumed for the first 350 days of the optical light curve, after that the light curve shape usually deviates from the power-law decay (van Velzen et al. 2021; Hammerstein et al. 2023a). For the later epochs, we measured the integrated UV/optical luminosity by fitting again with a blackbody function for the available UV/optical photometry data, epoch by epoch, when L_{BB} measurements were necessary (see §4). In Fig. 2, we illustrate what fitting a blackbody to the UV/optical broad-band photometric data means in terms of the full SED of the transient; it also illustrates how misleading it can be to interpret L_{BB} as a ‘bolometric’ luminosity, as is commonly done by some authors; such aspects will be further explored in §4.3.

3.3. X-rays

The following procedures were done using the python version of **xspec** (Arnaud 1996), **pyxspect**⁵. For all spectral models described below, we included the Galactic absorption using the **TBabs** model (Wilms et al. 2000), with the hydrogen-equivalent neutral column density N_H fixed at the values shown in Table 2 (HI4PI Collaboration et al. 2016). We shifted the TDE emission using the convolution model **zshift**, with the redshift z shown in Table 1.

3.3.1. XMM-Newton and Swift/XRT spectral fitting

In most cases, the X-ray spectra of TDEs are super-soft, with very few to no photons detected at energies higher than 2 keV. A visual inspection of our *XMM-Newton* observations confirms this trend for our optically detected X-ray bright TDEs sample. Fitting such soft spectra with a phenomenological **powerlaw** model like in AGN usually results in best-fitted Γ parameter higher than 5; such high values are nonphysical in the case of inverse up-scattering of seed photons by a hot corona (Titarchuk & Lyubarskij 1995) and hence do not represent any meaningful physical measurement. Nevertheless, fitting with **powerlaw** may be useful to differentiate X-ray TDE spectra from AGN ones, as we will show in §4.2.

In low signal-to-noise ratio (S/N) observations, these super-soft spectra are usually fitted using a single temperature blackbody model, **blackbody** or **bbodyrad** in **xspec**. However, for higher S/N observations, a multi-temperature model usually associated with a geometrically thin accretion disk fits the data better than the single-temperature models (Saxton et al. 2020; Mummery 2021). In these cases, the **diskbb** model (Shakura

& Sunyaev 1973; Mitsuda et al. 1984) developed for stellar black holes in X-ray binaries (XRB) is usually employed.

Recently, Mummery (2021) developed a model specifically tailored for TDE accretion disks; the author based their modeling on the fortunate property of TDE disks being relatively cool, with their spectra peaking below the low bandpass of X-ray telescopes, $kT \leq 0.3$ keV. This means that X-ray observations of TDE disks probe the quasi-Wien tail of the disk spectrum; hence no assumption about the disk temperature profile needs to be made; instead, the only assumption inherent to the model is that each disk radius emits like a color-corrected blackbody and that there exists some disk radius where the disk temperature peaks. The **xspec** model, called **tdediscspec**, fits the following expression to the observed X-ray spectra (Mummery 2021; Mummery & Balbus 2021):

$$F_\nu(R_p, \tilde{T}_p, \gamma) \simeq \frac{4\pi\xi_1 h\nu^3}{c^2 f_{\text{col}}^4} \left(\frac{R_p}{D}\right)^2 \left(\frac{k\tilde{T}_p}{h\nu}\right)^\gamma \exp\left(-\frac{h\nu}{k\tilde{T}_p}\right) \quad (2)$$

Where $\tilde{T}_p \equiv f_{\text{col}} f_\gamma T_p$, and T_p is the parameter of interest, i.e., the hottest temperature in the accretion disc. The factor f_ν is the photon energy-shift factor, defined as the ratio of the observed photon frequency ν to the emitted photon frequency ν_{emit} , $f_\gamma = \nu/\nu_{\text{emit}} \approx 1/\sqrt{2}$ (see Mummery & Balbus 2021, and reference therein for details), while f_{col} is the ‘color-correction’ factor, which is included to model disk opacity effects. This correction factor generally takes a value $f_{\text{col}} \sim 2.3$ for typical TDE disk temperatures (Done et al. 2012; Mummery 2021; Mummery et al. 2023), which is the value assumed in the **tdediscspec** model. The radius R_p is a normalization parameter that corresponds to radius of the hottest region. The constant γ depends on assumptions about both the inclination angle of the disk and the disk’s inner boundary condition and is limited to the range $1/2 \leq \gamma \leq 3/2$. The properties of γ are discussed in more detail in Mummery (2021) and references therein. In practice, the observed accretion disk spectrum is only weakly dependent on γ , which cannot be strongly constrained from observations (Mummery 2021). In this model, γ is therefore treated as a nuisance parameter, letting it vary between its allowed limits for each source. In fact, the $1-\sigma$ uncertainties on γ typically fill the entire permitted range, and as such, the γ parameter merely extends the uncertainty range of the parameters T_p and R_p .

⁵ <https://heasarc.gsfc.nasa.gov/xanadu/xspec/python>

We compare the single temperature **blackbody** to **tdediscspec**, most spectra are better fitted (smaller $\chi^2/d.o.f$) by the latter, only for the low S/N spectra the quality of the fits are comparable, furthermore, as demonstrated in Mummery (2021), **blackbody** may result in unphysical size (or radius) of the emitting region. Therefore, we select **tdediscspec** as our primary model for the soft emission.

For several sources/epochs, when fitted only with a soft component, a large residual at higher energies is present, this usually results in a poor fit, $\chi^2/d.o.f > 2.0$. Such ‘hard excess’ is well described by a power-law function and was already reported for both X-ray (e.g., Saxton et al. 2017) and optically selected TDEs (e.g., Wevers et al. 2021; Yao et al. 2022), and is associated with Compton up-scattering of the soft photons by a corona of hot electrons near the accretion disk (Titarchuk & Lyubarskij 1995).

In AGN, this component is the dominant component of their X-ray spectra and is modeled with a phenomenological model ($F(E) \propto E^{-\Gamma}$, **powerlaw** in **xspec**). However, for soft and intermediate state XRBs, which in contrast to AGN and similar to TDEs, have both their main continuum and the power-law in the X-ray band, a more physically motivated and self-consistent model was developed by Steiner et al. (2009) to describe the Comptonization process, called **simPL** in **xspec**. The model has two free parameters, f_{sc} ⁶ and Γ_{sc} ⁷; the first is the fraction of photons from the soft component that are up-scattered to create the power-law, and the second is the photon index of the resulting power-law. A more detailed discussion on using **simPL** on X-ray TDE spectra is presented in Appendix §A.

We employ the models described above, either **tdediscspec** or **simPL**⊗**tdediscspec**, depending on the need for the ‘hard tail’, based on a simple $\chi^2/d.o.f$ analysis. Therefore, our X-ray modeling has either two free parameters (T_p and R_p), if fitted only with **tdediscspec**, or four free parameters (T_p , R_p , f_{sc} and Γ_{sc}) if fitted with **simPL**⊗**tdediscspec**. We also check whether an additional intrinsic neutral absorption was necessary by adding a **zTBabs** component to the model, only for ASASSN-14li and AT2019dsg, N_H ’s of respectively $\sim 5 \times 10^{20} \text{ cm}^{-2}$ and $\sim 3 \times 10^{20} \text{ cm}^{-2}$, significantly improve the residuals at the most soft energies, and were

added to the final model. For all other sources the intrinsic absorption component was negligible to the fit quality which constraint their intrinsic N_H to be $\ll 10^{20} \text{ cm}^{-2}$.

We start by fitting *XMM-Newton* spectra which were grouped to have at least 25 counts per bin, but limiting the over-sampling of the instrumental resolution to a factor of 5; we assume a χ^2 -statistics. For *Swift*/XRT data fitting, the stacked spectra were grouped to have at least 1 count per bin; we assume a C-statistics (Cash 1979). To convert the count rate of each visit to flux, we assume the closest in time best-fit model to the stacked spectra. We check for the convergence of the fitting using the **steppar** command in **xspec**. The stacked *Swift*/XRT spectrum of AT2019qiz and the second *XMM-Newton* epoch of AT2019ehz show a divergent degeneracy between some of the model parameters, hence no uncertainties on the parameters could be determined and therefore no interpretation of the derived best-fitting parameters will be done, although we use the best-fitted parameters to scale the count-rates to flux/luminosity. The measured temperature of second epoch of AT2019teq is hotter than the T_p maximum limit on quasi-Wien approximation of **tdediscspec**, similarly no physical interpretation is attributed from the derived physical parameter of this epoch.

A representative *XMM-Newton* observation and modeled spectra, as well as residuals for each source, are shown in Fig. 3. In figure 5, we show the best-fit value and its evolution for all four parameters in our modeling. These models fit very well the continuum of most observations ($\chi^2/d.o.f \sim 1.0$). However, some sources present features that resemble absorption lines, usually associated with O VII ($\sim 0.54 \text{ keV}$) and/or O VIII ($\sim 0.65 \text{ keV}$); these can be highly blueshifted (up to $0.2c$) and interpreted as ultra fast outflows (UFO, e.g., Kara et al. 2018). We will explore these absorption lines’ detection, physical interpretation, and modeling in separate publications for those sources in which the statistical significance of the absorption detection can be assured.

3.4. Black Hole Masses

The black holes masses (M_{BH}) of the TDE hosts were estimated from the host galaxy scaling relations. If a measurement of the velocity dispersion (σ_*) of their nuclear stellar populations were publicly available (e.g., Wevers et al. 2019b; Yao et al. 2023) M_{BH} was estimated from $\sigma_* - M_{\text{BH}}$ relation by Gültekin et al. (2019). Alternatively, if σ_* was not available, M_{BH} was estimated from the host galaxy mass (M_* , as measured from 3.1) using the relation presented in Yao et al. 2023. The σ_* , M_* and M_{BH} values are shown in Table 1. Uncertainties

⁶ This should not be confused with the fractional flux of the power-law with respect to the total flux, at $f_{sc} \sim 0.3$ the total flux is already dominated by the powerlaw component as shown in §A.

⁷ We will use Γ_{sc} for the power-law photon index when the TDE X-ray spectra are fitted with **simPL**⊗**tdediscspec**, and Γ when the spectra are fitted with **powerlaw** model.

in M_{BH} are the result of the addition in quadrature of the statistical uncertainty of σ_*/M_* and the systematic spread of the scaling relations, and are usually ~ 0.5 dex.

4. RESULTS

The main results of the X-ray and UV/optical fitting are present in Fig. 4 and Fig. 5 as a function of time since the UV/optical peak. In Fig. 4, we show, from top to bottom panel: the neutral absorption corrected 0.3-10 keV Luminosity (L_X); the hardness ratio (HR) defined as $\text{HR} = (H - S)/(H + S)$, where S is the 0.3-2.0 keV count rate and H is the 2.0-10.0 keV count rate and the ratio (L_{BB}/L_X) between the UV/optical integrated luminosity (L_{BB} , Eq. 1) and L_X .

In Fig. 5, we show the best-fitting parameters from the X-ray spectral fitting (see §3.3), first the main parameters of `tbabspec`, the peak temperature (T_p) and apparent radius in which T_p occurs (R_p), and for the power-law component (`simPL`), the fraction of the comptonized photons (f_{sc}) and the photon index of the power-law (Γ_{sc}), the later is only shown for three sources (AT2018fyk, AT2020ocn, AT2021ehb) in which a strong enough power-law is detected at some epoch (i.e., $f_{sc} \geq 0.1$), given the high uncertainty in Γ when the component is only marginally detected. We also do not show the measurements of T_p and R_p for the epochs in which $f_{sc} \geq 0.2$ given that the power-law emission completely dominates the spectra; hence no trustworthy information on the underline thermal emission can be recovered, as discussed in §A.

4.1. Diversity of X-ray light curves

A surprising characteristic of optically discovered X-ray bright TDEs – first observed in ASASSN-15oi by Gezari et al. (2017) – is that their X-ray light curve does not necessarily follow the theoretically expected fallback rate ($\propto t^{-5/3}$, Rees 1988), not even a more general lower-law decay ($\propto t^{-\alpha}$), which is now established as the general evolution of their optical component (Hammerstein et al. 2023a). Instead, a wide diversity of time evolution and luminosity ranges are observed in the X-rays as shown by the top panel of Fig. 4. This diversity also means that the time evolution of the relation between the UV/optical and X-ray components also evolves in distinct ways in different sources, as shown by the bottom panel of Fig. 4. To search for a general picture of such diversity, we classified the sources in groups with similar evolution in terms of L_X and L_{BB}/L_X ; in Fig. 6, we show from top to bottom panels the following classes:

Power-law Decaying – ASASSN-14li and AT2019dsg are the only two sources to show prompt bright ($L_X \geq 10^{43}$ erg s $^{-1}$) X-ray emission during the optical peak.

Both sources show a power-law-like decay X-ray light curve, although the decay rate of the X-ray light curve in AT2019dsg is much higher than ASASSN-14li. Given the X-ray behavior, their L_{BB}/L_X do not show much variability staying in the $0.5 \leq L_{\text{BB}}/L_X \leq 10$ range during the entire evolution of the sources.

Late-time Brightening – Most sources in our sample show a $L_{\text{BB}}/L_X \gg 100$ near the optical peak, usually resulting from the faint X-ray emission ($L_X \leq 10^{42}$ erg s $^{-1}$) at early times. However, between 100-200 days after the optical peak, they show a significant brightening (more than an order of magnitude, $L_X \geq 10^{43}$ erg s $^{-1}$) in the X-rays, simultaneously to the UV/optical dimming and plateau, consequently L_{BB}/L_X tends to approach ~ 1 .

X-ray Faint – AT2018zr, AT2018hyz, and AT2019qiz also show $L_{\text{BB}}/L_X \gg 100$ near the optical peak, again resulting from the faint X-ray emission ($L_X \leq 10^{42}$ erg s $^{-1}$) at early times. However, the three sources never show a bright X-ray phase, although similar with previous classes their L_{BB}/L_X values also decrease with time.

Flaring – AT2019ehz show a unique behavior, the X-ray light curve show flares of almost two orders of magnitudes, from $L_X \sim \text{few} \times 10^{41}$ erg s $^{-1}$ up to $L_X \sim \text{few} \times 10^{43}$ erg s $^{-1}$ in a short scale of tens of days, while the L_{BB} show a standard smoothly evolution.

We could fit 12 of our 17 sources in these four classes; however, for the remaining sources, we do not have enough time coverage to assign them to one of these classes of X-ray evolution, either lack of sampling, lack of long-term follow-up, or lack of observations within the first 50 days from the optical peak. The later being fundamental to access whether the prompt bright X-ray emission is present or not.

4.2. X-ray spectral properties

The most distinct characteristic property of the X-ray spectra of TDE is its softness, clearly distinguishable from the dominant sources of extragalactic X-ray emission from AGN. While AGN usually emits from the soft X-ray up to the hard X-ray ($E \gg 10$ keV), with a non-thermal (power-law) spectrum, TDEs rarely show emission at energies higher than 2.0 keV.

To demonstrate this, we compare the X-ray spectral properties of our TDE sample with the X-ray properties of the non-blazar Type I and Type II of the BAT AGN Spectroscopic Survey (BASS, Ricci et al. 2017). Details on how the BASS comparison sample was retrieved is described in appendix §C.

In the left panels of Fig. 7 we compare the model independent – but instrument dependent – HR (as defined in §4) of the samples. Our entire TDEs sample

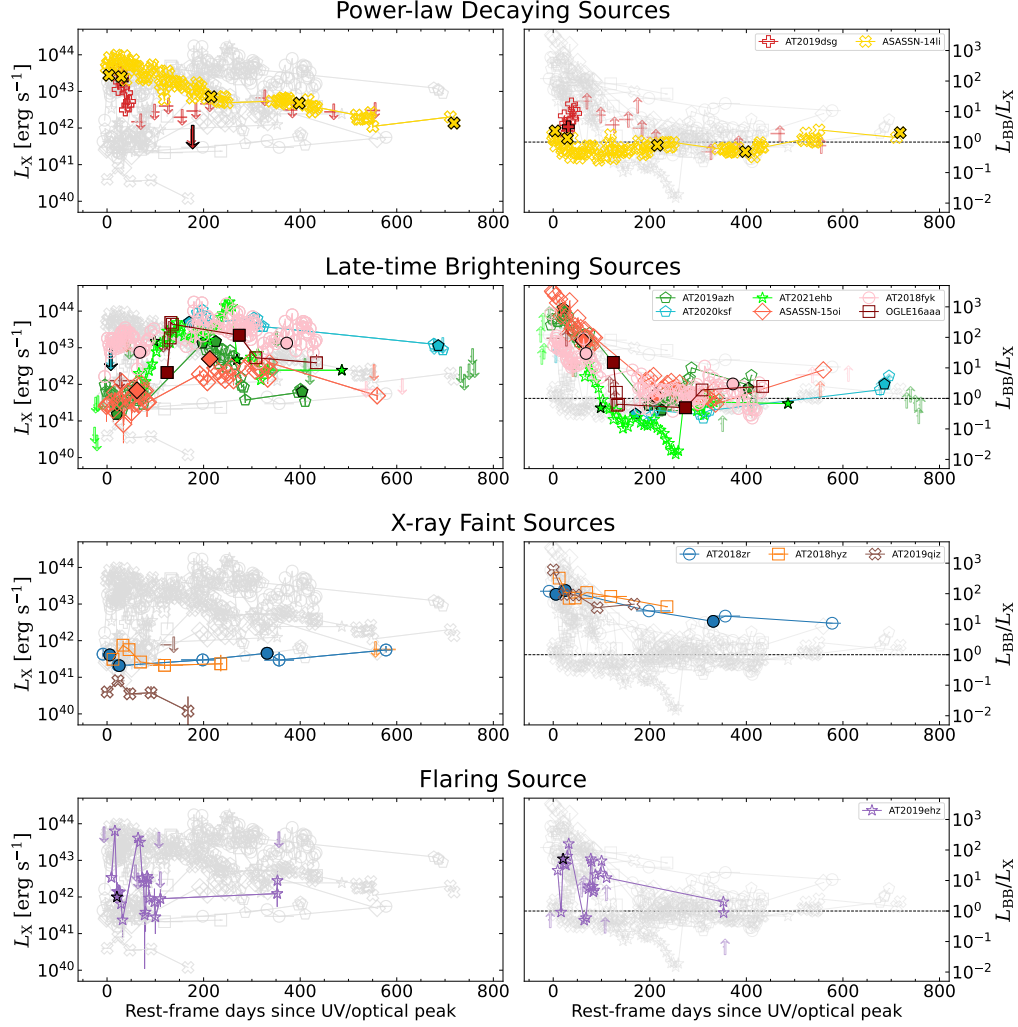


Figure 6. Left: The 0.3-10 X-ray luminosity (L_X). Right: ratio of UV/optical blackbody luminosity to X-ray luminosity (L_{BB}/L_X), grey dotted line shows $L_{BB} = L_X$. Top to Bottom panels show the different classes of X-ray evolution as described in §4.1.

has $HR \leq -0.6$, with 85% having $HR \leq -0.80$. The type I AGN sample concentrate between $-0.7 \leq HR \leq 0.0$, while the increased column density (N_H) in obscured type II AGN makes their HR to be concentrate between 0.0 and 1.0. Such HR is dependent on the X-ray instrument response, these values are valid for *Swift*/XRT and/or *XMM-Newton*, which have similar *relative* soft-to-hard sensibility.

Even at their harder states, TDEs are not as hard as AGN, that is due to two main reasons: i) the transient corona in TDEs rarely reaches the same power-law photon index of AGN (see more in §4.2.2); ii) most X-ray detected TDEs have negligible intrinsic N_H , while for AGN, even the unobscured (Type I) ones have detectable levels of neutral absorption, i.e., $21 \leq \log(N_H) \leq 22$, that absorbs some of the soft X-ray photons. The latter is a natural consequence of the gas-rich circumnuclear region of AGN and the gas/dust-poor cir-

cumnuclear region in the passive galaxies that host most TDEs (Jiang et al. 2021).

In the right panels of Fig. 7, we compare the photon index Γ (when TDE's spectra are fitted with `TBabs*zTBabs*zashift*powerlaw`). In AGN, both Type I and Type II, Γ only varies between ~ 1.0 and 2.5 , while in TDEs these are much steeper, with $\Gamma \in (2, 12)$. The large uncertainties in the spectra with $\Gamma \geq 4$ is not due to low S/N, instead by the inadequacy of the absorbed power-law to described TDE spectra, and the large degeneracy between the intrinsic N_H and Γ , when the a powerlaw model is fitted in a underlying thermal spectra, epochs/spectra with $\Gamma \leq 4$ are those in which corona formation is observed (see §4.2.2).

In summary, an absorbed powerlaw model is an inappropriate model for the emission of non-jetted TDEs, usually no physical interpretation can be derived from such fit, however, it still may be a good tool to differen-

tiate (when more information is lack) TDEs from AGN, as clearly demonstrate by Fig. 7.

4.2.1. Temperature and Radius Evolution

In this section, we explore the evolution of the temperature (T_p) and radius (R_p) derived from the X-ray continuum fitting (`tdediscspec`); we focus our analyses in the sources with higher temporal coverage in which some assessments on the long-term evolution of the derived parameters can be made. Due to the degeneracy between f_{sc} and T_p , at high values of f_{sc} , and the underline thermal can not be uniquely recovered (see §A), we exclude the sources with strong corona formation (i.e., $f_{sc} \geq 0.1$) from this analyses, these sources will be separately discussed in §4.2.2.

The temporal evolution of T_p is shown in Fig. 8; the cooling of the X-ray continuum is clearly observed: most sources show a peak X-ray temperature at their first available spectra, i.e., the closest to the peak of the UV/optical emission, with a decreasing T_p with time. This behavior is observed even for the sources with faint X-ray emission at early times.

In a Newtonian time evolving standard disk (Shakura & Sunyaev 1973; Cannizzo et al. 1990), the peak temperature follows a power law in time for a power-law declining accretion rate, $T_p \propto t^{(-n/4)}$, where n depends on the boundary conditions of the accretion disk: for finite stress at the innermost stable circular orbit (ISCO), $n \approx 0.8$, for a vanishing ISCO stress $n \approx 1.2$ (Mummery & Balbus 2020). These solutions seem to qualitatively agree with the observed behavior shown by the filled ($T_p \propto t^{(-1.2/4)}$) and dotted ($T_p \propto t^{(-0.8/4)}$) black lines in Fig. 8. The current quality/cadence of available data on X-ray TDEs does not allow for a more detailed assessment of the temperature evolution.

For a standard disk emission, T_p should also correlate with the bolometric luminosity, in the form $L_{disk,bol} \propto T^4$, while the relation with the observed X-ray luminosity should have a more general form of $L_X \propto T^\alpha$, where α is related to both the temperature evolution (i.e., n) and the measured temperature itself, given that the latter dictates the fraction of the bolometric luminosity emitted in the X-ray band.

In the top panel of Fig. 9, we show that such correlation is observed for several sources. However, some sources, namely AT2018zr, AT2019azh, ASASSN-15oi, and OGLE16aaa, show a decoupling between L_X and T_p . Such decoupling is a result of their maximum T_p occurring at early times (like all other sources), while their X-ray luminosity is at the faintest levels at early times ($L_X \leq 10^{42}$), which runs contrary to the expectation of higher luminosity at higher temperatures. All

these sources are either *Late-time brightening* or *X-ray faint* sources. The resulting decoupling, driven by the faint early-time X-ray emission, can also be seen by the color of the points in Fig. 9 representing their L_{BB}/L_X values: all sources that show $L_X \propto T^\alpha$ (top panel) have $L_{BB}/L_X < 10$ in all epochs, sources with decoupling between L_X and T_p have epochs with $L_{BB}/L_X \gg 10$, and it is in those specific epochs that the decoupling is observed. These results points towards a suppression of the X-ray flux/luminosity in this sources/epochs, while the observed T_p seems be following its expected behavior. An X-ray spectrum of AT2020ksf (another *Late-time brightening* source) at its early-time X-ray faint phase is not available to confirm whether such decoupling from the expected relationship is also present.

A similar analysis can be done regarding the apparent radius of the peak disk temperature (R_p); for a standard disk (with no ionizing/neutral absorption or/and reprocessing), the temperature should peak at the ISCO, i.e., $R_p = R_{ISCO} = (1 - 6) \times R_g$ (depending on the MBH spin), where $R_g = GM_{BH}/c^2$ is the gravitational radius. Given that the (systematic plus statistical) uncertainties in M_{BH} derived from scaling relations (see §3.4) are in the order of 0.5 dex, any measured radius in the $0.3 \leq R_p/R_g \leq 20$ range is still statically consistent with being emitted at the R_{ISCO} .

From Fig. 11, it is clear that for most sources/epochs, the recovered R_p are within the physically valid interval (i.e., $0.3 \leq R_p/R_g \leq 20$) hence are consistent with R_{ISCO} , in agreement with Mummery et al. (2023) findings. However, some epochs/sources show unphysically low values, i.e., $R_p/R_g \ll 0.3$, interestingly these sources show a large apparent R_p evolution, from unphysical values at early times to valid reasonable values at late times; a consequence of this is that the R_p/R_g seems closely connected with L_{BB}/L_X (and hence the distinct light curve evolution classes): the epochs with $R_p/R_g \ll 0.3$ are the epochs with higher L_{BB}/L_X (this can also be seen in Fig. 15). This correlation is not only observed for the general sample but also in distinct epochs of the same source (see, e.g., AT2019azh, OGLE16aa, AT2018zr in Fig. 11).

The L_{BB}/L_X (hence the shape of the SED) for a standard accretion disk also has a limiting range of values; based on our simulation shown in §B, for T_p range measured in our sample (i.e., $5.5 \leq \log T_p \leq 6.1$ K), the ratio between the observe L_{BB} and L_X , can only be $5 \times 10^{-2} \leq L_{BB}/L_X \leq 70$. Combing the valid ranges for L_{BB}/L_X and for R_p/R_g , in Fig. 11 we show in a gray shaded region the space of parameters in which derived properties *could*, in principle, be explained by a *bare/unreprocessed* accretion disk. For observations that fall outside this

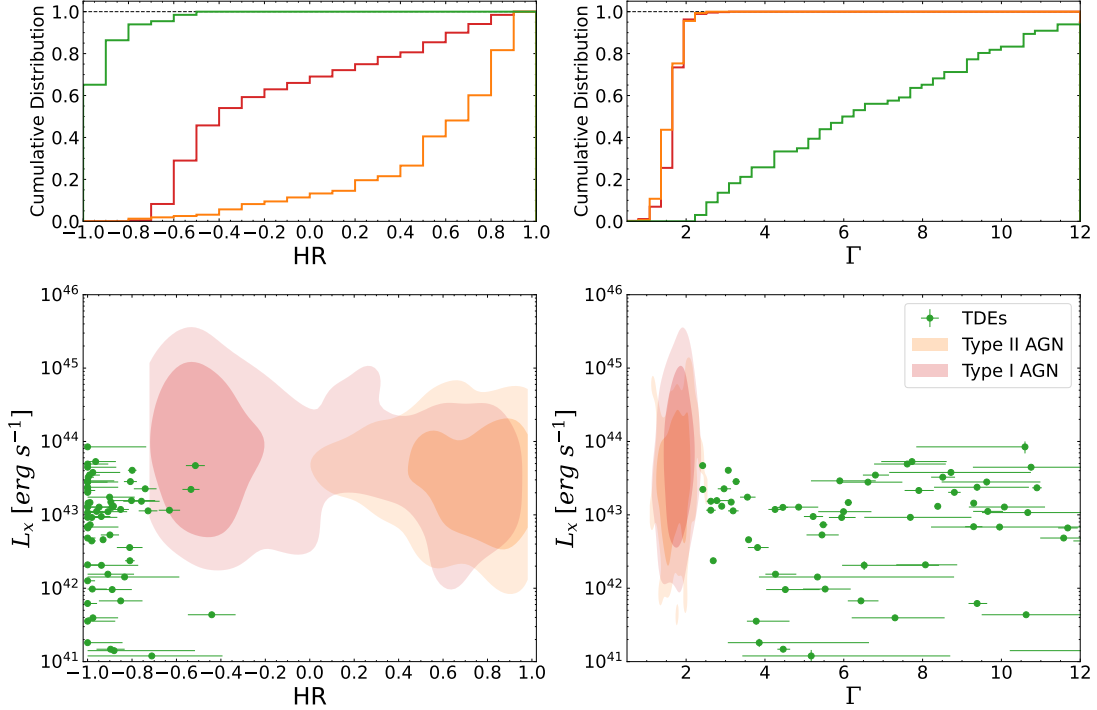


Figure 7. Comparison between X-ray spectral properties of TDEs (green) and AGN (Type I in red and Type II in gold) from the BAT AGN Spectroscopic Survey (BASS, Ricci et al. 2017). In the left panels we compare the *Swift*/XRT or *XMM-Newton* hardness ratio (HR, see text for definition), in the right panels we compare the Γ power-law index when TDEs are fitted with an absorbed power-law model. The top panels show the cumulative distribution of the parameters, while the bottom panels show the distribution of samples in the L_X vs. HR and L_X vs. Γ parameter space. For AGNs the contours represent 68% and 90% of the sample distribution, for TDEs each point is a *XMM-Newton* or *Swift*/XRT stacked spectrum.

region, however, the derived parameters are inconsistent with the ones of a *bare/unreprocessed* disk; hence additional radiative processes must be present. Interestingly, the epochs/sources in which the measured L_{BB}/L_X and R_p/R_g fall outside the disk region are the same epochs/sources that are decoupled from the $L_X \propto T^\alpha$ relation. i.e., all sources showing faint X-ray emission at early times.

In the following paragraphs we aim to demonstrate that the apparent unphysical R_p/R_g values derived from *X-ray faint* sources and the early-time observations of *Late-time brightening* are evidence for the suppression of the emitted X-ray in these sources/epochs and can be explained by the way that R_p is ‘measured’ by the X-ray continuum fitting.

In the color-corrected quasi-Wien approximation of `tdediscspec`⁸, the X-ray spectrum ($F_X(\nu)$) is related to R_p and T_p as follows:

$$F_X(\nu) \propto \left(\frac{R_p}{D}\right)^2 \tilde{T}_p^\gamma \exp\left(-\frac{h\nu}{k\tilde{T}_p}\right) \quad (3)$$

⁸ The specific equations are for `tdediscspec` but the same arguments holds for any thermal model.

where $\tilde{T}_p = f_{\text{col}} f_\gamma T_p$ (see definitions in §3.3.1), and D is the source luminosity distance. This means that the shape of the X-ray spectra shape depends exclusively on T_p , but not on R_p which is only a ‘*physically scaled*’ normalization factor that translates the observed count rate per energy bin to a flux per energy bin. Similarly,

$$L_X \propto R_p^2 \tilde{T}_p^\gamma \int_{\nu_i}^{\nu_f} \exp\left(-\frac{h\nu}{k\tilde{T}_p}\right) d\nu \quad (4)$$

where $\nu_i = \frac{0.3 \text{ keV}}{h}$ and $\nu_f = \frac{10 \text{ keV}}{h}$. Therefore for a constant T_p , $L_X \propto R_p^2$, while L_X decreases with decreasing T_p for constant R_p .

As we have shown, all sources – including those with faint X-ray emission at early times – show a decreasing or constant T_p with time; this means that their faint X-ray emission and late time X-ray brightening (or constant L_X , in AT2018zr) will translate into to an extremely low R_p at early times and an order of magnitude increase in R_p at late times. Such behavior is a consequence of eq. 4 in which R_p can not be constant with time if T_p is decreasing (or held constant) and L_X is not decreasing – as is the case for all sources in the bottom panel of Fig. 9.

One can take the earliest ($\Delta t = 21$ days) spectrum of AT2019azh as an example: the measured temperature and apparent radius were $\log T_p \approx 5.75$ K and $R_p/R_g \approx 6 \times 10^{-2}$, while $L_X \approx 2 \times 10^{41}$ erg s $^{-1}$. In order for the R_p/R_g to be within the physically valid range (i.e., to be at least 0.3), based on eq. 4, the observed luminosity would have to be higher by a factor of $(\frac{0.3}{0.06})^2 \approx 25$, similarly, for the early time R_p/R_g to be at the same value as the late-time $R_p/R_g \approx 3$ (hence a physically valid and approximately constant value during its entire evolution) the observed early time L_X would have to be higher by a factor of $(\frac{3}{0.06})^2 \approx 2 \times 10^3$. Such an increase would make the early time L_X to be coupled to the T_p during the entire evolution of the source, as can be seen by the bottom panel of Fig. 9.

A similar analysis can be done for the early time spectra of all the *Late-time Brightening* and *X-ray faint* sources, that show this unphysical value/evolution of the apparent R_p , for all of them an increase in the L_X by a factor $\gg 10$ is necessary for a physical value of R_p/R_g , given their measured temperature evolution.

In summary, the unphysical values of R_p/R_g , accompanied by decoupling between L_X and T_p , and a SED shape (L_{BB}/L_X) inconsistent with an accretion disk, indicates suppression of the emitted X-rays in these epochs/sources. However, such suppression of the X-ray emission seems to have a small effect in the measured T_p – given that the cooling of the accretion disk is still observed and is independent of the observed flux level – while suppression of the total observed X-ray flux is high. We will discuss possible mechanisms responsible for such suppression in §5.1. In Mummery et al. (2023), when the authors average all R_p values obtained in each spectrum to find a $\langle R_p \rangle$ for each source, the information on the unphysical nature of the R_p/R_g obtained at early times was missed. Furthermore important data such as high S/N X-ray spectra of, for example, AT2019azh at early times and AT2018zr at late times, as well as a $M_{BH}-\sigma_*$ measurement of AT2018zr’s black hole mass were not available to the authors, but are presented here. Although, we agree on the authors main claim, i.e. R_p is tracing R_{ISCO} , we show that this is only valid in the cases where the X-rays are not suppressed and the SED is consistent with a *bare/unreprocessed* disk, which is usually not the case for the very early times of optically discovered TDEs (as we will discuss in §4.3).

4.2.2. Soft \rightarrow hard transition

The X-ray spectra of AT2018fyk, AT2020ocn, and AT2021ehb exhibit extreme softness at early times ($\Delta t \leq 100$ days), similar to other spectra in our sample. However, these three sources undergo a transition to a

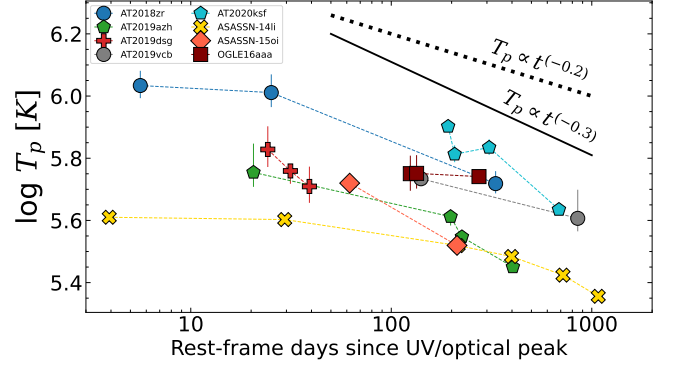


Figure 8. Peak temperature (T_p) of the accretion disk model as function of days since the UV/optical peak. Only sources with at least two fittable spectra and with no corona emission (see §4.2.2) are shown. The solid black line show the expected theoretical evolution for a finite stress at the innermost stable circular orbit.

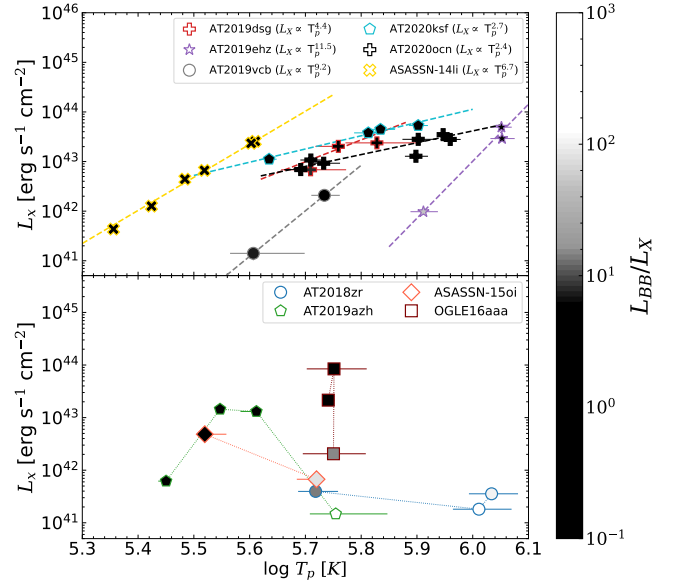


Figure 9. X-ray luminosity (L_X) as a function of peak temperature (T_p). The upper panel show sources where a $L_X \propto T_p^\alpha$ relation is observed, with the best-fitted α for each source shown in the legend. The bottom panel show the source where a clear decoupling between L_X and T_p is present. The color in which the markers are filled maps the L_{BB}/L_X ratio between the UV/optical luminosity and the L_X following the color-bar in the right side of the figure.

hard power-law-like state with a timescale of ~ 200 days after the UV/optical peak. The power-law component dominates the disk emission in this state and extends to much higher energies than in the soft state. As an extreme example, the *NuSTAR* spectra of AT2021ehb presented by Yao et al. (2022) show power-law emission detected above background up to 30 keV.

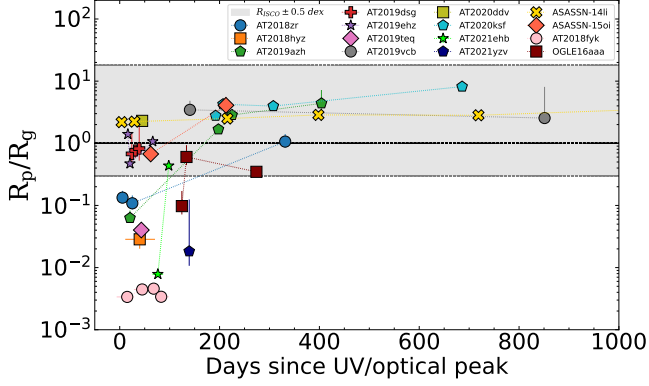


Figure 10. Apparent radius (R_p) of the peak temperature normalized by the gravitational radius (R_g) as function of days since the UV/optical peak. Only sources with no corona emission (see §4.2.2) are shown. Gray shaded region shown the $0.3 \leq R_p/R_g \leq 20$ interval in which the measured R_p/R_g is statistically consistent with R_{ISCO} .

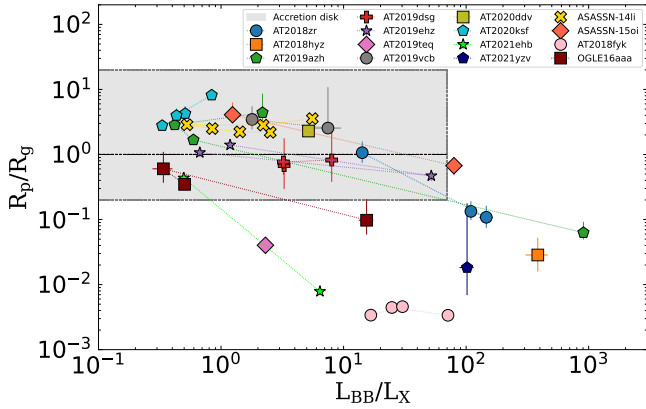


Figure 11. Distribution of apparent disk radius (R_p) normalized by the gravitational radii (R_g), and the L_{BB}/L_X ratio between the UV/optical luminosity and the X-ray luminosity. The shaded gray region delimits the parameter space in which the emission can be explained by a *bare/unreprocessed* standard accretion disk, see text for details. Several sources/epochs fall outside this region having unphysically low R_p/R_g values while also having SED shapes (L_{BB}/L_X) that deviate from the allowing SED shape of disk, and require additional radiative processes.

In the case of AT2018fyk, a faint hard excess ($f_{sc} \leq 0.05$) starts to appear around $\Delta t \approx 50$ days. Between $50 \leq \Delta t \leq 200$ days, a strong coronal component rapidly forms. The *Swift*/XRT spectrum at $\Delta t = 209^{+34}_{-35}$ days already shows $f_{sc} \approx 0.2$, and the peak of the corona emission occurs at $\Delta t = 209^{+45}_{-30}$ days with $f_{sc} \approx 0.3$. At this stage, the power-law component dominates the X-ray flux over the thermal component. The fraction of up-scattered photons decreases to $f_{sc} \approx 0.15$ at $\Delta t \approx 350$ days and remains relatively constant until the source becomes undetectable in the X-rays at $\Delta t = 500$ days.

In the case of AT2021ehb, a hard excess ($f_{sc} \approx 0.02 - 0.05$) is present from the first X-ray detections at $\Delta t \approx 70 - 100$ days. The value of f_{sc} then slowly rises to ~ 0.15 at $\Delta t \approx 200$ days, followed by an extreme transition to a corona-dominated state ($f_{sc} \approx 0.5$) at $\Delta t \approx 250$ days. At this stage, the spectra are hardly distinguishable from typical AGN X-ray spectra. The source then slowly transitions to an intermediate state again at $\Delta t \approx 300$ days.

For AT2020ocn, the state transition is even more extreme. The source is completely soft and disk-dominated (i.e., no need for the addition of the *simPL* model, or $f_{sc} = 0.00$) up to $\Delta t \approx 200$ days. However, a spectrum taken after a seasonal gap at $\Delta t \approx 290$ days shows the corona completely dominating the X-ray emission ($f_{sc} \approx 0.5$). The source remains in this hard state for at least 100 days and is observed again to be in an intermediate state at $\Delta t \approx 700$ days. Figure 12 displays the softest early-time spectrum (left panels), the hardest spectrum (middle panels), and the intermediate state at very late times (right panels), for the three sources, showing the formation of the corona.

Transitions from a soft disk-dominated state to a hard corona-dominated state are commonly observed in stellar-mass black holes in X-ray binary systems. They follow a standard *q-shape* evolution in the hardness-intensity diagram (HID, e.g., Remillard & McClintock 2006; Wang et al. 2022). However, in the case of MBHs, the corona is a ubiquitous and dominant component of the X-ray spectra of AGN. Dramatic state transitions, such as the appearance or disappearance of X-ray power-law emission, are usually not observed in AGN, except in the case of the Changing-look AGN 1ES 1927+654 (Trakhtenbrot et al. 2019; Ricci et al. 2020), where the corona was destroyed and later reformed. Therefore, X-ray bright TDEs provide a new window for studying the emission and formation of this poorly understood component.

A study by Wevers et al. (2021) suggested that AT2018fyk exhibits a “Fainter harder brighter softer” behavior similar to X-ray binary outbursts. Additionally, Wevers (2020) argued that this behavior could be ubiquitous in X-ray bright TDEs. The HID analysis conducted by Wevers et al. (2021) involved using the α_{OX} parameter, defined as the logarithmic ratio between the UV flux (representing the disk emission) and the 2 keV flux (representing the corona emission), along with the bolometric luminosity (L_{Bol}) normalized by the Eddington luminosity (L_{Edd}).

The left panel of Fig. 13 displays the HID for the three sources showing corona formation. In this figure, we utilize $\frac{f_{sc}}{\max(f_{sc})}$ as a measure of hardness, representing the

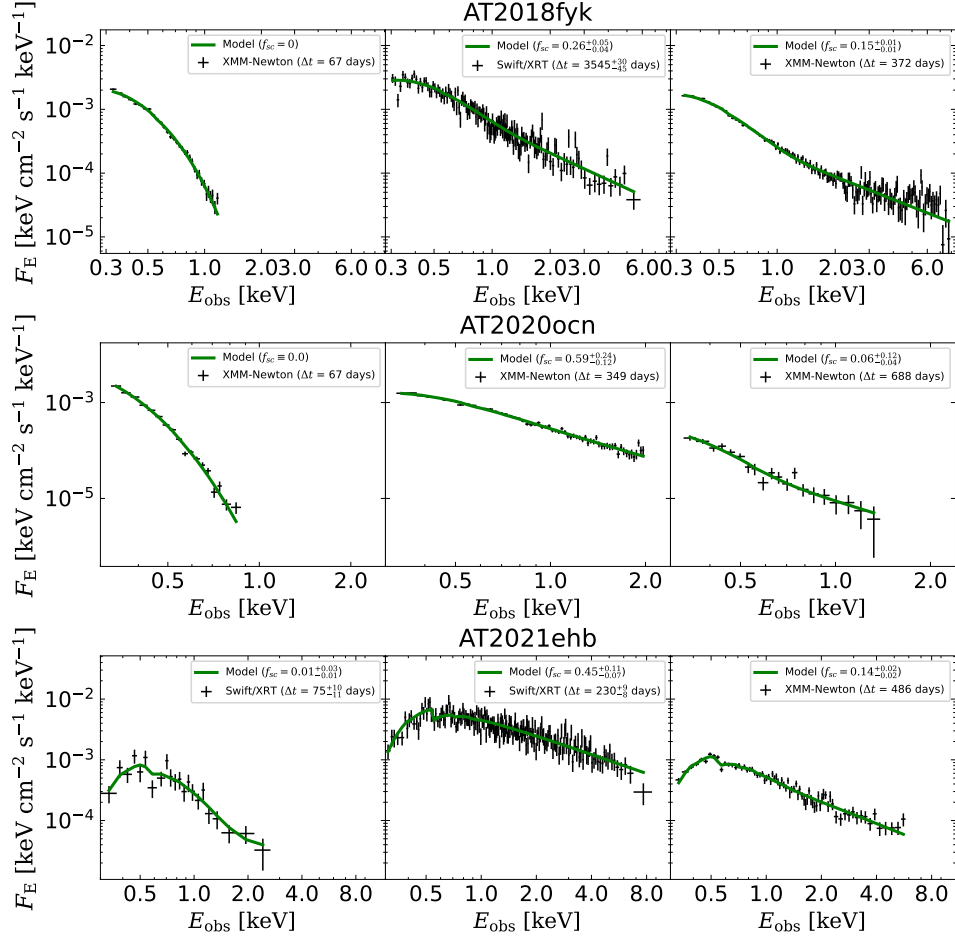


Figure 12. Spectral evolution of the three sources that show soft \rightarrow hard state transition, i.e., corona formation. From top to bottom: AT2018fyk, AT2020ocn, and AT2021ehb. From left to right: early time soft state spectra, hardest state spectra, and late-time intermediate state spectra. Unfolded spectra are shown in black crosses, best fitted model are shown in green.

relative strength of the corona, and $\frac{L_{BB}+L_X}{L_{Edd}}$ as a measure of intensity. A significant portion of the bolometric luminosity should be emitted in the unobserved extreme UV (EUV) range, the shape of the spectral energy distribution (SED) between the UV and X-ray regions is not fully understood and highly dependent on models, especially when the total SED deviates from a standard accretion disk SED (e.g., when $L_{BB}/L_X \gg 10$, see §4.3 for a detailed discussion on SED properties), therefore, we use $L_{BB} + L_X$ as a proxy for L_{Bol} and $\frac{L_{BB}+L_X}{L_{Edd}}$ as a proxy for the Eddington ratio. The actual value of L_{Bol} would be much higher if the EUV emission were taken into account.

From the left panel of Fig. 13, it can be observed that all three sources start in a soft state and then quickly transition to a hard state. This transition is accompanied by an increase or plateau in luminosity, primarily due to the addition of corona emission ($E > 1.0$ keV) to L_X (measured from 0.3-10 keV). The transition occurs at $\frac{L_{BB}+L_X}{L_{Edd}}$ values between 5×10^{-3} and 5×10^{-2}

for the three sources. However, as time passes and the luminosity decreases, all sources undergo further transitions, either returning to a completely soft state or transitioning to an intermediate state ($0.05 \leq f_{sc} \leq 0.15$); this behavior contrasts with the *Fainter harder brighter softer* pattern.

In the right panel of Fig. 13, we compare the power-law index (Γ_{sc}) of the emerging corona in the three TDE showing a state transition ($f_{sc} \geq 0.1$) to the corona power-law index (Γ) measured from the population of unobscured ($N_H \leq 10^{22}$ cm 2) AGN in the BAT AGN Spectroscopic Survey (BASS, Ricci et al. 2017). In the AGN population, Γ exhibits values in a narrow range between 1.2 to 2.5 with a mean value of $\Gamma \approx 1.7$, TDEs however, even at their hardest state are rarely as hard as AGN, instead their Γ_{sc} can exhibit a broader range of values between 1.7 and 4.0. The Γ_{sc} distribution and the evolution in the HID diagram suggest that the high optical depth corona cannot be sustained for an extended

period as the accretion rate onto the MBH decreases; we will discuss further implications in §5.6.

4.3. SED evolution

A natural consequence of the diversity of X-ray light curves and the uniformity of the UV/optical light curves is that the spectral energy distribution (SED) shows very distinct shapes and evolution. The shape of the broad-band SED can be probed by the $L_{\text{BB}}/L_{\text{X}}$ ratio. As shown in the bottom panel of Fig. 4; these ratios can vary between $\text{few} \times 10^3$ and $\text{few} \times 10^{-2}$. In Fig. 14, we show the cumulative distribution of $L_{\text{BB}}/L_{\text{X}}$ at three time bins, early times ($\Delta t \leq 50$ days) in purple, and at late times ($150 \leq \Delta t \leq 250$ days) in orange, and very late times ($400 \leq \Delta t \leq 800$ days) in black. The SED also show a noticeable trend: at early times they have $L_{\text{BB}}/L_{\text{X}}$ as large as 3000 and as low as 0.5, but with most sources showing $L_{\text{BB}}/L_{\text{X}} \geq 10$; with increase time from optical peak this range of $L_{\text{BB}}/L_{\text{X}}$ shrinks, and at very late times all sources show $0.5 \leq L_{\text{BB}}/L_{\text{X}} \leq 10$.

As discussed in §4.2.1 and demonstrated in Appendix §B, the SED produced by a *bare/unreprocessed* standard accretion disk with T_p in the range of values find in TDEs (i.e., $5.5 \leq \log T_p \leq 6.1$ K) can only produce $5 \times 10^{-2} \leq L_{\text{BB}}/L_{\text{X}} \leq 70$. Therefore the values of $L_{\text{BB}}/L_{\text{X}}$ in the range 100-1000 found in the early times of a large fraction of our sources indicate that an additional emission mechanism that deviates from a standard accretion disk-corona is operating. The deviation from a standard disk is stronger at early phases, given that the $L_{\text{BB}}/L_{\text{X}}$ ratios converge towards the expected disk values at late times.

In Fig. 15, we explore whether a standard disk SED can explain the observed SED for three distinct TDEs, one *Power-law Decaying*, one *Late-time brightening* and one *X-ray faint*. We extrapolate from the best-fitted parameters of the X-ray fitting disk model to the UV/optical bands. The shaded gray region represents our ignorance on the disk structure, and is a result of the uncertainty in the peak temperature and normalization (radius), as well as in the temperature profile, where we assume the limiting solutions: $T(R) \propto R^{-3/4}$ for a standard vanishing ISCO stress (Shakura & Sunyaev 1973; Cannizzo et al. 1990) and $T(R) \propto R^{-7/8}$ for a finite ISCO stress (Agol & Krolik 2000).

From the top panel, we can see that the SED of ASASSN-14li is consistent with an accretion disk even at early times; very little to no UV/optical excess is present; furthermore, the evolution in SED shape with time is very small and compatible with the cooling of the accretion disk. The same holds for the other *Power-law decaying* source, AT2019dsg, although the rapid decay

of X-ray emission indicates a quicker cooling of the accretion disk (Cannizzaro et al. 2021).

For AT2019azh, however, the disk emission extrapolated from the X-rays under-predicts the UV/optical emission by more than two orders of magnitudes, as can be seen from the left middle panel of the Fig. 15. This is mainly a consequence of the low X-ray luminosity $L_{\text{X}} \approx 5 \times 10^{41}$ erg s $^{-1}$ and high T_p , that result in both an unphysical R_p/R_g and a high $L_{\text{BB}}/L_{\text{X}} \approx 890$. At later times however, L_{BB} decays and L_{X} brights ($L_{\text{BB}}/L_{\text{X}} \approx 1$), and the SED is consistent with a standard accretion disk. Such behavior is observed in all *Late-time brightening* sources. One should notice that in AT2021ehb, the $L_{\text{BB}}/L_{\text{X}}$ reaches extremely low value $\sim 10^{-2}$ given the strong corona formation that increases L_{X} , consequently decreasing $L_{\text{BB}}/L_{\text{X}}$.

In the case of AT2018zr, the early time is very similar to AT2019azh; however, even at $\Delta t \approx 331$ days, the SED is yet not consistent with a standard disk, although the UV/optical excess does decrease, while L_{X} is approximately constant during the entire evolution. Similar behavior is found in the other *X-ray faint sources*. The physical interpretation of the diversity of SED shapes at early times and the convergence to a disk-like SED at late times, will be discussed and compared with the theoretical expectations in §5.1.

As discussed in §4.2.1, there is a clear anti-correlation between $L_{\text{BB}}/L_{\text{X}}$ and the radius derived from the X-ray spectral fitting, R_p/R_g assumes nonphysical values at the highest $L_{\text{BB}}/L_{\text{X}}$ (usually with $L_{\text{BB}}/L_{\text{X}} \gg 10$), this can also be seen in the legend of Fig. 15. In light of the discussion of this current section and §4.2.1, we can conclude that R_p/R_g values are nonphysical when the SED strongly deviates from the SED of a standard disk. Both lines of evidence point towards the suppression of the observed X-ray emission as discussed in §4.2.1.

4.4. The ratio of X-ray loud TDEs in optical surveys and its (in)dependence on M_{BH}

A surprising characteristic of the population of TDEs discovered by optical surveys is the lack of detectable X-ray emission in most sources, contrary to that first theoretical expectation (Rees 1988) and the fact that first TDE were discovered in the X-rays (e.g., Bade et al. 1996). We would like to determine the fraction ($N_{\text{opt,x}}/N_{\text{opt}}$) of optically discovered TDEs that show X-ray emission. Therefore, a controlled sample of total discovered TDE and X-ray bright TDEs needs to be compared.

We will use the first 3 years of the ZTF (October 2018 to August 2020 for ZTF-I and September 2020 to August 2021 for ZTF-II) survey to determine this ratio. After a

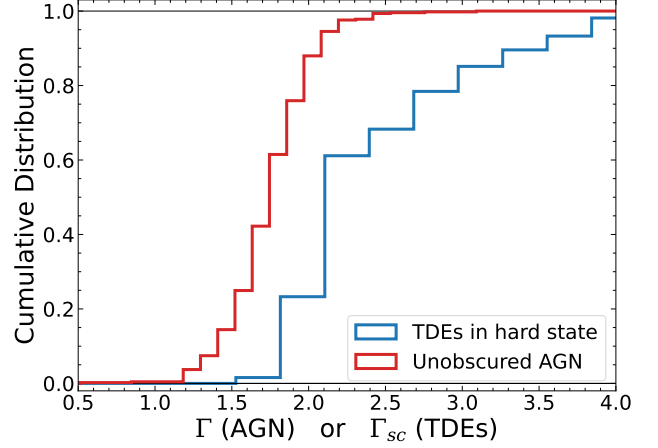
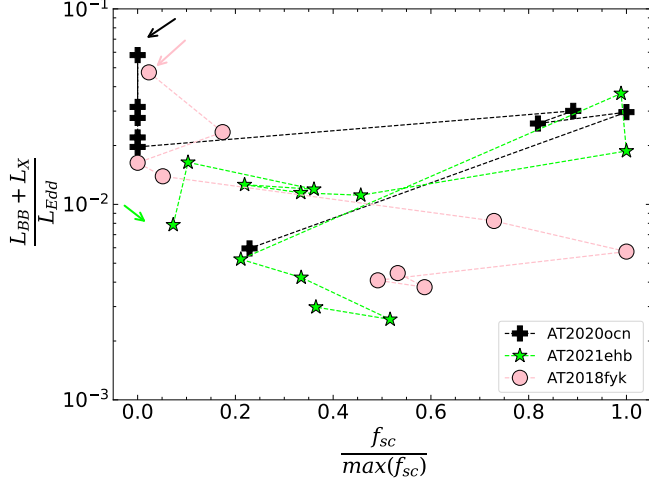


Figure 13. Properties and evolution of the corona emission in TDEs. Left: Hardness intensity diagram (HID), the total observed luminosity ($L_{BB} + L_X$) in units of the Eddington luminosity, as a function of the hardness as traced by the normalized fraction (f_{sc}) of the photons upper-scatter by the corona. The arrows indicate the first available spectra for each source, and the points are connected by increasing Δt . Right: comparison between the power-law index of the corona emission spectra in local AGN (Γ , blue) from the BAT AGN Spectroscopic Survey (BASS), and TDEs (Γ_{sc} , red) that show corona formation (AT2020ocn, AT2021ehb, AT2018fyk).

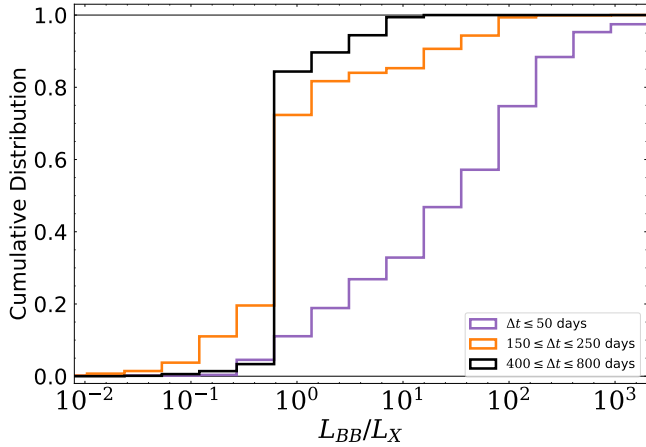


Figure 14. Evolution of the distribution of SED shapes, as trace by the ratio (L_{BB}/L_X) between the UV/optical luminosity (L_{BB}) and the 0.3-10 keV luminosity (L_X). Each color show the distribution in a different time bin. The contribution of each source for the total distribution was weighed by the number of spectral observation available in each Δt interval.

ZTF TDE candidate (see, [van Velzen et al. 2021](#); [Yao et al. 2023](#), for selection criteria) is spectrally classified, a few *Swift* observations are performed to confirm the UV brightness characteristic of TDEs and check whether the source is detected in the X-rays. The number of visits and the cadence varies from source to source, but at a minimal a few 1-2 ks long observations (usually with a total of ~ 10 ks) are performed, leading to a detection limit of $\sim 5 \times 10^{-14}$ erg cm $^{-2}$ s $^{-1}$ with XRT, which means any TDE with $L_X > 10^{42}$ erg s $^{-1}$ can be detected

up to $z \approx 0.09$, while $L_X \sim 10^{41}$ erg s $^{-1}$ can only be detected if extremely nearby ($z < 0.04$). Therefore, we will use $L_X \geq 10^{42}$ erg s $^{-1}$ to define the sub sample X-ray bright TDEs. During the first three years of ZTF 10 sources showed, at some point in time, $L_X \geq 10^{42}$ erg s $^{-1}$, therefore $N_{opt,x} = 10$.

To construct the control sample, we start with all TDEs discovered by ZTF during the same time period (from [van Velzen et al. 2021](#); [Hammerstein et al. 2023a](#); [Yao et al. 2023](#)). For sources at $z < 0.09$ (24 sources), we select those with *Swift*/XRT observations, for sources with no XRT detection we stacked all their *Swift*/XRT observations and check whether L_X upper-limit (after correcting for Galactic absorption) was deeper than 10^{42} erg s $^{-1}$. Only 3 sources (AT2021mhg, AT2021sdu, AT2021yte) the upper limit were not deep enough to constraint the presence $L_X \geq 10^{42}$ erg s $^{-1}$, particularly because of their higher Galactic absorption $N_{H,G} \geq 10^{21}$ cm $^{-2}$, than the typical $N_{H,G} \approx \text{few} \times 10^{20}$ cm $^{-2}$ of the other sources. For our typical exposure times, *XMM-Newton* detection limit is around 5×10^{-15} erg cm $^{-2}$ s $^{-1}$, this means that we can detected $L_X > 10^{42}$ erg s $^{-1}$ up to $z \approx 0.25$. Therefore, we include all sources at $0.09 \leq z \leq 0.25$ that had at least one *XMM-Newton* visit to our control sample (adding 4 more sources). This results in 25 sources in which a $L_X \geq 10^{42}$ erg s $^{-1}$ could be (or was) detected if such level of emission was present, hence $N_{opt} = 25$. Therefore for ZTF, we obtain $N_{opt,x}/N_{opt} = 10/25$, meaning that in ZTF, $\sim 40\%$ of the discovered TDEs had (eventually) some X-ray bright emission ($L_X \geq 10^{42}$ erg s $^{-1}$). The list of

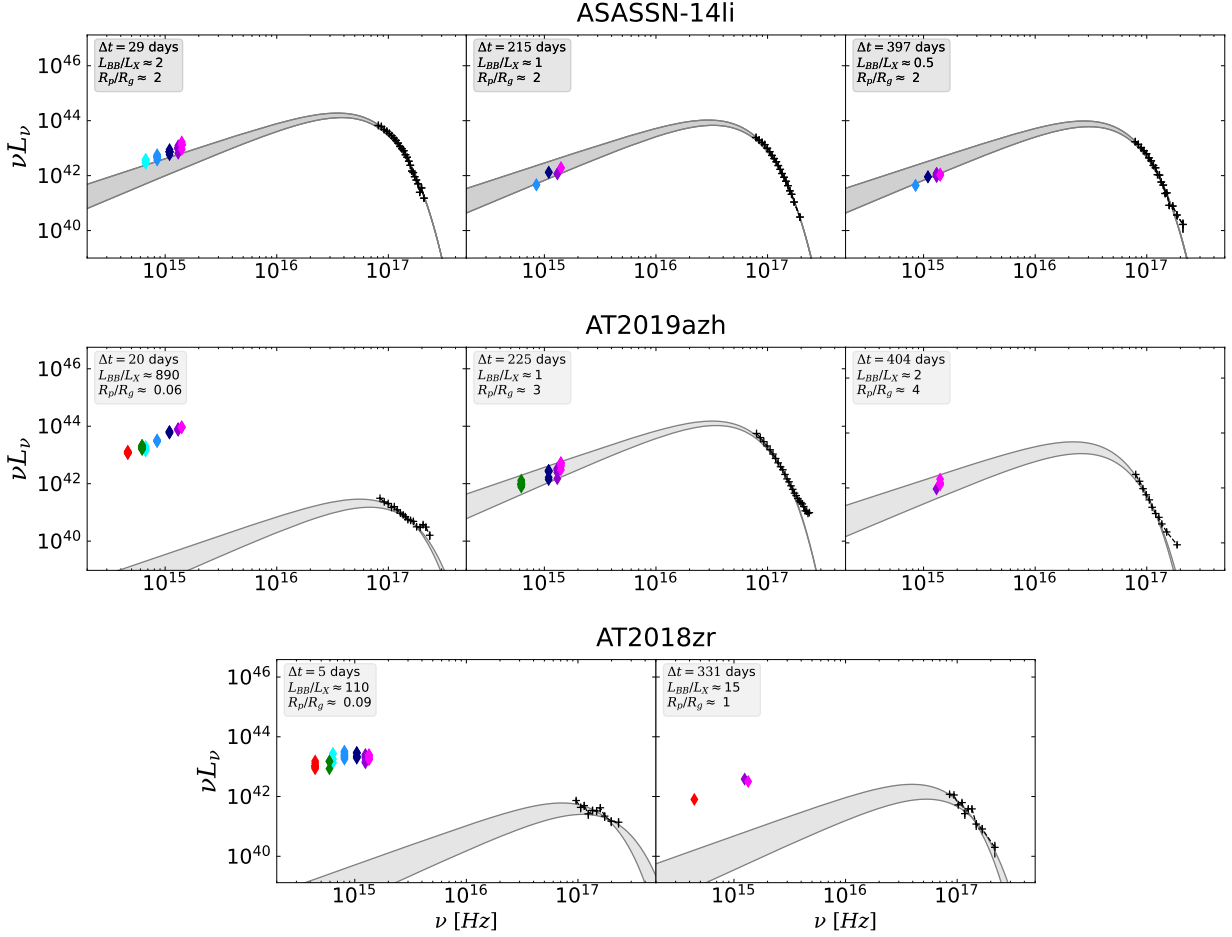


Figure 15. Evolution of the SED for three sources, one *Power-law decaying* (Top), one *Late-time Brightening* (middle), and one *X-ray faint* (bottom). Left panels show early time ($\Delta t \leq 30$ days) SED, middle panel show late time SED ($\Delta t \approx 200$ days) and right panel show very-late time SED ($\Delta t \approx 400$ days). No X-ray spectrum of AT2018zr around $\Delta t \approx 200$ days is available. The colored points show the observed UV/optical photometry (ZTF + *Swift*/UVOT), the black crosses show the unfolded X-ray spectrum, the gray line shows the best-fitted disk model (and uncertainty) for the X-ray spectra, and it is extrapolated to the UV/optical band to check whether the full SED is consistent with a disk or not. Main parameters of interest are shown in the legend for each epoch.

the 25 TDEs and their redshift are present in Table 4. Given the non-uniformity of the X-ray follow-up, particularly at late-time for those at higher z , the ratio should be seen as an lower-limit.

We also use this above-defined sub samples to investigate whether the presence of $L_X \geq 10^{42}$ is dependent on M_{BH} . In Fig. 16 we show the cumulative distribution of M_{BH} for the two sub samples (L_X higher and lower than 10^{42} erg s $^{-1}$), where the underlying distribution was constructed by adding a normalized probability distribution function (PDF) based on estimated M_{BH} and their uncertainties (see §3.4).

From Fig. 16 there seems to be no distinction between the M_{BH} distribution of TDE L_X higher/lower than 10^{42} erg s $^{-1}$: the difference in the median of the distributions (dotted vertical lines) is only ~ 0.1 dex which is much smaller than the typical uncertainty in M_{BH} . In order

to statistically investigate the (lack of) difference between the distributions we apply a Kolmogorov-Smirnov test, assuming the null-hypothesis that the two samples are drawn from the same distribution, we recover a p -value of ~ 0.2 , which means the null-hypothesis can not be excluded, hence there is no statistically significant difference between the distributions. This result is in agreement with previous ones, that although use distinct samples or selection criteria, also did not find any correlation between X-ray loudness and M_{BH} (Wevers et al. 2019b; French et al. 2020; Hammerstein et al. 2023a,b),

4.5. X-ray luminosity function

When studying sources with constant flux, such as quasars, we can estimate their luminosity function (LF) by assigning weights to each source proportional to its

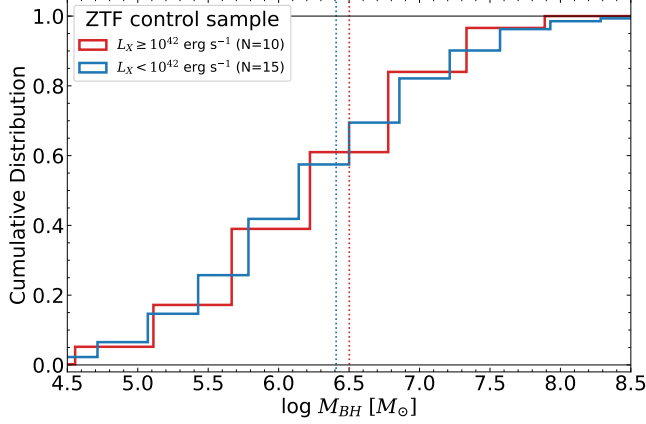


Figure 16. Cumulative distribution of black hole mass for the *ZTF control sample* (see §4.4 for definition) with L_X higher or lower than 10^{42} erg s $^{-1}$. The underlying distribution was constructed by adding the normalized PDF of individual sources M_{BH} based on the estimated values and its uncertainties. No statistically significant difference in the distributions is observed.

maximum detectable volume, V_{max} . This approach, introduced by [Schmidt \(1968\)](#), allows us to obtain a representative sample of the population and plot the number of sources per unit volume as a function of their luminosity.

In the case of transients, such as supernovae (SNe) and TDEs, we are interested in their volumetric rate, i.e., the number of events per unit volume per unit time as a function of their peak luminosity. To estimate this rate from a survey, we can also use the “ $1/V_{\text{max}}$ ” method, but with a modification that accounts for the survey duration and area. We define this modified V_{max} as:

$$V_{\text{max}} = V(z_{\text{max}}) A_{\text{survey}} \times \tau_{\text{survey}} \quad (5)$$

where $A_{\text{survey}} \times \tau_{\text{survey}}$ denotes the product of the effective survey duration and survey area, and $V(z_{\text{max}})$ is the volume (per unit solid angle) corresponding to the maximum redshift observable with the survey, given its limiting flux.

Single-band optical and integrated UV/optical luminosity function for TDEs was first present by [van Velzen \(2018\)](#), who constructed a *relative* luminosity function using 13 TDE discovered before 2018 by several surveys (namely GALEX, SDSS, PTF, iPTF, PS1, and ASASSN). More recently, [Yao et al. \(2023\)](#) present an *absolute* UV/optical luminosity function from a sample of 33 homogeneously selected TDEs from ZTF. In the X-rays, the first luminosity function was constructed from 13 events selected among X-ray transients detected in the $0^\circ < l < 180^\circ$ hemisphere by *SRG/eROSITA* during its second sky survey ([Sazonov et al. 2021](#)). The

luminosity function ranged from $10^{42.5} \leq L_X \leq 10^{45}$ erg s $^{-1}$ and was best-fitted by a power-law with a slope of 0.6 ± 0.2 .

Since the X-ray bright TDEs presented in our study were not discovered by an X-ray survey, but instead from inhomogeneous follow-up X-ray observations of optically discovered TDEs, and given that the criteria and cadence for X-ray follow-up was not uniform, we cannot use our sample to obtain an *absolute* X-ray luminosity function as obtained by [Sazonov et al. \(2021\)](#). Instead, what we propose to do is to combine all TDEs discovered by X-ray survey with our sample of optically selected X-ray detected TDEs to construct a *relative* luminosity function but with wider luminosity range and lower uncertainty per luminosity bin than the one constructed from *SRG/eROSITA*, in order to better constrain its shape.

To construct a large sample of X-ray TDEs, we combine our 17 sources, the 13 discovered by *SRG/eROSITA* ([Sazonov et al. 2021](#)), with 6 discovered by *ROSAT*/RASS and 8 discovered by the *XMM-Newton* Slew Survey as presented in the recent review by [Saxton et al. \(2020\)](#), resulting in 44 X-ray detected TDE ranging from $10^{41} \leq L_X \leq 10^{45}$ erg s $^{-1}$.

We follow the procedures detailed in [van Velzen \(2018\)](#) to construct a *relative* luminosity function from a combined sample discovered by distinct surveys with distinct selection functions and detection efficiency, assuming that each survey discovers events from the same parent distribution so that we can use the discovered/detected number of TDE in each survey to compare the selection efficiencies and thus obtain the *relative* LF. The *effective* $A_{\text{survey}} \times \tau_{\text{survey}}$ (see Eq. 5) for each survey can be estimated from:

$$N_{\text{TDE,detected}} \approx \dot{N} V(z_{\text{max}*}) A_{\text{survey}} \times \tau_{\text{survey}} \quad (6)$$

where $N_{\text{TDE,detected}}$ is the number of TDEs detected by the survey, and $V(z_{\text{max}*})$ denotes the comoving volume (per solid angle) corresponding to maximum redshift ($z_{\text{max}*}$) the survey can detect a ‘typical’ X-ray TDE. We define a ‘typical’ X-ray TDE to have $L_X^* = 10^{43}$ erg s $^{-1}$ and $T_{\text{in}}^* = 60$ eV, and use the detection limit flux ($F_{X,\text{lim}}$) of each survey (see Table 3) to determine $z_{\text{max}*}$ for each survey. For the optical survey, we assume $F_{X,\text{lim}}$ to be the flux limit of *Swift*/XRT in a stacked exposure time of 10ks. In eq. 6 \dot{N} is the *assumed* mean event rate which was chosen to be $\dot{N} = 2 \times 10^{-7}$ Mpc $^{-3}$ yr $^{-1}$, following [Sazonov et al. \(2021\)](#). The resulting $A_{\text{survey}} \times \tau_{\text{survey}}$ for each survey is shown in Table 3, while Table 5 show the detailed information from individual sources.

Table 3. Survey' Properties

Survey	N_{TDE}	$F_{X,lim}$	$(A_{survey} \times \tau_{survey})^*{}^a$
		(erg cm ⁻² s ⁻¹)	(deg ² yr)
ASASSN+ <i>Swift</i> /XRT	6(3) ^b	8×10^{-14}	138
ZTF+ <i>Swift</i> /XRT	12	8×10^{-14}	273
OGLE+ <i>Swift</i> /XRT	1	8×10^{-14}	22
ROSAT	6	2×10^{-13}	2009
XMMLS	9	5×10^{-13}	6484
eROSITA	14	8×10^{-14}	645

NOTE—(a) Effective $(A_{survey} \times \tau_{survey})$ as measured from Eq. 6. (b) Three were part of both in ZTF and ASASSN.

In the upper panel of Fig. 17, we show the distribution of the 44 TDEs in the redshift vs. peak L_X diagram, where boundaries of the nine $\Delta \log L_X$ bins are indicated with vertical lines. For a certain bin j with n_j TDEs and width $\Delta_j \log L_X$, the rate luminosity function is $\phi_j = \left[\sum_{i=1}^{n_j} \frac{1}{V_{max,i}} \right] / \Delta_j \log L_X$, we compute the corresponding uncertainty of ϕ_j based in the Poisson error (Gehrels 1986). For example when $n_j = 1$, the upper and lower limits of ϕ_j are $\phi_j^u = \phi_j \times 3.30/1$ and $\phi_j^l = \phi_j \times 0.17/1$, and when $n_j = 11$, $\phi_j^u = \phi_j \times 14.27/11$ and $\phi_j^l = \phi_j \times 7.73/11$. We show ϕ_j vs. $\log L_X$ in the bottom panel of Fig. 17.

First, we fit the seven LF data points with a single power-law of:

$$\phi(L_X) = \dot{N}_0 \left(\frac{L_X}{L_0} \right)^{-\gamma} \quad (7)$$

For $L_0 = 10^{43}$ erg s⁻¹, we obtained $\gamma = 1.2 \pm 0.1$. The best-fit model, shown as an orange line in the bottom panel of Fig. 17, is steeper than the power-law model with $\gamma = 0.6 \pm 0.2$ present by Sazonov et al. (2021), however, the fit seems to slight over predict the number of low L_X sources and the number of sources with $L_X \geq 10^{44.5}$ erg s⁻¹.

Next, we describe the luminosity function with a broken (or double) power-law in the form of:

$$\phi(L_X) = \dot{N}_0 \left[\left(\frac{L_X}{L_{bk}} \right)^{\gamma_1} + \left(\frac{L_X}{L_{bk}} \right)^{\gamma_2} \right]^{-1} \quad (8)$$

where $-\gamma_1$ is the faint-end slope, $-\gamma_2$ is the bright-end slope, and L_{bk} is the characteristic break luminosity. We perform the fit with MCMC, obtaining $\gamma_1 = 0.96^{+0.21}_{-0.24}$, $\gamma_2 = 2.65^{+1.1}_{-0.90}$, and $\log L_{bk} = 44.1^{+0.4}_{-0.5}$ erg s⁻¹. The Bayesian information criterion (BIC) value of the broken

power-law fit is smaller than the single power-law fit by 7.1. According to Raftery (1995), a BIC difference of 0–2 is weak, a of 2–6 is positive, and a difference of 6–10 is strong. Therefore, we conclude that the broken power-law LF provides a better description of the data. The break in the LF around $L_X \approx 10^{44}$ erg s⁻¹ will be discussed in §5.7.

Our best-fit γ_1 below the brake is steeper than the $\gamma = 0.6 \pm 0.2$ obtained by Sazonov et al. (2021), this means that that authors are either underestimating the low L_X end of the LF or/and overestimating the high end of the LF, if we assume the same normalization (rate of TDEs). In their selection of candidates Sazonov et al. (2021) has only considered sources in which the observed flux was at least 10 time brighter than the previous upper limit, such selection bias the discovery rate against low luminosity sources, which may indicate that their LF is underestimating the low L_X end of the LF. Furthermore, our results indicates that LF extends to L_X 's below $10^{42.5}$ erg s⁻¹ (Sazonov et al. (2021)'s lowest L_X bin), at least as low as $L_X \approx 10^{41}$ erg s⁻¹. This indicates that there is a large population of TDEs that could be detected in the X-rays, but that are just too faint to be detected by current instruments unless those happen at very low z , it also shows that the absolute rate estimated by the authors is just a lower limit on the rate of TDEs with X-rays emission.

5. DISCUSSION

5.1. On the diversity of X-ray evolution: delayed accretion or variable optical depth? an orientation effect?

As we have shown in §4.1, optically selected TDEs have a large diversity in X-ray evolution, with sources rarely showing prompt ($\Delta t \leq 100$ days) bright ($L_X \geq 10^{43}$ erg s⁻¹) X-ray emission that decays as a power-law with time as predicted from simple fallback accretion models. Instead, most sources show a faint X-ray emission at early times, with a subset showing a delayed increase in the observed X-ray luminosity, while others showing a faint and approximately constant X-ray luminosity during the UV/optical evolution.

From our X-ray spectral and SED analyses, a number of conclusions can be drawn:

- The X-ray emission temperature (T_p) decreases with time (see Fig. 8);
- The decrease in T_p is independent of the L_X , given that *Late-time brightening* sources show highest T_p at early times, when the L_X is minimum.
- This independent T_p and L_X evolution creates a decoupling between the two parameters in these

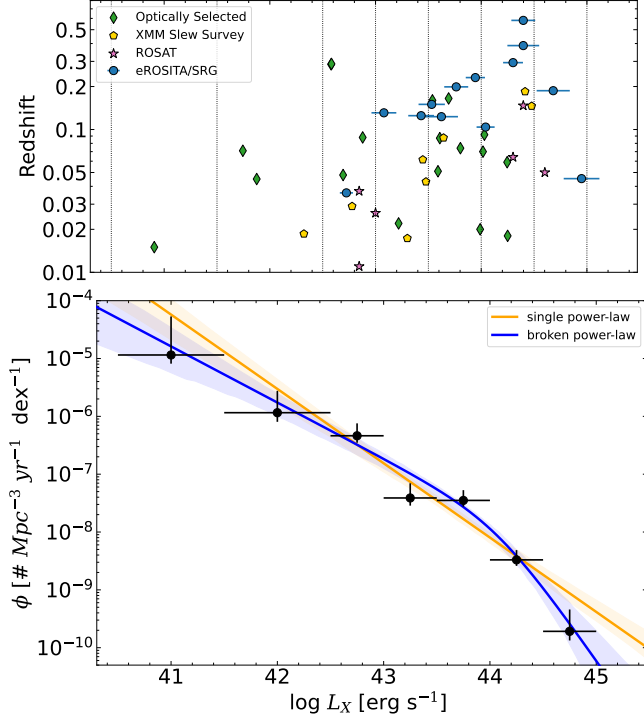


Figure 17. Top: Distribution of Redshift \times peak X-ray luminosity (L_X) for all the sources included in the X-ray luminosity function analyses. Bottom: Derived luminosity function (black points), best-fitted single power-law (orange line), best-fitted broken power-law (blue line).

epochs/sources. Other epochs/sources show a $L_X \propto T^\alpha$ relation (see Fig. 9).

- The highest T_p with lowest L_X results in an unphysical value for the X-ray emission radius (R_p/R_g) for these source/epochs. For other epochs/epoch R_p is consistent with R_{ISCO} (see Fig. 10).
- The epochs with unphysical R_p/R_g are also the epochs in which UV/optical to X-ray ratio (L_{BB}/L_X) is too high to be produced by *bare/unreprocessed* accretion disk (see Fig. 11).
- There is a large range of observed L_{BB}/L_X values at early times ($0.5 \leq L_{BB}/L_X \leq 3000$); at late times these values converge to ($0.5 \leq L_{BB}/L_X < 10$), see Fig. 14.
- There is no M_{BH} dependence on the presence/absence of luminous X-ray emission ($L_X \geq 10^{42}$ erg s $^{-1}$).

Viable theoretical models for the TDE emission mechanism must be able to reproduce these observational findings.

A possible explanation for the late-time brightening of the X-ray emission, put forward by several authors (e.g., Gezari et al. 2017; Liu et al. 2019), is the delayed formation of the accretion disk in these sources. Some problems arise from this interpretation:

- i) faint soft X-ray emission ($L_X \leq 10^{42}$ erg s $^{-1}$) is detected in the early times for most of the *late-time brightening* sources in which an exposure deep enough to detect such faint emission is available (the upper limits on AT2020ksf and OGLE16aa are higher than 10^{42} erg s $^{-1}$, the two are also the highest redshift sources); which means that the structure responsible for X-ray emission in this sources is already present at very early times;
- ii) the temperature of these X-ray faint phases are as high or higher than the temperatures at the late-time;
- iii) the overall evolution of the temperature is consistent with a cooling accretion disk (see Fig. 8), that would not necessarily be the case if the late time X-ray emission is tracing a different physical structure (disk) than the early time is tracing (stream-stream shocks), like proposed by Liu et al. (2019);
- iv) if the presence of bright X-ray emission ($L_X > 10^{42}$ erg s $^{-1}$) is driven by the successful circularization of the debris streams, while in sources with $L_X \leq 10^{42}$ erg s $^{-1}$ these do not circularize to form a disk; there should be a distinct M_{BH} distribution underlying the two populations – given the strong M_{BH} dependence in the circularization time (Bonnerot et al. 2016) – as we have shown in Fig. 16, there is not difference in their M_{BH} distribution.

As we argued in §4.2.1, the suppression of the observed X-ray emission in the early times of the *Late-time brightening* and *X-ray faint* source can explain all the points listed above, independently of the model assumed for such suppression. If the X-ray luminosity is suppressed in these epochs/sources with minimal change in the observed temperature (or spectral shape), all the above-listed properties would be naturally produced.

Suppression of the X-ray emission is an expected consequence of different TDE models that invoke the reprocessing of the X-ray emission into the UV/optical wavelengths by an optionally thick material, these models, known as the *reprocessing scenario* (e.g., Loeb & Ulmer 1997; Ulmer 1999; Coughlin & Begelman 2014; Metzger & Stone 2016; Roth et al. 2016; Dai et al. 2018; Thomsen et al. 2022; Parkinson et al. 2022; Metzger 2022), assume different physical processes and geometries, but have the common property of the suppression of the X-ray emission at the highest accretion rates, i.e., early times, and its re-emission at lower energies.

Although a large fraction of the optical TDEs in our sample shows suppression of the X-ray emission at early

times, some do not, namely, ASASSN-14li, AT2019dsg, and AT2019ehz; this is also true for most X-rays discovered TDEs (comparison between these populations will be presented in §5.5). Instead, there is an at least three orders of magnitude range in observed $L_{\text{BB}}/L_{\text{X}}$ at early times (see Fig. 14, and 15). Some of this diversity was already previously known and had inspired a series of models where the presence/absence of strong reprocessing is orientation dependent (Dai et al. 2018; Parkinson et al. 2022; Thomsen et al. 2022).

In these models, the reprocessing is produced by the disk outflow, where at the highest accretion rate, i.e., early times, if the source is seen at lower inclination angles with respect to the disk pole, the reprocessing is minimal, and the observed SED resembles a disk SED (i.e., $L_{\text{BB}}/L_{\text{X}} \leq 10$ if $\log(T_p) \geq 5.6$ K, see Appendix §B); at the largest inclination angles (near edge-on) most of the X-ray emission should be reprocessed to the to lower energies, making the X-rays undetectable, and high lower limits on $L_{\text{BB}}/L_{\text{X}}$ to be measured. When seen at intermediate angles, only a small fraction of the X-ray can escape unprocessed; the SED is then UV/optical dominated ($L_{\text{BB}}/L_{\text{X}}$ between $\text{few} \times 10^1$ to $\text{few} \times 10^3$), but faint X-rays are still able to escape and be detected. As the accretion rate decreases, the optical depth of the reprocessing layer decreases, allowing for a larger fraction of the X-ray photons to escape, which can produce the X-ray late-time brightening as shown by Thomsen et al. (2022). At extreme edge-on angles, the colder parts of the disk may still be able to absorb the X-rays that may never be able to escape, even at late times. The convergence of the $L_{\text{BB}}/L_{\text{X}}$ values to disk-like values at late times in our sample is also an expected outcome of this orientation-dependent and time-evolving reprocessing layer (Thomsen et al. 2022).

In the left panel of Fig. 18, we show four early-time SEDs with a diverse range of $L_{\text{BB}}/L_{\text{X}}$ values, while in the right panel, we show the four simulated SEDs for distinct inclination angles as presented by Dai et al. (2018). A direct comparison is, of course, not valid, given that in Dai et al. (2018) models, the only parameter changed between the SEDs is the viewing angle towards the system; every other parameter of the system is fixed, while in reality, our four example sources/SEDs may have distinct black hole masses, black hole spin, impact parameter (β), peak disk temperature, radial profile of the disk temperature and many other differences, that could also shape the SED, however, it is interesting to note that the large diversity of $L_{\text{BB}}/L_{\text{X}}$ observed can be, in principle, produce just by a change in viewing angle.

As we pointed out in §4.2.1, an important characteristic of the early suppression of the X-ray emission in

the *late-time brightening* and *X-ray faint* sources is that such suppression has a minimal effect in the measured T_p , this means that the optical depth of the reprocessing-layer must have a *quasi-gray* shape in the 0.3-1.0 keV band so that the observed flux is suppressed with small effect in the spectrum shape. In most of the radiative transfer simulations performed (e.g., Dai et al. 2018; Parkinson et al. 2022; Thomsen et al. 2022) the suppression of the X-rays is driven by a combination of *adiabatic expansion*, bound-free interactions (absorption and re-emission) and electron scattering by a reprocessing-layer of ionized gas; these effects should not be confused with absorption by a neutral medium (modeled, e.g., by the TBabs in xspec) which in contrast, has a strong energy dependence in the soft X-rays. Unfortunately, such confusion is sometimes present in some studies.

The X-ray spectra of TDEs are, in the majority of cases, only detected above background in an extremely narrow energy range (0.3-1.0 keV); however, as shown by the blue curve in Figure B1 of Thomsen et al. (2022) the combined optical depth of the three physical processes mentioned above, have very little energy dependence in the 0.3-1.0 keV range for intermediate viewing angles. Furthermore, the TDE X-ray spectra are extremely steep, with an observed flux density ($F_E(E)$), between 0.3 keV and 1.0 keV that can be as steep as $\frac{F_E(0.3 \text{ keV})}{F_E(1.0 \text{ keV})} \approx \text{few} \times 10^3$ for the lowest T_p spectra (see, e.g., AT2019dsg spectrum in Fig. 3), and at minimum as steep as $\frac{F_E(0.3 \text{ keV})}{F_E(1.0 \text{ keV})} \approx 10$ for higher T_p values (see e.g., AT2018zr spectrum in Fig. 3). Therefore a strong energy dependence on the optical depth would be necessary to change the measured T_p considerably, and this is not the case. Hence a suppression on the X-ray flux can be achieved without great changes in the X-ray spectral shape.

Such an ionized gas layer should, in principle, leave absorption features in the X-ray spectra; however, at extreme column densities ($N_{H,\text{ion}}^9 \gg 10^{23} \text{ cm}^{-2}$) at these early phases – when the system seems at intermediate viewing angles from the disk pole – the optical depth is high ($\tau_{\text{ion}} \approx 10$, see Figure B1 of Thomsen et al. 2022) in the entire observable X-ray energy range, making the observable X-ray flux drop and hence the S/N. The low S/N and the low resolution of X-ray CCD instruments in the soft bands make it impossible to detect such features. However, the column density should be lower at lower inclination angles, where features may be detectable.

⁹ We will use $N_{H,\text{ion}}$ to refer to an ionized gas column density. In contrast, we have used N_H to denote neutral column density.

The detection of a low column density, $N_{H,\text{ion}} \approx \text{few} \times 10^{21} \text{ cm}^{-2}$, ultra fast outflow (UFO, i.e. high velocity ionized gas), in the early time spectrum of ASASSN-14li by Kara et al. (2018), supports our interpretation that ASASSN-14li is seen at small inclination angles (see top left panel of Fig. 15), given that the mean optical depth in the 0.3-1.0 keV range for $N_{H,\text{ion}} \approx \text{few} \times 10^{21} \text{ cm}^{-2}$ is only $\tau_{\text{ion}} \approx 0.1$, hence not able to absorb any considerable fraction of the X-ray radiation, the optical depth is just slightly higher ($\tau_{\text{ion}} \approx 0.7$) at the O VII 0.57 keV transition, which allow for the detection of the absorption feature. See the bottom panel of Figure 1 in Ajay et al. in prep, for a plot of the τ_{ion} as a function of energy for ASASSN-14li's UFO. A direct consequence of this orientation driven reprocessing scenario is that mild column density ($N_{H,\text{ion}}$ up to $\text{few} \times 10^{22} \text{ cm}^{-2}$) UFO's could/should be detected at either the early time spectra of sources showing prompt bright X-ray emission (e.g., ASASSN-14li) or the late time spectra of *late-time brightening* sources.

The *flaring* source, AT2019ehz, has not been addressed yet; we first note that such short term flaring differs from the gradual late time X-ray increase of the *late-time brightening* sources, the reprocessing scenario does not work in this case, given that this system is bright at early times, fades, and then re-brightens, which would disagree with the net brightening predicted under the reprocessing scenario. Furthermore, the flaring behavior is accompanied by an increase in T_p , a relation between T_p and L_X is present (interestingly with the highest best-fitted α for a $L_X \propto T^\alpha$ relation), and no large variations in R_p is observed, with R_p/R_g always in the physically valid range. This behavior differs from the other sources with early X-ray faint emission – as extensively discussed above – and instead points towards a disk seen directly without much reprocessing, but with intrinsic variability.

One possibility is that X-ray variability is produced by random short term fluctuations in the peak disk temperature (Mummery & Balbus 2022). Alternatively, the nascent accretion disk may be initially misaligned with respect to the MBH's spin axis, which would induce relativistic torques on the disk and causes it to precess (Lense-Thirring precession), producing repeating flares, that should also modulate the observed T_p (Stone & Loeb 2012; Franchini et al. 2016). In this scenario relativistic torque effects align the disk and terminates precession and the flares; the flares are indeed not observed at late times in AT2019ehz, although the cadence of observation is not enough to confirm this. In both cases, a short term decoupling between the hotter (X-

ray) and colder (UV/optical) emission regions, as observed, would be expected.

A definitive explanation for the flaring behavior of AT2019ehz is not within the scope of this work, it may not be possible at all, given the cadence/quality of the available data. A TDE discovered in 2022 (Yao & Gezari 2022) has shown similar flaring behavior, for that source the cadence of the observations is much higher (several per day for hundreds of days), and distinct models for the flaring behavior will be tested in a forthcoming study (Yao, Guolo, et al. in prep).

5.2. On the origin of the UV/optical and X-ray emission

The soft X-ray emission observed in TDEs seems to follow all the expected characteristics of the inner region of a newly formed accretion disk, from the inferred radius to the temperature evolution (see §4.2.1). It is not clear how any alternative scenario for the X-ray emission would be able to produce the observed properties, in particular the formation of a hot hard X-ray emitting *corona* akin to AGN (see §4.2.2).

Although not every optically discovered TDE shows a strong UV/optical excess (e.g., ASASSN-14li, AT2019dsg and AT2019ehz do not show) at early times, most do. As we have argued in §5.1 the excess in UV/optical emission is accompanied by a suppression of the observed X-ray emission. The structure responsible for such excess needs therefore to also absorb the emitted X-rays, which favors the *reprocessing scenarios*. The physical nature of such a reprocessing layer may be a radiation-driven outflow formed under super-Eddington accretion (Miller et al. 2015; Dai et al. 2018; Parkinson et al. 2022; Thomsen et al. 2022), a quasi-static weakly bound envelope (Loeb & Ulmer 1997; Coughlin & Begelman 2014; Metzger 2022), or even optically thick gas from the self-collision shock (Lu & Bonnerot 2020). The fact that such reprocessing is not always present, and has a variable strength (continuous range of early time L_{BB}/L_X , see Fig. 14), indicates, as pointed in §5.1, that a geometric or viewing angle effect should also be present, as originally proposed by Dai et al. (2018). At the late-times, such UV/optical excess disappears (see Fig. 14), which translates into an optically thick \rightarrow thin transition of the reprocessing layer, given most sources' SEDs are consistent with a *bare/unreprocessed* accretion disk. A purely *bare/unreprocessed* disk emission at late-times is also supported by the late-time UV plateau observed in most TDEs (van Velzen 2018; Hammerstein et al. 2023a), which is naturally explained by the simultaneous cooling and decreasing accretion rate onto the sub-Eddington disk.

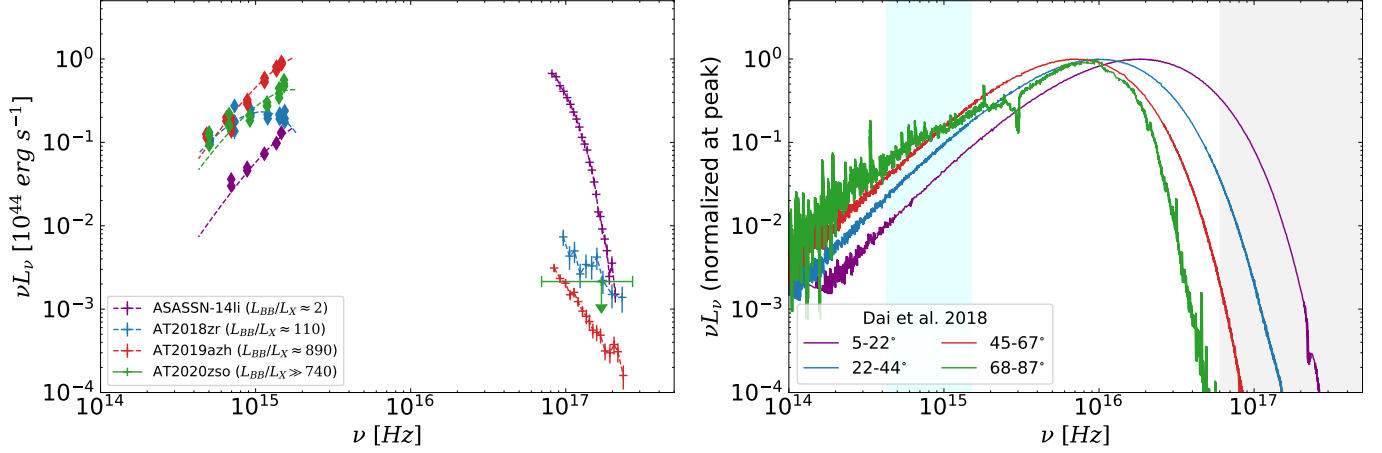


Figure 18. Comparison between observed SEDs and model SEDs by Dai et al. (2018). In the right we show the early time (near UV/optical peak) observed SED for ASASSN14-li, AT2018zr and AT2019azh (this work) as well as for AT2020zso (Wevers et al. 2022), showing a large range of $L_{\text{BB}}/L_{\text{X}}$ values. The left panels show Dai et al. (2018)’s early time simulated SEDs as seen by distinct viewing angles from the disk pole: face-on = 0° and edge-on = 90° .

5.3. On the large population of X-ray quiet TDEs

As we have shown in §4.4, most (up to 60%) discovered by optical surveys are X-ray quiet ($L_{\text{X}} \leq 10^{42} \text{ erg s}^{-1}$), the definitive picture for why that is the case is beyond the scope of this paper. However, a couple of insights can be made.

First, TDEs with $L_{\text{X}} \leq 10^{42} \text{ erg s}^{-1}$ do exist, as we have demonstrated, and should be common given: *i*) the derived LF (see §4.5), *ii*) the orientation effects (see §5.1) that make a large fraction of X-ray emission from TDE seen at more edge-on inclinations to be reprocessed to the UV/optical.

However, such X-ray luminosities can hardly be observed unless the TDE happens at extremely low redshifts. Even with a modest ~ 20 ks *XMM-Newton* observation upper-limits of $L_{\text{X}} \approx 10^{41} \text{ erg s}^{-1}$ can rarely be placed for the typical redshift range in which TDEs are observed (see the L_{X} upper limits for the non-detected TDE in Table 2). Sometimes these sources show a strong late-time X-ray rebrightening, but not always (e.g., AT2018zr, AT2018hyz, and AT2019qiz); besides, if a TDE is not detected at early times – which for $L_{\text{X}} \leq 10^{42} \text{ erg s}^{-1}$ only occurs for the nearest sources – it is unlikely that this source will continue to be followed-up by an X-ray instrument, much less by *XMM-Newton*.

Furthermore, to be able to produce observable radiation in the 0.3-2 keV range from an accretion disk, the inner temperature (T_{p}) must necessarily be $\geq 10^{5.1} - 10^{5.2} \text{ K}$, since at lower peak temperatures the emission is shifted entirely to the extreme UV.

For a Galactic like gas-to-dust ratio ($N_{\text{H}} = 5.5 \times 10^{21} \times E(B-V)$), soft X-rays are more absorbed than UV light. For instance, with $N_{\text{H}} = 5 \times 10^{20} \text{ cm}^{-2}$ ($E(B-V) = 0.09$), about 74% of 0.3 keV X-rays get absorbed, while

only 42% of 2600 \AA UV light is. With higher absorption of $N_{\text{H}} = 1 \times 10^{21} \text{ cm}^{-2}$ ($E(B-V) = 0.18$), 93% of X-rays and 67% of UV are absorbed¹⁰. Therefore, soft X-rays photons are more affected by absorption along our line of sight than UV photons, making them harder to detect given same emitted flux. See for example the cases of AT2021mhg, AT2021sdu and AT2021yte in §4.4.

Finally, it is still possible that the circularization of the stellar debris does not happen, and no accretion disk is formed in these sources. In contrast, another process, independent of accretion, such as shocks produced by the intersection between the streams, would be responsible for all the UV/optical emission. Although it is not clear why the proposed lack of circularization is not dependent on M_{BH} , see Fig. 16.

The combination of the effects mentioned above is likely to be able to explain the large fraction of optically discovered TDE with no observable X-ray emission.

5.4. On the bolometric luminosity of TDEs

As pointed out by several authors (e.g., Dai et al. 2018; Lu & Kumar 2018; Thomsen et al. 2022; Mummery et al. 2023) a ‘missing energy’ problem will only arise when the integrated UV/optical (fitted with a blackbody function) is incorrectly considered as the bolometric luminosity of the TDE. This is an obvious statement for the sources with detected X-ray emission (see Fig. 2), but should also be true for those in which X-ray emission is not detected, since the bulk of the TDE emission should be emitted in the extreme UV (EUV) bands (see

¹⁰ For this calculation a standard Wilms et al. (2000) abundance was assumed for the X-ray absorption, using TBabs, while the UV extinction was based on Calzetti et al. (2000) law.

right panel of Fig. 18) which is not adequately modeled by the single temperature blackbody assumption for the UV/optical emission (see also right panel of Figure 5 in Dai et al. 2018).

When the full SED is consistent with a *bare/unreprocessed* accretion disk, i.e., the extrapolated disk model fitted from the X-rays matches the observed UV/optical (usually when $L_{\text{BB}}/L_{\text{X}} < 10$, see ASASSN-14li and late-time AT2019azh panel in Fig. 15), the bolometric luminosity can be computed simply by integration over the disk SED. We note, however, that if a *bare/unreprocessed* disk SED is assumed in cases where there is X-ray suppression, e.g., early-times of AT2019azh or AT2018zr, where $L_{\text{BB}}/L_{\text{X}} \gg 100$, the resulting SED will be based on an unphysical normalization ($R_p/R_g \leq 0.3$) and hence will underestimate the true bolometric luminosity, even if considering the ‘disk bolometric luminosity’.

For the cases – usually at early times – in which the strong UV/optical excess (i.e., $L_{\text{BB}}/L_{\text{X}} > 100$) is present (see again right panel of Fig. 18) the SED shape is strongly dependent on the radiative processes involved, and have large uncertainties because of the lack of constraints in the unobservable EUV waveband.

5.5. On the unification of the TDE population: survey selection biases and the lack of an optical/X-ray dichotomy

As we have shown, optical surveys can discover TDEs with a large range of $L_{\text{BB}}/L_{\text{X}}$ at early times, as we argue in §5.1 some (if not most) of this diversity can be explained by the viewing angle towards the system. We would like to compare the TDEs discovered by optical surveys and by X-ray surveys to look for differences (or lack thereof) in these populations and, if present, what could drive such differences.

TDEs discovered by most X-ray missions (e.g., *ROSAT* and *XMM-Newton* Slew Survey) had very little to no real-time UV/optical follow-up; hence accessing their $L_{\text{BB}}/L_{\text{X}}$ ratio is not possible. We thus focused our analyses on the more recent sources discovered by *SRG*/eROSITA, in particularly the 13 TDEs presented Sazonov et al. (2021) and eRASSt J074426.3 +291606 (hereafter J0744) presented by Malyali et al. (2023). Unfortunately, the sources presented in Sazonov et al. (2021) had no UV follow-up, but some constraints on the optical emission from ground-base optical time-domain surveys were obtained.

As reported by Sazonov et al. (2021), all of their sources had L_g/L_{X} ¹¹ ratios lower than 0.3. For a typical UV/optical blackbody temperature of 20,000 K (Hammerstein et al. 2023a), this translates into $L_{\text{BB}}/L_{\text{X}} \leq 3$. Such values, however, do not mean that these sources were ‘X-ray only’. For example, the early time $L_{\text{BB}}/L_{\text{X}}$ of ASASSN-14li and AT2019dsg were also lower than 3. This is also true for J0744, which had $L_{\text{BB}}/L_{\text{X}} \approx 2$ at early times. Most of the sources in Sazonov et al. (2021) had no optical counterpart detection, given the relatively high redshift range of their sample (all but one have $z > 0.1$, compare with our sample, in Table 1), ground-based optical surveys are not sensitive enough to detect the typical optical TDE luminosities at these redshifts. For the sources with detected optical counterparts, the range of $L_{\text{BB}}/L_{\text{X}}$ was $\sim 0.1 \leq L_{\text{BB}}/L_{\text{X}} \leq 2$. As discussed in §5.1, for these values of $L_{\text{BB}}/L_{\text{X}}$, no UV/optical excess is necessarily present; the shape of the SED shape is fully consistent with an *bare/unreprocessed* accretion disk; hence these systems are likely to be seen at lower angles (i.e., towards face-on orientations), similar to ASASSN-14li and AT2019dsg. The small variations observed in the $L_{\text{BB}}/L_{\text{X}}$ can be fully explained by a range of values of T_p , that as shown in appendix §B can produce $L_{\text{BB}}/L_{\text{X}}$ as low as ~ 0.05 for the range of T_p found in TDEs.

The distribution of $L_{\text{BB}}/L_{\text{X}}$ at early times for sources discovered by distinct methods/surveys is presented in Fig. 19. Triangles are lower limits on $L_{\text{BB}}/L_{\text{X}}$ (i.e., no X-ray detection), inverse triangles are an upper limit on $L_{\text{BB}}/L_{\text{X}}$ (i.e., no UV/optical detection), filled markers represent detections in both UV/optical and X-rays. In Fig. 20 we show the peak L_{BB} vs. the early time L_{X} , where the distinct symbols shows: *SRG*/eROSITA (squares) TDEs, optically selected X-ray detected (circles) and optically selected with no X-ray detection (diamond); filled marker show detection in both optical/UV (y-axis) and X-ray (x-axis), while hollow markers either UV/optical or X-rays (at early times) were no detected, similarly to Fig.19 distinct color represents the different references.

From Fig. 19, it is clear that there is no obvious dichotomy between optical and X-ray discovered TDEs. Instead, there is a continuous distribution of $L_{\text{BB}}/L_{\text{X}}$ values at early times, that is at least as wide as $L_{\text{BB}}/L_{\text{X}} \in (0.1, 32000)$. This can be explained by the fact that surveys at distinct wavelengths will be biased to discover sources that are brightest in that wavelength range. Optical surveys will discover mostly sources with high

¹¹ Where L_g is the optical *g*-band luminosity.

L_{BB}/L_X , up to 60% of which with $L_X \leq 10^{42} \text{ erg s}^{-1}$ (see §4.4), but will still sometimes discover sources with lower L_{BB}/L_X , such as ASASSN-14li and AT2019dsg. X-ray surveys, on the other hand, will most likely discover sources with lower L_{BB}/L_X , but not always; AT202ksf, for example, had no X-ray detection at early times ($L_{\text{BB}}/L_X \geq 25$), was not identified in real-time as a TDE candidate by optical surveys, and later ($\Delta t \sim 200$ days) was discovered by *SRG*/eROSITA following its X-ray brightening. The same holds for their distribution in $L_{\text{BB}} \times L_X$ plane of Fig. 20, there is a continuous distribution of the X-ray and UV/optical selected populations, instead of clear dichotomy between them.

An *unbiased*¹² discovery of TDEs would be possible with either: *i*) the simultaneous operation of an wide field-of-view (FoV) X-ray survey telescope with UV follow-up capabilities (e.g., STAR-X, Hornschemeier et al. 2023) and a wide FoV optical survey (e.g. LSST, Ivezić et al. 2019), *ii*) or the simultaneous and coordinated operation of an wide FoV UV survey telescope (e.g. ULTRASAT and/or UVEX, Sagiv et al. 2014; Kulkarni et al. 2021) and wide FoV X-ray survey telescope (e.g., *SRG*/eROSITA and/or *Einstein Probe*, Sunyaev et al. 2021; Yuan et al. 2015).

5.6. On the conditions for and consequences of corona formation

The so-called *corona*, and its characteristic power-law spectrum, is one of the main emission components in X-ray astronomy and a ubiquitous consequence of accretion onto compact objects. It is now widely accepted that such emission is produced by the Comptonization of lower energies photons produced in the accretion disks by a corona of hot electrons (Haardt & Maraschi 1991; Titarchuk & Lyubarskij 1995) located within a light-hour from the accreting massive black hole (Fabian et al. 2009). The spectrum created by this process depends on the Compton parameter y , given by:

$$y = \frac{k T_e}{m_e c^2} \max(\tau_e, \tau_e^2) \quad (9)$$

where τ_e and T_e are, respectively, the corona optical depth and electron temperature of the corona. It can be shown (Shapiro et al. 1976) that the spectrum resulting from the Comptonization is a power-law with a photon index given by:

¹² This is still biased towards dust free host galaxies, for heavily dust obscured TDEs, the UV/optical and soft X-ray are absorbed and re-emitted in the infrared, see for example Panagiotou et al. (2023).

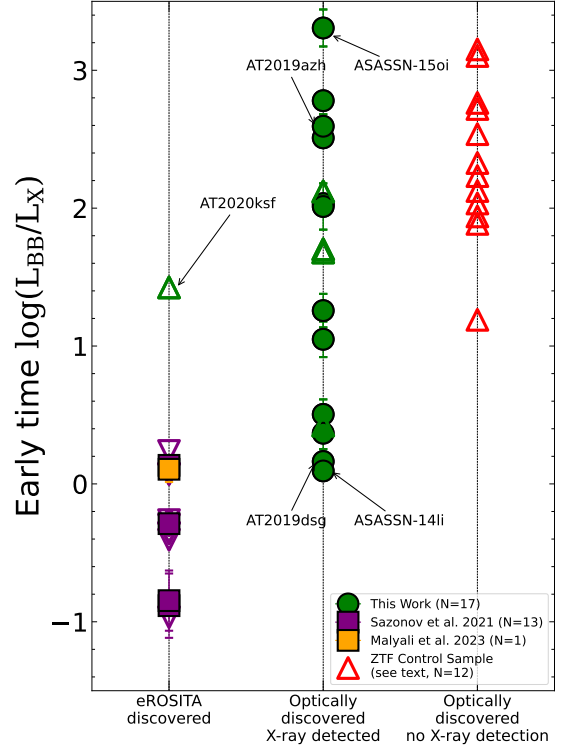


Figure 19. Distribution of early time L_{BB}/L_X based on discovery wavelength/survey. Extreme sources are marked with arrow. Triangles are lower limits on L_{BB}/L_X (i.e., no X-ray detection), inverse triangles are an upper limit on L_{BB}/L_X (i.e., no UV/optical detection), filled markers represent detections in both UV/optical and X-rays. Color represent distinct samples or references. Sources with extreme values are marked with arrows. There is a continuous and wide distribution of L_{BB}/L_X values, instead of a clear dichotomy between optically and X-ray discovered TDEs.

$$\Gamma = -\frac{1}{2} + \sqrt{\frac{9}{4} + \frac{4}{y}} \quad (10)$$

Although the exact mechanism responsible for the corona formation is still to be fully understood, the need for a strong magnetic field is common feature of the different models. As presented in §4.2.2, three sources in our sample have shown a soft \rightarrow hard transition consistent with the formation of a corona; in all three sources, the spectrum is soft at early times, and the complete hardening of the X-ray spectrum is only observed at $\Delta t \geq 200$ days. This gradual hardening process suggests that it takes approximately 10^2 days for the magnetically dominated hot corona region to develop. The initial weak magnetic fields present in the bound debris could undergo amplification through the combined effects of the disk's differential rotation and the magnetorotational instability. (Balbus & Hawley 1991; Miller & Stone 2000; Yao et al. 2022).

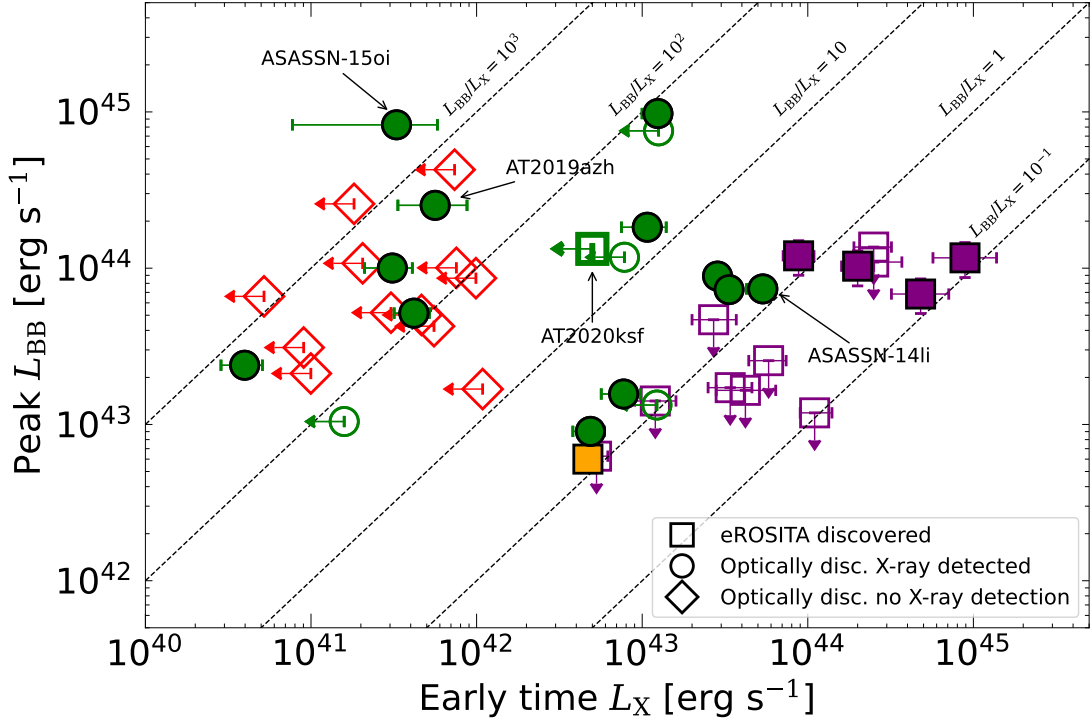


Figure 20. Distribution of peak $L_{\text{BB}} \times$ early time L_X for different TDE populations. Squares show *SRG*/eROSITA (X-ray) discovered sources, circles show optically discovered X-ray detected, while diamonds show optically discovered with no X-ray detection. Filled markers represent detections in both UV/optical and X-rays (early times), while hollow symbols represent upper limits in one of the two wavelength bands, where the arrows represent their 3σ upper limit. The colors are the same as in Fig. 19.

While the corona was able to form in these three sources, their hard state is short-lived, and the sources transition back to soft/intermediate state at even later times ($\Delta t \gg 400$ days); this indicates that the high optical depth corona can not be sustained as the accretion rate onto the black hole decreases. Another line of evidence towards the inefficiency of the corona formation is on the measured Γ_{sc} (see right panel of 13). In TDEs the spectra are rarely as hard in a typical AGN. From the combination of equations 9 and 10 these higher values of the power-law index in the TDEs, translates into lower values of the $T_e \times \max(\tau_e, \tau_e^2)$ product as compared with those in AGN corona. Disentangling between τ_e and T_e effects relies on the detection of cut-off energy (E_{cut}) of the power-law spectra. Such a measurement is possible using *NuSTAR* (Harrison et al. 2013) for some bright nearby AGN (e.g., Tortosa et al. 2018), however, this is still not feasible for TDEs with current instruments. The proposed High Energy X-ray Probe (*HEX-P*, Madsen et al. 2019) may allow measurements of E_{cut} and as well as detection of reflection features, in bright nearby TDE such as AT2021ehb. The reason for which only these three sources show corona formation are unclear at this time, while all three sources show $M_{\text{BH}} \geq 5 \times 10^6 M_{\odot}$ – which is in high mass end of the TDE M_{BH} function,

and expected from the requirement of sub-Eddington accretion for the formation of the component – a high M_{BH} does not seems to be sufficient condition, given that other TDEs were hosted by black holes with $M_{\text{BH}} \geq 5 \times 10^6 M_{\odot}$ and still did not show such state transition.

5.7. On the break of the luminosity function

In §4.5, we have shown that the TDE X-ray luminosity function (LF) can be described by a broken power-law with a characteristic break luminosity of $L_X \approx 10^{44}$ erg s $^{-1}$. In the case that the X-ray luminosity of TDEs are Eddington limited, and hence their fraction $l_x = L_X/L_{\text{Edd}}$ is < 1 , the observed suppression of the TDE rate at $M_{\text{BH}} > 10^8 M_{\odot}$ (van Velzen 2018; Yao et al. 2023) can naturally explain the brake in the X-ray LF at $\sim 10^{44}$ erg s $^{-1}$. Indeed, based on such arguments, Mummery (2021) estimated a *maximum* X-ray luminosity of $\sim 10^{44}$ erg s $^{-1}$ for non-jetted TDEs¹³. Although a couple TDEs have shown a peak $L_X > 10^{44}$ erg s $^{-1}$ (see top panel of Fig. 17), the steep break, from $\gamma \approx 1.0$

¹³ TDEs in which the jet is pointed towards us – so-called jetted or relativistic TDEs – have their luminosity beamed, hence those can reach $L_X \geq 10^{47}$ erg s $^{-1}$. This is a distinct physical scenario, than what is discussed in this section, therefore are not considered.

to $\gamma \approx 2.7$ in the LF is still in qualitative agreement with the limiting luminosity expectation, given that a TDE with peak $L_X = 10^{45} \text{ erg s}^{-1}$ should be ~ 1000 rarer than a TDE with peak $L_X = 10^{44} \text{ erg s}^{-1}$. TDEs with peak $L_X \gg 10^{44} \text{ erg s}^{-1}$ may be a result of extreme values in terms of the physical parameters involved in the stellar disruption, such as large M_{BH} and disrupted star masses, high black holes spin, and small impact parameters (β), furthermore likely an almost face-on view of the disk may be necessary so that no suppression/reprocessing of the X-ray emission occurs. Recently, Wiseman et al. (2023) and Subrayan et al. (2023) have shown that the extreme nuclear transient AT2021lwx has $L_X \geq 10^{45} \text{ erg s}^{-1}$, although the interpretation of such transient is still disputed, and very little is known about its X-ray spectra and evolution; the authors argue that if AT2021lwx is indeed the result of tidal disruption, extreme scenarios such as the disruption of $M_* \approx 15 M_\odot$ star (Subrayan et al. 2023) or a giant molecular cloud (Wiseman et al. 2023) by a $M_{\text{BH}} > 10^8$, need to be invoked to explain the transient emission.

6. CONCLUSIONS

We have analyzed the *XMM-Newton* and *Neil Gehrels Swift Observatory* X-ray and broad-band UV/optical emission of 17 optically selected X-ray detected TDEs discovered between 2014 and December 2021; we also compare our sample with the samples of optically discovered X-ray quiet TDEs and X-ray discovered TDEs, our main conclusions are:

- The X-ray light curves show a large diversity, with sources rarely showing a power-law decay and a large fraction showing a late-time brightening.
- The X-ray spectra are extremely soft in most sources and epochs, easily distinguishable from AGN X-ray spectra.
- The overall behavior of the measured radius (normalization) and temperature (shape) resulting from the X-ray spectral fitting is in agreement with that expected for the innermost region of a newly formed and time-evolving accretion disk, including the cooling of the peak temperature and a radius (in most cases) consistent with innermost stable orbit.
- Sources with early-time faint X-ray emission show an unphysical radius for the X-ray emission at these epochs, while their temperature behaves as expected, indicating the apparent suppression of their intrinsic early X-ray emission.

- The spectral energy distribution (SED) shape, as probed by the ratio (L_{BB}/L_X) between the UV/optical and X-ray luminosities, has a large range of values $L_{\text{BB}}/L_X \in (0.5, 3000)$ at early times, at late times the range converges to disk-like values, $L_{\text{BB}}/L_X \in (0.5, 10)$, for all sources.
- The combined X-ray spectral and SED properties and evolution favors a change in the optical depth (thick \rightarrow thin) of a reprocessing layer instead of the delayed formation of the accretion disk, in order to explain the late-time brightening of the X-ray emission.
- Three sources show a soft \rightarrow hard X-ray spectral transition, indicative of the formation of a hot corona akin to active galaxies, with the state transitions occurring at least 200 days after the UV/optical peak, but it is not sustained for more than a couple of months.
- We estimated that the fraction of optically discovered TDEs that are X-ray loud, with $L_X \geq 10^{42} \text{ erg s}^{-1}$, is at least 40% and that X-ray loudness is not dependent on M_{BH} .
- We show that the TDE X-ray luminosity function from $10^{41} \text{ erg s}^{-1}$ to $10^{45} \text{ erg s}^{-1}$ has a broken-power-law shape in the form of $dN/dL_X \propto L_X^{-1.0 \pm 0.2}$ at $L_X < L_{\text{bk}}$ and $dN/dL_X \propto L_X^{-2.7 \pm 1.0}$ at $L_X \geq L_{\text{bk}}$ with brake luminosity of $\log(L_{\text{bk}}) = 44.1^{+0.3}_{-0.5} \text{ erg s}^{-1}$. Which reveals a large population of TDE with $L_X \leq 10^{42} \text{ erg s}^{-1}$ (and high L_{BB}/L_X), which X-ray emission can not be detected with current instruments unless occurs at very low z .
- We show that there is no dichotomy between optical and X-ray discovered TDEs, and instead there is a continuous range of early time L_{BB}/L_X , at least as wide as $L_{\text{BB}}/L_X \in (0.1, 3000)$, with X-ray/optical surveys discovering preferentially, but not exclusively, from the lower/higher portion of the distribution.
- Our findings are consistent with the presence of an orientation-dependent, and time-evolving layer, that reprocesses and shift the disk emission to lower energies. With viewing-angle playing a crucial role in the unification of the TDE populations, as originally proposed by Dai et al. (2018).

Acknowledgments – M.G. thanks Thomas Wevers for introducing him to the field of TDEs and for the discussions on TDE physics. M.G. and S.G. are supported in part by NASA XMM-Newton grants 80NSS23K0621 and 80NSSC22K0571. E.H. acknowledges support by NASA under award number 80GSFC21M0002. This work is based on observations obtained with the Samuel Oschin Telescope 48-inch and the 60-inch Telescope at the Palomar Observatory as part of the Zwicky Transient Facility project. ZTF is supported by the National Science Foundation under grant No. AST-2034437 and a collaboration including Caltech, IPAC, the Weizmann Institute of Science, the Oskar Klein Center at Stockholm University, the University of Maryland, Deutsches Elektronen-Synchrotron and Humboldt University, the TANGO Consortium of Taiwan, the University of Wisconsin at Milwaukee, Trinity College Dublin, Lawrence Livermore National Laboratories, IN2P3, University of Warwick, Ruhr University Bochum, and Northwestern University. Operations are conducted by COO, IPAC, and UW. The ZTF forced-photometry service was funded under the Heising-Simons Foundation grant #12540303 (PI: Graham). This work has made use of data from the Asteroid Terrestrial-impact Last Alert System (ATLAS) project. The Asteroid Terrestrial-impact Last Alert System (ATLAS) project is primarily funded to search for near earth asteroids through NASA grants NN12AR55G, 80NSSC18K0284, and 80NSSC18K1575. This work made use of data supplied by the UK Swift Science Data Centre at the University of Leicester.

Software: `astropy` (Astropy Collaboration et al. 2013), `emcee` (Foreman-Mackey et al. 2013), `heasoft` (Heasarc 2014), `matplotlib` (Hunter 2007), `Prospector` (Johnson et al. 2021), `scipy` (Virtanen et al. 2020), `xspect` (Arnaud 1996).

Facilities: XMM, Swift, eROSITA, PO:1.2m., OGLE.

REFERENCES

- Agol, E., & Krolik, J. H. 2000, *ApJ*, 528, 161, doi: [10.1086/308177](https://doi.org/10.1086/308177)
- Alexander, K. D., Berger, E., Guillochon, J., Zauderer, B. A., & Williams, P. K. G. 2016, *ApJL*, 819, L25, doi: [10.3847/2041-8205/819/2/L25](https://doi.org/10.3847/2041-8205/819/2/L25)
- Arnaud, K. A. 1996, in *Astronomical Society of the Pacific Conference Series*, Vol. 101, *Astronomical Data Analysis Software and Systems V*, ed. G. H. Jacoby & J. Barnes, 17
- Astropy Collaboration, Robitaille, T. P., Tollerud, E. J., et al. 2013, *A&A*, 558, A33, doi: [10.1051/0004-6361/201322068](https://doi.org/10.1051/0004-6361/201322068)
- Bade, N., Komossa, S., & Dahlem, M. 1996, *A&A*, 309, L35
- Balbus, S. A., & Hawley, J. F. 1991, *ApJ*, 376, 214, doi: [10.1086/170270](https://doi.org/10.1086/170270)
- Blagorodnova, N., Gezari, S., Hung, T., et al. 2017, *ApJ*, 844, 46, doi: [10.3847/1538-4357/aa7579](https://doi.org/10.3847/1538-4357/aa7579)
- Blagorodnova, N., Neill, J. D., Walters, R., et al. 2018, *PASP*, 130, 035003, doi: [10.1088/1538-3873/aaa53f](https://doi.org/10.1088/1538-3873/aaa53f)
- Blagorodnova, N., Cenko, S. B., Kulkarni, S. R., et al. 2019, *ApJ*, 873, 92, doi: [10.3847/1538-4357/ab04b0](https://doi.org/10.3847/1538-4357/ab04b0)
- Bonnerot, C., Rossi, E. M., & Lodato, G. 2017, *MNRAS*, 464, 2816, doi: [10.1093/mnras/stw2547](https://doi.org/10.1093/mnras/stw2547)
- Bonnerot, C., Rossi, E. M., Lodato, G., & Price, D. J. 2016, *MNRAS*, 455, 2253, doi: [10.1093/mnras/stv2411](https://doi.org/10.1093/mnras/stv2411)
- Bright, J. S., Fender, R. P., Motta, S. E., et al. 2018, *MNRAS*, 475, 4011, doi: [10.1093/mnras/sty077](https://doi.org/10.1093/mnras/sty077)
- Brightman, M., & Nandra, K. 2011, *Monthly Notices of the Royal Astronomical Society*, 413, 1206, doi: [10.1111/j.1365-2966.2011.18207.x](https://doi.org/10.1111/j.1365-2966.2011.18207.x)

- Brown, G. C., Levan, A. J., Stanway, E. R., et al. 2017, *MNRAS*, 472, 4469, doi: [10.1093/mnras/stx2193](https://doi.org/10.1093/mnras/stx2193)
- Burrows, D. N., Hill, J. E., Nousek, J. A., et al. 2005, *SSRv*, 120, 165, doi: [10.1007/s11214-005-5097-2](https://doi.org/10.1007/s11214-005-5097-2)
- Calzetti, D., Armus, L., Bohlin, R. C., et al. 2000, *ApJ*, 533, 682, doi: [10.1086/308692](https://doi.org/10.1086/308692)
- Cannizzaro, G., Wevers, T., Jonker, P. G., et al. 2021, *MNRAS*, 504, 792, doi: [10.1093/mnras/stab851](https://doi.org/10.1093/mnras/stab851)
- Cannizzo, J. K., Lee, H. M., & Goodman, J. 1990, *ApJ*, 351, 38, doi: [10.1086/168442](https://doi.org/10.1086/168442)
- Cash, W. 1979, *ApJ*, 228, 939, doi: [10.1086/156922](https://doi.org/10.1086/156922)
- Cenko, S. B., Krimm, H. A., Horesh, A., et al. 2012, *ApJ*, 753, 77, doi: [10.1088/0004-637X/753/1/77](https://doi.org/10.1088/0004-637X/753/1/77)
- Cenko, S. B., Cucchiara, A., Roth, N., et al. 2016, *ApJL*, 818, L32, doi: [10.3847/2041-8205/818/2/L32](https://doi.org/10.3847/2041-8205/818/2/L32)
- Chornock, R., Berger, E., Gezari, S., et al. 2014, *ApJ*, 780, 44, doi: [10.1088/0004-637X/780/1/44](https://doi.org/10.1088/0004-637X/780/1/44)
- Conroy, C., Gunn, J. E., & White, M. 2009, *ApJ*, 699, 486, doi: [10.1088/0004-637X/699/1/486](https://doi.org/10.1088/0004-637X/699/1/486)
- Coughlin, E. R., & Begelman, M. C. 2014, *ApJ*, 781, 82, doi: [10.1088/0004-637X/781/2/82](https://doi.org/10.1088/0004-637X/781/2/82)
- Dai, L., McKinney, J. C., Roth, N., Ramirez-Ruiz, E., & Miller, M. C. 2018, *ApJL*, 859, L20, doi: [10.3847/2041-8213/aab429](https://doi.org/10.3847/2041-8213/aab429)
- Done, C., Davis, S. W., Jin, C., Blaes, O., & Ward, M. 2012, *MNRAS*, 420, 1848, doi: [10.1111/j.1365-2966.2011.19779.x](https://doi.org/10.1111/j.1365-2966.2011.19779.x)
- Evans, P. A., Beardmore, A. P., Page, K. L., et al. 2007, *A&A*, 469, 379, doi: [10.1051/0004-6361:20077530](https://doi.org/10.1051/0004-6361:20077530)
- . 2009, *MNRAS*, 397, 1177, doi: [10.1111/j.1365-2966.2009.14913.x](https://doi.org/10.1111/j.1365-2966.2009.14913.x)
- Fabian, A. C., Zoghbi, A., Ross, R. R., et al. 2009, *Nature*, 459, 540, doi: [10.1038/nature08007](https://doi.org/10.1038/nature08007)
- Foreman-Mackey, D., Hogg, D. W., Lang, D., & Goodman, J. 2013, *Publications of the Astronomical Society of the Pacific*, 125, 306, doi: [10.1086/670067](https://doi.org/10.1086/670067)
- Franchini, A., Lodato, G., & Facchini, S. 2016, *MNRAS*, 455, 1946, doi: [10.1093/mnras/stv2417](https://doi.org/10.1093/mnras/stv2417)
- French, K. D., Wevers, T., Law-Smith, J., Graur, O., & Zabludoff, A. I. 2020, *SSRv*, 216, 32, doi: [10.1007/s11214-020-00657-y](https://doi.org/10.1007/s11214-020-00657-y)
- Gabriel, C., Denby, M., Fyfe, D. J., et al. 2004, in *Astronomical Society of the Pacific Conference Series*, Vol. 314, *Astronomical Data Analysis Software and Systems (ADASS) XIII*, ed. F. Ochsenbein, M. G. Allen, & D. Egret, 759
- Gehrels, N. 1986, *ApJ*, 303, 336, doi: [10.1086/164079](https://doi.org/10.1086/164079)
- Gehrels, N., Chincarini, G., Giommi, P., et al. 2004, *ApJ*, 611, 1005, doi: [10.1086/422091](https://doi.org/10.1086/422091)
- Gezari, S. 2021, *ARA&A*, 59, doi: [10.1146/annurev-astro-111720-030029](https://doi.org/10.1146/annurev-astro-111720-030029)
- Gezari, S., Cenko, S. B., & Arcavi, I. 2017, *ApJL*, 851, L47, doi: [10.3847/2041-8213/aaa0c2](https://doi.org/10.3847/2041-8213/aaa0c2)
- Gezari, S., Chornock, R., Rest, A., et al. 2012, *Nature*, 485, 217, doi: [10.1038/nature10990](https://doi.org/10.1038/nature10990)
- Gilfanov, M., Sazonov, S., Sunyaev, R., et al. 2020, *The Astronomer's Telegram*, 14246, 1
- Greiner, J., Schwarz, R., Zharikov, S., & Orío, M. 2000, *A&A*, 362, L25. <https://arxiv.org/abs/astro-ph/0009430>
- Grupe, D., Thomas, H. C., & Leighly, K. M. 1999, *A&A*, 350, L31. <https://arxiv.org/abs/astro-ph/9909101>
- Guillochon, J., Manukian, H., & Ramirez-Ruiz, E. 2014, *ApJ*, 783, 23, doi: [10.1088/0004-637X/783/1/23](https://doi.org/10.1088/0004-637X/783/1/23)
- Gültekin, K., King, A. L., Cackett, E. M., et al. 2019, *ApJ*, 871, 80, doi: [10.3847/1538-4357/aaf6b9](https://doi.org/10.3847/1538-4357/aaf6b9)
- Haardt, F., & Maraschi, L. 1991, *ApJL*, 380, L51, doi: [10.1086/186171](https://doi.org/10.1086/186171)
- Hammerstein, E., van Velzen, S., Gezari, S., et al. 2023a, *ApJ*, 942, 9, doi: [10.3847/1538-4357/aca283](https://doi.org/10.3847/1538-4357/aca283)
- Hammerstein, E., Cenko, S. B., Gezari, S., et al. 2023b, *arXiv e-prints*, arXiv:2307.15705, doi: [10.48550/arXiv.2307.15705](https://doi.org/10.48550/arXiv.2307.15705)
- Harrison, F. A., Craig, W. W., Christensen, F. E., et al. 2013, *ApJ*, 770, 103, doi: [10.1088/0004-637X/770/2/103](https://doi.org/10.1088/0004-637X/770/2/103)
- Heasarc. 2014, *HEASoft: Unified Release of FTOOLS and XANADU*. <http://ascl.net/1408.004>
- HI4PI Collaboration, Ben Bekhti, N., Flöer, L., et al. 2016, *A&A*, 594, A116, doi: [10.1051/0004-6361/201629178](https://doi.org/10.1051/0004-6361/201629178)
- Hills, J. G. 1975, *Nature*, 254, 295, doi: [10.1038/254295a0](https://doi.org/10.1038/254295a0)
- Holoien, T. W. S., Prieto, J. L., Bersier, D., et al. 2014, *MNRAS*, 445, 3263, doi: [10.1093/mnras/stu1922](https://doi.org/10.1093/mnras/stu1922)
- Holoien, T. W. S., Kochanek, C. S., Prieto, J. L., et al. 2016a, *MNRAS*, 455, 2918, doi: [10.1093/mnras/stv2486](https://doi.org/10.1093/mnras/stv2486)
- . 2016b, *MNRAS*, 463, 3813, doi: [10.1093/mnras/stw2272](https://doi.org/10.1093/mnras/stw2272)
- Holoien, T. W. S., Huber, M. E., Shappee, B. J., et al. 2019, *ApJ*, 880, 120, doi: [10.3847/1538-4357/ab2ae1](https://doi.org/10.3847/1538-4357/ab2ae1)
- Hornschemeier, A., Zhang, W., STAR-X Team, & Kara, E. 2023, in *American Astronomical Society Meeting Abstracts*, Vol. 55, *American Astronomical Society Meeting Abstracts*, 120.05
- Hung, T., Gezari, S., Blagorodnova, N., et al. 2017, *ApJ*, 842, 29, doi: [10.3847/1538-4357/aa7337](https://doi.org/10.3847/1538-4357/aa7337)
- Hunter, J. D. 2007, *Computing In Science & Engineering*, 9, 90, doi: [10.1109/MCSE.2007.55](https://doi.org/10.1109/MCSE.2007.55)
- Ivezić, Ž., Kahn, S. M., Tyson, J. A., et al. 2019, *ApJ*, 873, 111, doi: [10.3847/1538-4357/ab042c](https://doi.org/10.3847/1538-4357/ab042c)
- Jiang, N., Wang, T., Hu, X., et al. 2021, *ApJ*, 911, 31, doi: [10.3847/1538-4357/abe772](https://doi.org/10.3847/1538-4357/abe772)

- Jiang, Y.-F., Guillochon, J., & Loeb, A. 2016, *ApJ*, 830, 125, doi: [10.3847/0004-637X/830/2/125](https://doi.org/10.3847/0004-637X/830/2/125)
- Johnson, B. D., Leja, J., Conroy, C., & Speagle, J. S. 2021, *ApJS*, 254, 22, doi: [10.3847/1538-4365/abef67](https://doi.org/10.3847/1538-4365/abef67)
- Kajava, J. J. E., Giustini, M., Saxton, R. D., & Miniutti, G. 2020, *A&A*, 639, A100, doi: [10.1051/0004-6361/202038165](https://doi.org/10.1051/0004-6361/202038165)
- Kara, E., Dai, L., Reynolds, C. S., & Kallman, T. 2018, *MNRAS*, 474, 3593, doi: [10.1093/mnras/stx3004](https://doi.org/10.1093/mnras/stx3004)
- Komossa, S., & Greiner, J. 1999, *A&A*, 349, L45. <https://arxiv.org/abs/astro-ph/9908216>
- Kosec, P., Pasham, D., Kara, E., & Tombesi, F. 2023, arXiv e-prints, arXiv:2308.05250, doi: [10.48550/arXiv.2308.05250](https://doi.org/10.48550/arXiv.2308.05250)
- Koss, M. J., Ricci, C., Trakhtenbrot, B., et al. 2022, *ApJS*, 261, 2, doi: [10.3847/1538-4365/ac6c05](https://doi.org/10.3847/1538-4365/ac6c05)
- Kulkarni, S. R., Harrison, F. A., Grefenstette, B. W., et al. 2021, arXiv e-prints, arXiv:2111.15608, doi: [10.48550/arXiv.2111.15608](https://doi.org/10.48550/arXiv.2111.15608)
- Lin, D., Maksym, P. W., Irwin, J. A., et al. 2015, *ApJ*, 811, 43, doi: [10.1088/0004-637X/811/1/43](https://doi.org/10.1088/0004-637X/811/1/43)
- Liu, X.-L., Dou, L.-M., Chen, J.-H., & Shen, R.-F. 2019, arXiv e-prints, arXiv:1912.06081, doi: [10.48550/arXiv.1912.06081](https://doi.org/10.48550/arXiv.1912.06081)
- Loeb, A., & Ulmer, A. 1997, *ApJ*, 489, 573, doi: [10.1086/304814](https://doi.org/10.1086/304814)
- Lu, W., & Bonnerot, C. 2020, *MNRAS*, 492, 686, doi: [10.1093/mnras/stz3405](https://doi.org/10.1093/mnras/stz3405)
- Lu, W., & Kumar, P. 2018, *ApJ*, 865, 128, doi: [10.3847/1538-4357/aad54a](https://doi.org/10.3847/1538-4357/aad54a)
- Madsen, K., Hickox, R., Bachetti, M., et al. 2019, in *Bulletin of the American Astronomical Society*, Vol. 51, 166
- Mainzer, A., Bauer, J., Cutri, R. M., et al. 2014, *ApJ*, 792, 30, doi: [10.1088/0004-637X/792/1/30](https://doi.org/10.1088/0004-637X/792/1/30)
- Makishima, K., Maejima, Y., Mitsuda, K., et al. 1986, *ApJ*, 308, 635, doi: [10.1086/164534](https://doi.org/10.1086/164534)
- Malyali, A., Liu, Z., Merloni, A., et al. 2023, *MNRAS*, 520, 4209, doi: [10.1093/mnras/stad046](https://doi.org/10.1093/mnras/stad046)
- Masci, F. J., Laher, R. R., Rusholme, B., et al. 2019, *PASP*, 131, 018003, doi: [10.1088/1538-3873/aae8ac](https://doi.org/10.1088/1538-3873/aae8ac)
- . 2023, arXiv e-prints, arXiv:2305.16279, doi: [10.48550/arXiv.2305.16279](https://doi.org/10.48550/arXiv.2305.16279)
- Metzger, B. D. 2022, *ApJL*, 937, L12, doi: [10.3847/2041-8213/ac90ba](https://doi.org/10.3847/2041-8213/ac90ba)
- Metzger, B. D., & Stone, N. C. 2016, *MNRAS*, 461, 948, doi: [10.1093/mnras/stw1394](https://doi.org/10.1093/mnras/stw1394)
- Miller, J. M., Kaastra, J. S., Miller, M. C., et al. 2015, *Nature*, 526, 542, doi: [10.1038/nature15708](https://doi.org/10.1038/nature15708)
- Miller, K. A., & Stone, J. M. 2000, *ApJ*, 534, 398, doi: [10.1086/308736](https://doi.org/10.1086/308736)
- Mitsuda, K., Inoue, H., Koyama, K., et al. 1984, *PASJ*, 36, 741
- Mummery, A. 2021, *MNRAS*, 507, L24, doi: [10.1093/mnrasl/slab088](https://doi.org/10.1093/mnrasl/slab088)
- Mummery, A., & Balbus, S. 2022, *MNRAS*, 517, 3423, doi: [10.1093/mnras/stac2844](https://doi.org/10.1093/mnras/stac2844)
- Mummery, A., & Balbus, S. A. 2020, *MNRAS*, 492, 5655, doi: [10.1093/mnras/staa192](https://doi.org/10.1093/mnras/staa192)
- . 2021, *MNRAS*, 505, 1629, doi: [10.1093/mnras/stab1141](https://doi.org/10.1093/mnras/stab1141)
- Mummery, A., Wevers, T., Saxton, R., & Pasham, D. 2023, *MNRAS*, 519, 5828, doi: [10.1093/mnras/stac3798](https://doi.org/10.1093/mnras/stac3798)
- Nicholl, M., Wevers, T., Oates, S. R., et al. 2020, *MNRAS*, 499, 482, doi: [10.1093/mnras/staa2824](https://doi.org/10.1093/mnras/staa2824)
- Panagiotou, C., De, K., Masterson, M., et al. 2023, *ApJL*, 948, L5, doi: [10.3847/2041-8213/acc02f](https://doi.org/10.3847/2041-8213/acc02f)
- Parkinson, E. J., Knigge, C., Matthews, J. H., et al. 2022, *MNRAS*, 510, 5426, doi: [10.1093/mnras/stac027](https://doi.org/10.1093/mnras/stac027)
- Pasham, D. R., Cenko, S. B., Levan, A. J., et al. 2015, *ApJ*, 805, 68, doi: [10.1088/0004-637X/805/1/68](https://doi.org/10.1088/0004-637X/805/1/68)
- Pasham, D. R., Lucchini, M., Laskar, T., et al. 2023, *Nature Astronomy*, 7, 88, doi: [10.1038/s41550-022-01820-x](https://doi.org/10.1038/s41550-022-01820-x)
- Piran, T., Svirski, G., Krolik, J., Cheng, R. M., & Shiokawa, H. 2015, *ApJ*, 806, 164, doi: [10.1088/0004-637X/806/2/164](https://doi.org/10.1088/0004-637X/806/2/164)
- Predehl, P., Andritschke, R., Arefiev, V., et al. 2021, *A&A*, 647, A1, doi: [10.1051/0004-6361/202039313](https://doi.org/10.1051/0004-6361/202039313)
- Quintin, E., Webb, N. A., Guillot, S., et al. 2023, arXiv e-prints, arXiv:2306.00438, doi: [10.48550/arXiv.2306.00438](https://doi.org/10.48550/arXiv.2306.00438)
- Raftery, A. E. 1995, *Sociological Methodology*, 25, 111. <http://www.jstor.org/stable/271063>
- Rees, M. J. 1988, *Nature*, 333, 523, doi: [10.1038/333523a0](https://doi.org/10.1038/333523a0)
- Remillard, R. A., & McClintock, J. E. 2006, *ARA&A*, 44, 49, doi: [10.1146/annurev.astro.44.051905.092532](https://doi.org/10.1146/annurev.astro.44.051905.092532)
- Ricci, C., Trakhtenbrot, B., Koss, M. J., et al. 2017, *ApJS*, 233, 17, doi: [10.3847/1538-4365/aa96ad](https://doi.org/10.3847/1538-4365/aa96ad)
- Ricci, C., Trakhtenbrot, B., Koss, M. J., et al. 2017, *ApJS*, 233, 17, doi: [10.3847/1538-4365/aa96ad](https://doi.org/10.3847/1538-4365/aa96ad)
- Ricci, C., Kara, E., Loewenstein, M., et al. 2020, *ApJL*, 898, L1, doi: [10.3847/2041-8213/ab91a1](https://doi.org/10.3847/2041-8213/ab91a1)
- Roming, P. W. A., Kennedy, T. E., Mason, K. O., et al. 2005, *SSRv*, 120, 95, doi: [10.1007/s11214-005-5095-4](https://doi.org/10.1007/s11214-005-5095-4)
- Roth, N., Kasen, D., Guillochon, J., & Ramirez-Ruiz, E. 2016, *ApJ*, 827, 3, doi: [10.3847/0004-637X/827/1/3](https://doi.org/10.3847/0004-637X/827/1/3)
- Sagiv, I., Gal-Yam, A., Ofek, E. O., et al. 2014, *AJ*, 147, 79, doi: [10.1088/0004-6256/147/4/79](https://doi.org/10.1088/0004-6256/147/4/79)
- Saxton, R., Komossa, S., Auchettl, K., & Jonker, P. G. 2020, *SSRv*, 216, 85, doi: [10.1007/s11214-020-00708-4](https://doi.org/10.1007/s11214-020-00708-4)

- Saxton, R. D., Read, A. M., Komossa, S., et al. 2017, *A&A*, 598, A29, doi: [10.1051/0004-6361/201629015](https://doi.org/10.1051/0004-6361/201629015)
- Sazonov, S., Gilfanov, M., Medvedev, P., et al. 2021, *MNRAS*, 508, 3820, doi: [10.1093/mnras/stab2843](https://doi.org/10.1093/mnras/stab2843)
- Schlaflly, E. F., & Finkbeiner, D. P. 2011, *ApJ*, 737, 103, doi: [10.1088/0004-637X/737/2/103](https://doi.org/10.1088/0004-637X/737/2/103)
- Schmidt, M. 1968, *ApJ*, 151, 393, doi: [10.1086/149446](https://doi.org/10.1086/149446)
- Shakura, N. I., & Sunyaev, R. A. 1973, *A&A*, 24, 337
- Shapiro, S. L., Lightman, A. P., & Eardley, D. M. 1976, *ApJ*, 204, 187, doi: [10.1086/154162](https://doi.org/10.1086/154162)
- Short, P., Nicholl, M., Lawrence, A., et al. 2020, *MNRAS*, 498, 4119, doi: [10.1093/mnras/staa2065](https://doi.org/10.1093/mnras/staa2065)
- Stein, R., Velzen, S. v., Kowalski, M., et al. 2021, *Nature Astronomy*, 5, 510, doi: [10.1038/s41550-020-01295-8](https://doi.org/10.1038/s41550-020-01295-8)
- Steiner, J. F., Narayan, R., McClintock, J. E., & Ebisawa, K. 2009, *PASP*, 121, 1279, doi: [10.1086/648535](https://doi.org/10.1086/648535)
- Stern, D., Assef, R. J., Benford, D. J., et al. 2012, Mid-infrared Selection of Active Galactic Nuclei with the Wide-Field Infrared Survey Explorer. I. Characterizing WISE-selected Active Galactic Nuclei in COSMOS, doi: [10.1088/0004-637X/753/1/30](https://doi.org/10.1088/0004-637X/753/1/30)
- Stone, N., & Loeb, A. 2012, *PhRvL*, 108, 061302, doi: [10.1103/PhysRevLett.108.061302](https://doi.org/10.1103/PhysRevLett.108.061302)
- Strüder, L., Briel, U., Dennerl, K., et al. 2001, *A&A*, 365, L18, doi: [10.1051/0004-6361:20000066](https://doi.org/10.1051/0004-6361:20000066)
- Subrayan, B. M., Milisavljevic, D., Chornock, R., et al. 2023, *ApJL*, 948, L19, doi: [10.3847/2041-8213/accfla](https://doi.org/10.3847/2041-8213/accfla)
- Sunyaev, R., Arefiev, V., Babyshkin, V., et al. 2021, *A&A*, 656, A132, doi: [10.1051/0004-6361/202141179](https://doi.org/10.1051/0004-6361/202141179)
- Thomsen, L. L., Kwan, T., Dai, L., Wu, S., & Ramirez-Ruiz, E. 2022, arXiv e-prints, arXiv:2206.02804. <https://arxiv.org/abs/2206.02804>
- Titarchuk, L., & Lyubarskij, Y. 1995, *ApJ*, 450, 876, doi: [10.1086/176191](https://doi.org/10.1086/176191)
- Tonry, J. L., Denneau, L., Heinze, A. N., et al. 2018, *PASP*, 130, 064505, doi: [10.1088/1538-3873/aabadf](https://doi.org/10.1088/1538-3873/aabadf)
- Tortosa, A., Bianchi, S., Marinucci, A., Matt, G., & Petrucci, P. O. 2018, *A&A*, 614, A37, doi: [10.1051/0004-6361/201732382](https://doi.org/10.1051/0004-6361/201732382)
- Trakhtenbrot, B., Arcavi, I., MacLeod, C. L., et al. 2019, *ApJ*, 883, 94, doi: [10.3847/1538-4357/ab39e4](https://doi.org/10.3847/1538-4357/ab39e4)
- Udalski, A., Szymański, M. K., & Szymański, G. 2015, *AcA*, 65, 1. <https://arxiv.org/abs/1504.05966>
- Ulmer, A. 1999, *ApJ*, 514, 180, doi: [10.1086/306909](https://doi.org/10.1086/306909)
- van Velzen, S. 2018, *ApJ*, 852, 72, doi: [10.3847/1538-4357/aa998e](https://doi.org/10.3847/1538-4357/aa998e)
- van Velzen, S., Gezari, S., Cenko, S. B., et al. 2019, *ApJ*, 872, 198, doi: [10.3847/1538-4357/aafe0c](https://doi.org/10.3847/1538-4357/aafe0c)
- van Velzen, S., Gezari, S., Hammerstein, E., et al. 2021, *ApJ*, 908, 4, doi: [10.3847/1538-4357/abc258](https://doi.org/10.3847/1538-4357/abc258)
- Virtanen, P., Gommers, R., Oliphant, T. E., et al. 2020, *Nature Methods*, 17, 261, doi: [10.1038/s41592-019-0686-2](https://doi.org/10.1038/s41592-019-0686-2)
- Wang, J., Kara, E., Lucchini, M., et al. 2022, *ApJ*, 930, 18, doi: [10.3847/1538-4357/ac6262](https://doi.org/10.3847/1538-4357/ac6262)
- Wevers, T. 2020, *MNRAS*, 497, L1, doi: [10.1093/mnras/slaa097](https://doi.org/10.1093/mnras/slaa097)
- Wevers, T., Pasham, D. R., van Velzen, S., et al. 2019a, *MNRAS*, 488, 4816, doi: [10.1093/mnras/stz1976](https://doi.org/10.1093/mnras/stz1976)
- Wevers, T., Stone, N. C., van Velzen, S., et al. 2019b, *MNRAS*, 487, 4136, doi: [10.1093/mnras/stz1602](https://doi.org/10.1093/mnras/stz1602)
- Wevers, T., Pasham, D. R., van Velzen, S., et al. 2021, *ApJ*, 912, 151, doi: [10.3847/1538-4357/abf5e2](https://doi.org/10.3847/1538-4357/abf5e2)
- Wevers, T., Nicholl, M., Guolo, M., et al. 2022, *A&A*, 666, A6, doi: [10.1051/0004-6361/202142616](https://doi.org/10.1051/0004-6361/202142616)
- Wilms, J., Allen, A., & McCray, R. 2000, *ApJ*, 542, 914, doi: [10.1086/317016](https://doi.org/10.1086/317016)
- Wiseman, P., Wang, Y., Hönig, S., et al. 2023, *MNRAS*, 522, 3992, doi: [10.1093/mnras/stad1000](https://doi.org/10.1093/mnras/stad1000)
- Wyrzykowski, L., Zieliński, M., Kostrzewa-Rutkowska, Z., et al. 2017, *MNRAS*, 465, L114, doi: [10.1093/mnrasl/slz213](https://doi.org/10.1093/mnrasl/slz213)
- Yao, Y., & Gezari, S. 2022, *The Astronomer's Telegram*, 15751, 1
- Yao, Y., Wang, Q. D., & Nan Zhang, S. 2005, *MNRAS*, 362, 229, doi: [10.1111/j.1365-2966.2005.09294.x](https://doi.org/10.1111/j.1365-2966.2005.09294.x)
- Yao, Y., Lu, W., Guolo, M., et al. 2022, arXiv e-prints, arXiv:2206.12713. <https://arxiv.org/abs/2206.12713>
- Yao, Y., Ravi, V., Gezari, S., et al. 2023, arXiv e-prints, arXiv:2303.06523, doi: [10.48550/arXiv.2303.06523](https://doi.org/10.48550/arXiv.2303.06523)
- Yuan, W., Zhang, C., Feng, H., et al. 2015, arXiv e-prints, arXiv:1506.07735, doi: [10.48550/arXiv.1506.07735](https://doi.org/10.48550/arXiv.1506.07735)
- Zauderer, B. A., Berger, E., Soderberg, A. M., et al. 2011, *Nature*, 476, 425, doi: [10.1038/nature10366](https://doi.org/10.1038/nature10366)

APPENDIX

A. MODELING OF CORONA EMISSION IN TDES WITH `simpl`

In the study of active galactic nuclei (AGN), the corona is the primary X-ray emitter, while the cold accretion disks mainly emit in the UV bands. AGN X-ray spectra are often described using the `powerlaw` model, despite some attempts to develop more comprehensive models like `Optxagnf` (Done et al. 2012), these face challenges due to numerous parameters and degeneracies. Therefore, the `powerlaw` model remains prevalent in AGN X-ray literature.

In X-ray binaries (XRBs), the accretion disks are hotter and emit mainly in the X-ray bands. In the soft state of XRBs, the accretion disk dominates the X-ray emission, but as they transition to the hard state, an emergent corona with a power-law spectrum becomes dominant. The `powerlaw` model is widely used in XRB modeling but suffers from the drawback of rising infinitely at low energies, which is inconsistent with Comptonization.

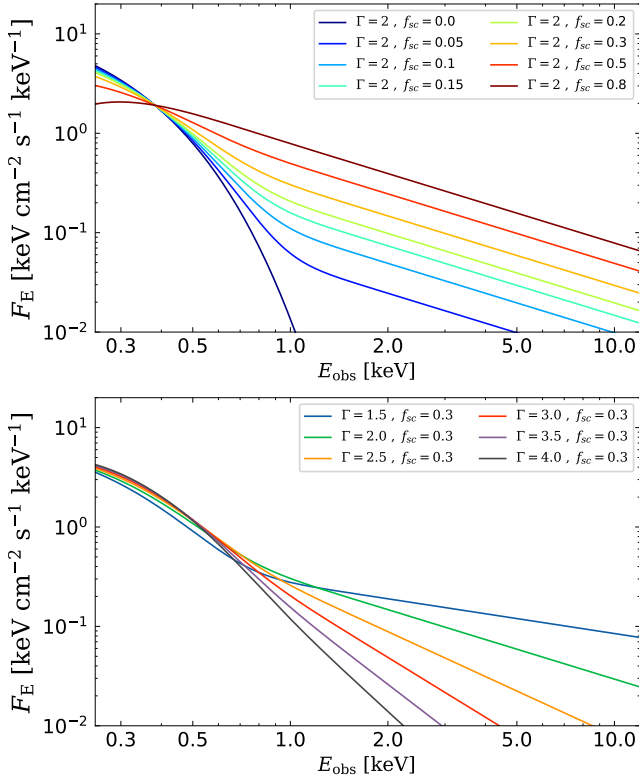


Figure 21. Simulation of `SimPL` model spectra. Upper panel: Fixed power law index (Γ_{sc}) varying fraction of up-scattered photons (f_{sc}). Bottom panel: Fixed f_{sc} varying Γ_{sc} .

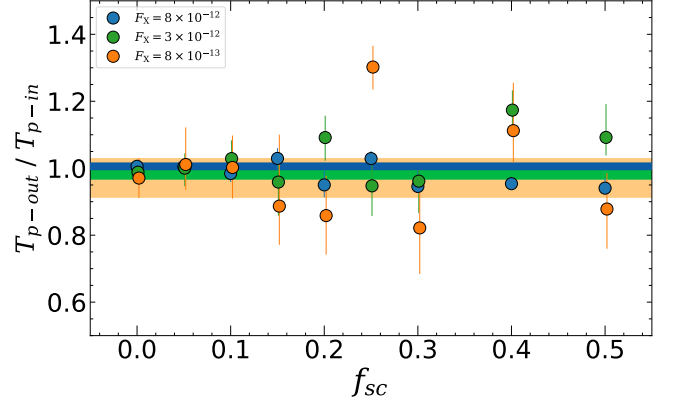


Figure 22. Simulation on the measurement of the underlying disk properties in the presence of a corona comptonization. The y-axis show the ratio between the input and output T_p as a function of the corona strength (f_{sc})

. The color show distinct fluxes of the mock spectra, and the shaded regions the uncertainty in the $f_{sc} = 0$ spectra, i.e. the uncertainty from the instrumental S/N.

To overcome the limitation of the `powerlaw` model in accurately describing Comptonization, Steiner et al. (2009) introduced `simpl`, a flexible convolution model for fitting X-ray spectra of XRBs. `simpl` captures Comptonization effects using any seed photon spectrum and shares parameters such as the photon index (Γ) with the `powerlaw` model. However, it employs the scattered fraction (f_{sc}) as the normalization factor instead of photon flux, simplifying the model by omitting specific details of the Comptonizing medium while maintaining a physically consistent approach. Unlike the `powerlaw` model, `simpl` directly links the power-law component to the input photon energy distribution, resulting in a power-law tail at higher energies without extending indefinitely to lower energies. This behavior aligns with Compton-scattering expectations and is commonly observed in physical Comptonization models. Notably, in the soft X-ray bands, `simpl` exhibits a natural cutoff consistent with Comptonization, whereas the `powerlaw` model continues to rise without limit (Yao et al. 2005).

Similarly to XRBs, TDEs also have a portion of their continuum disk emission in the X-rays. Therefore, a similar approach can be applied to model the X-ray spectra of TDEs. Figure 21 demonstrates the effects of using `simpl` through a series of simulations where a thermal model with $T_p \approx 70$ eV and $R_p \approx 10^{12}$ cm is convoluted with `simpl` using different values of f_{sc} (top panel) and Γ (bottom panel). With $f_{sc} = 0$, there is no corona emission, the resulting model corresponds to the input

disk spectrum. As f_{sc} increases from 0.05, the spectrum remains dominated by the disk, but with a faint hard excess. Between $0.5 \leq f_{sc} \leq 0.20$, the source enters an intermediate state, where the thermal and non-thermal spectra have similar fluxes. When $f_{sc} \approx 0.3$, the total spectrum becomes almost indistinguishable from a pure power-law, and the spectrum remains consistent with a power law for higher values.

An important question to our X-ray spectral analyses (3.3.1 and 4.2.1) is up to what corona strength (as probed by f_{sc}) the underlying thermal continuum can be recovered from the fitting. To answer this question we simulate mock X-ray spectra using the `fakeit` command in `xspec` for a stacked 30 ks observation with *Swift*/XRT, assuming `simpl \otimes tdediscspec`, a random T_p in the range of observed in our sample, for three fluxes ($F_X = 8 \times 10^{-12}, 3 \times 10^{-12}, 8 \times 10^{-13} \text{ erg cm}^{-2} \text{ s}^{-1}$) levels, and varying f_{sc} between 0.0 (no corona) and 0.5. We then fit the mock spectra with the same model in order to measure the best-fit T_p , and compare with the input value. Fig. 22 summarized our findings. The underlying (input) temperature can be recovered (within the error-bar) considering the uncertainties related with the S/N of the instrument (shaded regions) up to $f_{sc} \approx 0.2$, at higher values the underlying information on the temperature of the disk is lost by the emergency of the corona in the higher energies of the disk spectrum, and can not be uniquely recovered.

B. SIMULATION OF EXPECTED L_{BB}/L_X FOR STANDARD DISK

An important observational probe of TDE emission is the ratio L_{BB}/L_X between the UV/optical luminosity (as fitted by a blackbody) and the 0.3-10 keV X-ray luminosity. Although additional emission processes should be involved, the formation of accretion disk is a natural prediction of a tidal disruption event. In this section, we aim to probe the range of L_{BB}/L_X that can be produced by an *bare/unreprocessed* accretion disk, given the range of inner peak temperatures (T_p) we observe from the X-ray fitting. To obtain that we simulate accretion disk with varying T_p between $5.5 \leq \log T_p \leq 6.1$ Kelvin, we test two distinct disk solutions for the temperature profile of the disk: the standard vanishing ISCO stress solution (Shakura & Sunyaev 1973; Makishima et al. 1986), $T(r) \propto r^{-3/4}$, and the finite ISCO stress (Agol & Krolik 2000), $T(r) \propto r^{-7/8}$. We pass the synthetic SED into the sensibility curve of the six UVOT and two ZTF filters, and fitted the resulting broad-band UV/optical with a blackbody to obtain L_{BB} , the same way it was done in the observed data (see Fig. 2 for illustration). The ratio L_{BB}/L_X as a function of T_p for the two dis-

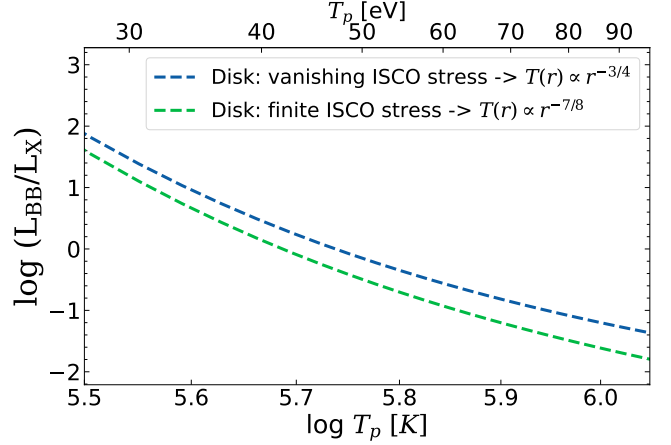


Figure 23. Simulation of expected expected UV/optical to X-ray luminosity ratio (L_{BB}/L_X) for standard disk. The y-axis show the expected L_{BB}/L_X from a *bare/unreprocessed* accretion disk with two distinct temperature profiles (green and blue lines), as a function of the peak temperature of the disk (T_p).

tinct disk solution is shown in Fig. 23. For the entire range L_{BB}/L_X is between 5×10^{-2} and a maximum of ~ 70 . At late times, most our sample shows disk cooling, and all TDE have $\log T_p \leq 5.8$, this limits L_{BB}/L_X to values > 0.3 , but rarely higher than 10, which is in agreement with our findings in Fig. 14.

C. THE BASS AGN SAMPLE

The *Swift*/BAT 70-month AGN catalog consists of 858 nearby ($z \lesssim 0.3$ for unbeamed) AGN (Koss et al. 2022), and using soft X-ray observations by XMM-Newton, *Swift*, ASCA, Chandra, and Suzaku, their broadband X-ray spectra were characterized and presented by Ricci et al. (2017). Some of the properties they constrain are the intrinsic X-ray luminosity (in the 2–10, 20–50, and 14–150 keV bands), the line-of-sight column density of obscuring material (N_H), the slope of the X-ray power-law continuum, and the temperature of the thermal plasma for obscured sources. The many phenomenological models used are broadly classified into four groups: unobscured (352), obscured (386), blazars (97), and other non-AGN models (2). The 75 sources that were found to be Compton-thick by a phenomenological model were again fit in `xspec` with the `BNtorus` model (Brightman & Nandra 2011) to better constrain N_H of heavily obscured sources. The remaining details of the X-ray modeling of the BASS sample can be found in Ricci et al. (2017).

From among these sources, we selected those that were either obscured or unobscured (which excludes beamed and non-AGN sources), and that had spectroscopic redshift measurements from optical counterparts. This re-

sulted in 617 sources. To calculate the HR, the X-ray spectra were simulated from the models using `XSPEC`, and the count rate was recorded for the soft (0.3–2.0 keV) and hard (2.0–10.0 keV) bands. Spectra were measured with a long response time (1 Ms) to minimize the effects of statistical noise on the HR. This was done twice: with the response files for Swift/XRT photon counting grade 0-12 and XMM-Newton Epic PN. We also measured the 0.3-10.0 keV intrinsic luminosities by setting all N_H parameters of all model components to zero (or, in certain cases, the minimum nonzero value allowed by the model) and using the `calcLumin` command.

D. SUPPLEMENTARY DATA

Table 4. ZTF control sample, described in §4.4.

Source	z	$L_X \geq 10^{42} \text{ erg s}^{-1}$	$\log (M_{\text{BH}}/M_{\odot})^a$
AT2018zr	0.075	False	5.83 ± 0.51
AT2018bsi	0.051	False	7.46 ± 0.47
AT2018hco	0.088	False	6.44 ± 0.48
AT2018iih	0.212	False	7.93 ± 0.48
AT2018hyz	0.046	False	6.12 ± 0.46
AT2018lna	0.091	False	5.21 ± 0.54
AT2019azh	0.022	True	6.68 ± 0.46
AT2019dsg	0.051	True	7.04 ± 0.45
AT2019ehz	0.074	True	5.75 ± 0.59
AT2019mha	0.148	False	6.41 ± 0.49
AT2019meg	0.152	False	5.81 ± 0.52
AT2019qiz	0.015	False	6.49 ± 0.49
AT2019teq	0.087	True	6.32 ± 0.49
AT2020pj	0.068	False	6.43 ± 0.49
AT2019vcb	0.088	True	5.59 ± 0.52
AT2020ddv	0.160	True	6.09 ± 0.55
AT2020ksf	0.092	True	5.92 ± 0.48
AT2020ocn	0.070	True	6.77 ± 0.49
AT2020mot	0.070	False	7.04 ± 0.47
AT2020wey	0.027	False	5.38 ± 0.51
AT2020zso	0.057	False	6.12 ± 0.48
AT2020vwl	0.033	False	5.80 ± 0.48
AT2021ehb	0.018	True	7.04 ± 0.46
AT2021nwa	0.047	False	7.21 ± 0.46
AT2020ksf	0.092	True	5.92 ± 0.48
AT2021yzv	0.286	True	7.45 ± 0.47

NOTE—a) Black hole masses. When a σ_* measurement is available it is estimated using the Gültekin et al. (2019) σ_*-M_{BH} relation, when σ_* is not available, this is estimated from the M_*-M_{BH} relation presented in Yao et al. 2023.

Table 5. Sources used on the luminosity function.

Source	z	'peak' L_X (erg s^{-1})	Survey
AT2018zr	0.071	5.55×10^{41}	ZTF
AT2018hyz	0.045	7.51×10^{41}	ZTF/ASASSN
AT2019azh	0.022	1.65×10^{43}	ZTF/ASASSN
AT2019dsg	0.051	3.90×10^{43}	ZTF
AT2019ehz	0.074	6.35×10^{43}	ZTF
AT2019qiz	0.015	8.06×10^{40}	ZTF/ASASSN
AT2019teq	0.087	4.06×10^{43}	ZTF
AT2019vcb	0.088	1.66×10^{43}	ZTF
AT2020ddv	0.160	3.45×10^{43}	ZTF
AT2020ksf	0.092	1.07×10^{44}	ZTF/eROSITA
AT2020ocn	0.070	1.04×10^{44}	ZTF
AT2021ehb	0.018	1.78×10^{44}	ZTF
ASASSN-14li	0.020	9.77×10^{43}	ASASSN
ASASSN-15oi	0.048	4.93×10^{42}	ASASSN
AT2018fyk	0.059	1.76×10^{44}	ASASSN
OGLE16aaa	0.165	4.92×10^{43}	OGLE
AT2021yzv	0.288	3.83×10^{42}	ZTF
J135514.8+311605	0.199	5.80×10^{43}	eROSITA
J013204.6+122236	0.123	4.20×10^{43}	eROSITA
J153503.4+455056	0.231	8.80×10^{43}	eROSITA
J163831.7+534020	0.581	2.50×10^{44}	eROSITA
J163030.2+470125	0.294	2.00×10^{44}	eROSITA
J021939.9+361819	0.387	2.50×10^{44}	eROSITA
J161001.2+330121	0.131	1.20×10^{43}	eROSITA
J171423.6+085236	0.036	5.30×10^{42}	eROSITA
J071310.6+725627	0.104	1.10×10^{44}	eROSITA
J095928.6+643023	0.045	8.90×10^{44}	eROSITA
J091747.6+524821	0.187	4.80×10^{44}	eROSITA
J133053.3+734824	0.150	3.40×10^{43}	eROSITA
J144738.4+671821	0.125	2.70×10^{43}	eROSITA
NGC5905	0.011	7.00×10^{42}	ROSAT
RXJ1624+7554	0.064	2.00×10^{44}	ROSAT
RBS 1032	0.026	1.00×10^{43}	ROSAT
RXJ1420+5334	0.147	2.50×10^{44}	ROSAT
RXJ 1242-1119	0.050	4.00×10^{44}	ROSAT
TDXF1347-3254	0.037	7.00×10^{42}	ROSAT
NGC 3599	0.003	1.20×10^{41}	XMMLS
SDSS J1323+48	0.087	4.40×10^{43}	XMMLS
SDSS J0939+37	0.184	2.60×10^{44}	XMMLS
2MASX J0203-07	0.062	2.80×10^{43}	XMMLS
2MASX J02491-04	0.019	2.10×10^{42}	XMMLS
SDSS J1201+30	0.146	3.00×10^{44}	XMMLS
2MASX 0740-85	0.017	2.00×10^{43}	XMMLS
XMMSL2 J1446+68	0.029	6.00×10^{42}	XMMLS
XMMSL1 J1404	0.043	3.00×10^{43}	XMMLS